Numerical modeling of train-induced ground vibrations

Malmborg, Jens

2020

Document Version:
Publisher's PDF, also known as Version of record

LUND UNIVERSITY

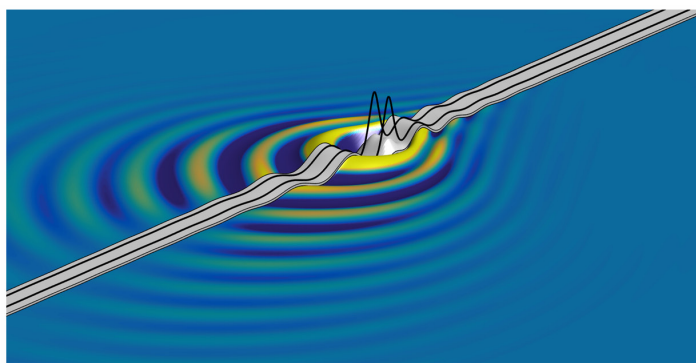

NUMERICAL MODELING OF TRAIN-INDUCED GROUND VIBRATIONS

JENS MALMBORG

Structural Mechanics

Licentiate Dissertation

DEPARTMENT OF CONSTRUCTION SCIENCES
DIVISION OF STRUCTURAL MECHANICS

ISRN LUTVDG/TVSM--20/3080--SE (1-132) | ISSN 0281-6679
ISBN 978-91-7895-438-4 (Print) | 978-91-7895-439-1 (Pdf)
LICENTIATE DISSERTATION

NUMERICAL MODELING OF TRAIN-INDUCED GROUND VIBRATIONS

JENS MALMBORG

Printed by V-husets tryckeri LTH, Lund, Sweden, February 2020 *(Pl)*.

For information, address:
Div. of Structural Mechanics,
Faculty of Engineering LTH, Lund University, Box 118, SE-221 00 Lund, Sweden.
Homepage: www.byggmek.lth.se

Acknowledgements

I would like to express my gratitude towards my supervisor Prof. Kent Persson for giving me the opportunity to become a PhD student and for giving me the freedom to explore an interesting field. I would also like to thank my co-supervisor Dr. Peter Persson, for carefully reading and commenting on my manuscripts. Thanks are directed to both supervisors for their support with various matters during my studies. I am also grateful to Mr. Bo Zadig for his excellent work with many of the illustrations.

Thanks to Prof. Lars Vabbersgaard Andersen and Dr. Paulius Bucinskas from Aarhus University for helpful advice regarding the semi-analytical ground model, and pleasant company during conferences.

Furthermore, I would like to thank my good friend and long-time colleague Linus Andersson for fruitful discussions and moral support.

Finally, I thank my wife Stina and my son Torsten for constantly reminding me about what is truly important.

February 2020
Jens Malmborg

Abstract

The population is growing, and an increasing proportion of the population live in urban areas. As a consequence, human exposure to noise and vibrations is increasing. Larger and denser cities lead to a higher amount of traffic close to where people work and live. Land close to railways and heavily trafficked roads, previously left unexploited, are now being used for dwellings and offices. Vibrations are often accompanied by noise, to which long-term exposure is known to have serious health effects. Furthermore, some buildings such as hospitals and research facilities contain instruments that are highly sensitive to vibrations, and require proper vibration isolation to ensure safe operation. To address the problems of noise and vibrations, their generation and propagation need to be understood.

In this thesis, numerical modeling strategies for predicting ground-borne vibrations from a surface railway track have been studied. Focus have been on the vibration transmission from the track to the free-field, and to a smaller extent on the actual load generation due to a train running on an uneven rail.

The wave propagation in the ground resulting from the dynamic loads on the track can be calculated using numerous numerical techniques. The finite element method offers a large flexibility regarding modeling capabilities in terms of geometrical conditions and material properties. However, the need for discretizing a large soil volume, under and between the track and the receiver, can generate very large systems of equations that are time-consuming or practically impossible to solve. Computational savings can be made by introducing a coordinate transformation into the governing equations, so that the computational model is formulated in a moving frame of reference following the vehicle. Furthermore, if a horizontally layered viscoelastic half-space is assumed, a so called Green's function (a fundamental solution) for the ground dynamic response can be found very efficiently by employing a semi-analytical solution procedure in frequency–wavenumber domain. Here, the Green's function in a moving reference frame was used for establishing a dynamic stiffness matrix for a set of points in the track–soil interface, to which a finite element representation of the track was coupled. After solving the coupled track–soil problem, the Green's function was used again to obtain the free-field ground vibrations resulting from the forces in the track–soil interface. The influence of different modeling strategies regarding the railway track was investigated, and further the change in response due to a mitigation measure under the track was studied using this model.

Additional efficiency may be obtained by applying a so called 2.5D procedure, in which a Fourier transform with regards to the track direction coordinate is performed. Instead of solving one large 3D problem, a sequence of 2D problems is solved for a set of discrete wavenumbers, after which the 3D response is recovered by an inverse Fourier transform. In the thesis, a very time efficient model is formulated that employs a 2.5D finite element representation of the

railway track, coupled to a dynamic stiffness matrix of the layered ground obtained using the aforementioned semi-analytical approach.

Finally, a 2.5D model employing finite elements for both the track and the surrounding soil was implemented and compared to the two previously mentioned coupled models, showing very good agreement.

Contents

Paper C
Effects of modeling strategies for a slab track on predicted ground vibrations.
J. Malmborg, P. Persson, K. Persson
Submitted for publication in international journal.

Part I

Introduction and Overview

1 Introduction

1.1 BACKGROUND

The population is growing. Currently (year 2020), 88% of the Swedish population live in urban areas. For the population worldwide, the figure is 56%. These numbers are increasing. [1]

As a consequence of the urban densification, human exposure to noise and vibrations is increasing. Larger and denser cities lead to a higher amount of traffic close to where people work and live. In most cities, construction sites emitting noise and vibrations are constantly present. Land close to railways and heavily trafficked roads, previously left unexploited, are now being used for dwellings and offices. Vibrations are often accompanied by noise, which is known to cause serious health effects. Furthermore, some buildings such as hospitals and research facilities contain instruments that are highly sensitive to vibrations, and require proper vibration isolation to ensure safe operation.

To address the problems of noise and vibrations, their generation and propagation need to be known. When the physics behind the observed phenomena is understood, appropriate mitigation measures may be undertaken. To describe the physics in detail, mathematical models are required. These models are generally so complex that they need to be solved using computers. Such models can then be used to evaluate the efficacy of different design alternatives, by numerically predicting the outcome of different scenarios. They can therefore be helpful in making better decisions during the early stages of design of, for example, a new building close to a railway track.

1.2 AIMS AND OBJECTIVES

The long-term aim of the work presented in this thesis is to reduce noise and vibrations for residents close to railways and heavily trafficked roads, and to enable safe operation of sensitive equipment and instruments in such areas. To accomplish the long-term goal, tools are needed to understand and predict the generation and propagation of such vibrations.

The objective in this work is to investigate and develop efficient numerical techniques and models that can be used in engineering practice for predicting ground-borne vibrations emanating from man-made sources (so called environmental vibrations), such as construction activities, road and railway traffic. Apart from being able to properly represent the transmission of the vibrations through the ground, and eventually into a building structure, such models need to include the source of the vibrations.

In this thesis, two numerical techniques are combined to predict the free-field ground vibrations caused by a train running on a railway track. The influence of different modeling strategies regarding the railway track is investigated, and further the change in response due to a mitigation measure under the track is studied.

1.3 LIMITATIONS

Vibrations from a train running at constant speed along a straight railway track with constant geometry is considered. Vibrations due to rail curvature, rail joints/switches, transition zones, varying subgrade stiffness, etc. are not accounted for. However, vertical rail unevenness of the rail is considered. The vehicle speed is assumed to be lower than the phase velocity of the elastic waves in the ground. Furthermore, only the free-field vibrations on the soil surface are considered, i.e. the transmission of vibrations into buildings have not yet been studied.

1.4 OUTLINE

This thesis is divided into two parts:

Part I contains an introduction to the research area of environmental vibrations, with particular emphasis on the physics and the numerical modeling of ground-borne vibrations. In Chapter 2, some general concepts regarding the generation and propagation of ground vibrations are introduced, together with a brief summary of vibration mitigation measures. Further, the excitation mechanisms behind ground vibrations generated by railway traffic are introduced, with a short review of different computational modeling strategies aiming to simulate some of these mechanisms and the resulting wavefield in the ground. Chapter 3 provides the basics of the physics that govern the dynamics of structural systems, and different wave types in structural elements and an elastic continuum are derived. Two numerical methods used extensively in the present work are described in Chapter 4, namely the Finite Element Method and the Layer Transfer Matrix method. How these methods can be used for efficiently evaluating the response of moving loads is given special attention. Three different computational models that have been implemented are described in Chapter 5 along with a small example case. A summary of the appended papers are given in Chapter 6, and finally some concluding remarks are given in Chapter 7. Part II contains the appended papers.

2 Environmental Vibrations

2.1 GENERAL REMARKS

In the urban environment, there is a vast number of sources producing vibrations. Heavily trafficked roads, railways, and construction work (e.g. pile driving), are a few examples of external sources that can generate vibrations perceptible inside a building. Rotating machinery, ventilation systems, walking people, closing doors, are examples of internal vibration sources.

The current work is focused on models for predicting vibrations generated by external sources, where the vibrations are generated in one location and transmitted to a second location through the ground. The process of vibration transmission is often described in terms of a source, a medium and a receiver. The receiver can be a building, a part of a building structure, equipment or a person inside the building. The medium, or transmission path, where the vibrations are transferred as elastic waves, includes the ground but could also, depending on the receiver, include the building; see Figure 2.1.

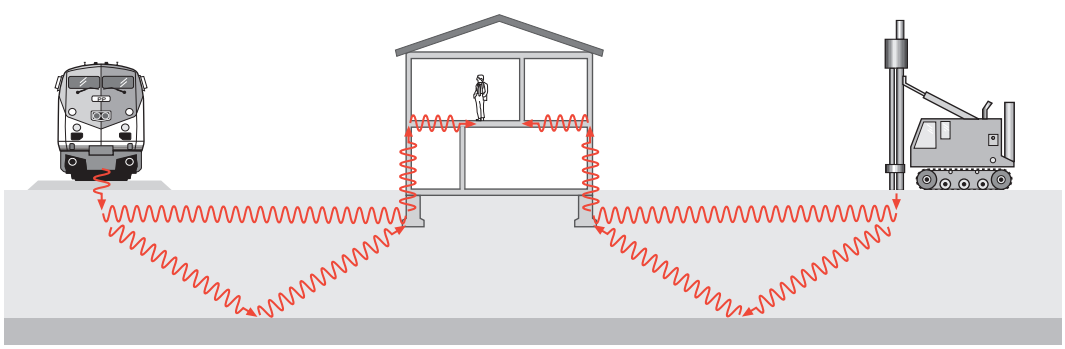

Figure 2.1: Vibration transmission from the source, via the transmission path, to the receiver.

2.2 EFFECTS OF GROUND-BORNE VIBRATIONS

Ground-borne vibrations may cause annoyance to humans, through perceptible motion of building floors and radiated noise. Ground-borne vibrations from pile driving and blasting during construction may also lead to structural damage of buildings, however such effects from road and railway traffic are very rare [2]. Furthermore, the operation of sensitive equipment in for example hospitals or research facilities may be adversely affected by ground-borne vibrations.

Vibration is an oscillatory motion around a static equilibrium, and such a motion may be described or quantified in many different ways using different descriptors. The amplitude of the vibration may be described in terms of the maximum displacement, velocity or acceleration during the event, or in terms of an "effective value" calculated as the root-mean-square (RMS). Further, a vibration may consist of a single harmonic motion or have a broad frequency content.

In the frequency range $20 - 250$ Hz, vibrations inside buildings may lead to acoustic radiation heard as a rumbling noise. Furthermore, the vibrations may excite resonance frequencies of structural members and furniture inside the building, producing a rattling noise [3]. At low frequencies (< 80 Hz), humans are sensitive to whole-body vibrations, but how the vibrations are perceived also depends on the amplitude and the duration of the vibration [2]. There are studies suggesting that environmental noise contributes to cardiovascular risk of coronary artery disease, hypertension, stroke and heart failure [4].

The international standard ISO 2631 [5] specifies vibration criteria guidelines for different applications in terms of allowable RMS values of vibration velocity in 1/3 octave bands. These

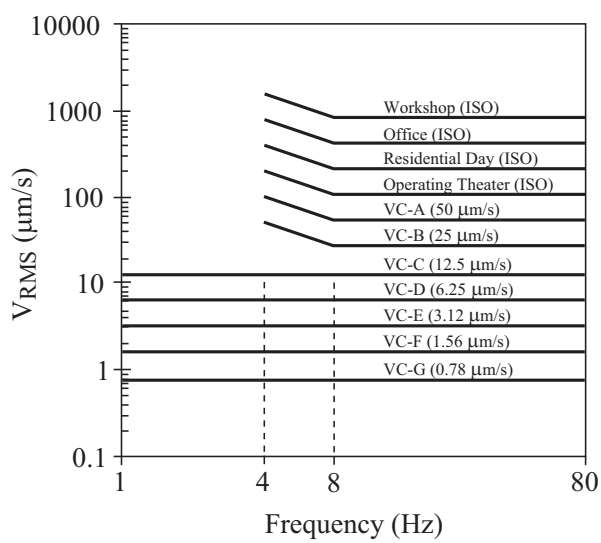

Figure 2.2: Vibration requirements. ISO guidelines and VC curves.

are shown in Figure 2.2, together with so called Vibration Criterion (VC) curves, that are frequently used by manufacturers of sensitive equipment to specify maximum allowable vibration levels.

2.3 GROUND VIBRATIONS

2.3.1 Wave propagation

Ground vibrations propagate as elastic waves. In an infinite, homogeneous, elastic medium (a so called full-space), only two different types of waves exist; the P-wave and the S-wave, which propagate independently of each other. The P-waves are also called pressure, dilational, longitudinal, irrotational or primary waves. P-waves are the fastest moving waves, and the particle movement is parallel with the wave propagation direction. The S-waves are also called shear, rotational, equivoluminal or secondary waves, and are characterized by a particle movement that is perpendicular to the wave propagation direction. However, in a homogeneous, elastic semi-infinite medium involving a free surface (a so called half-space), the P- and S-waves interact at the surface, resulting in a surface wave called the Rayleigh wave, propagating with a slightly lower velocity than the S-wave. The particle motion is elliptical, and the amplitude decreases with depth. At the surface, the particle motion is retrograde. At depths larger than about 1.5 wavelengths, the particle displacement amplitude is only a few percents of the maximum value, see further Section 3.3.2. The P-, S- and Rayleigh waves are shown schematically in Figure 2.3.

For a harmonic excitation, the wavelength λ of the resulting waves are $\lambda = c/f$, where c is the wave propagation speed (the so called phase velocity) of the respective wave type and f is the frequency, in Hz, of the harmonic load. The wavenumber is defined as $k = 2\pi/\lambda$ and is

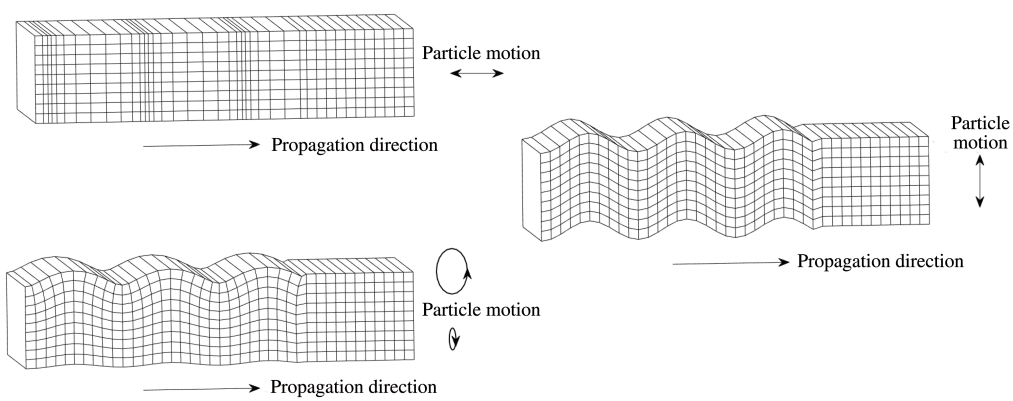

Figure 2.3: P-, S- and Rayleigh waves.

the space domain equivalent of the angular frequency ω in time domain ($\omega = 2\pi f = 2\pi/T$).

Disregarding any energy dissipation due to material damping, the total energy within a traveling wave remains constant. However, since the wavefront increases in size with increasing distance from the source, the energy density decreases, causing an attenuation of the particle displacement amplitude. Contrary to the P- and S-waves, that propagate away from a point source with spherical wavefronts, the Rayleigh wave propagates only along the surface with a circular wavefront. Therefore, the attenuation is weaker for the Rayleigh wave than for the P- and S-waves. The Rayleigh wave carries about $2/3$ of the energy transmitted into the ground from a vertical oscillatory load on the surface of an elastic half-space [6]. Furthermore, due to the lower attenuation of the Rayleigh wave, the particle displacement on the soil surface is often primarily due to the Rayleigh wave, especially at longer distances.

The earth is not a homogeneous half-space. All soils are layered to some extent, with different material properties within and between the different layers. Hence, waves propagate with different velocities in the different layers. When a wave arrives at an interface between two layers with different elastic properties, the wave is partially reflected and partially refracted. Similarly to the case of P- and S-waves interacting at the free surface of a homogeneous half-space, interaction between the two waves takes place along an interface between two different materials. The layering also introduces surface waves other than the fundamental Rayleigh wave. These are often called P-SV waves, indicating that they stem from interacting P- and vertically polarized S-waves. In fact, the depth and material properties of the different soil layers have a huge impact on the vibration response. Some typical wave speeds of P- and S-waves in different soil materials are shown in Figure 2.4.

As will be shown in Section 3.3.2, the speeds with which the P-, S- and Rayleigh waves propagate (c_p, c_s and c_R) within a homogeneous material are independent of frequency. Such waves are called non-dispersive. In a layered soil, with homogeneous layers, the surface waves become dispersive due to the fact that the wavefronts potentially span several soil layers with different mechanical properties. For very low frequencies, i.e. long wavelengths, the velocity of the sur-

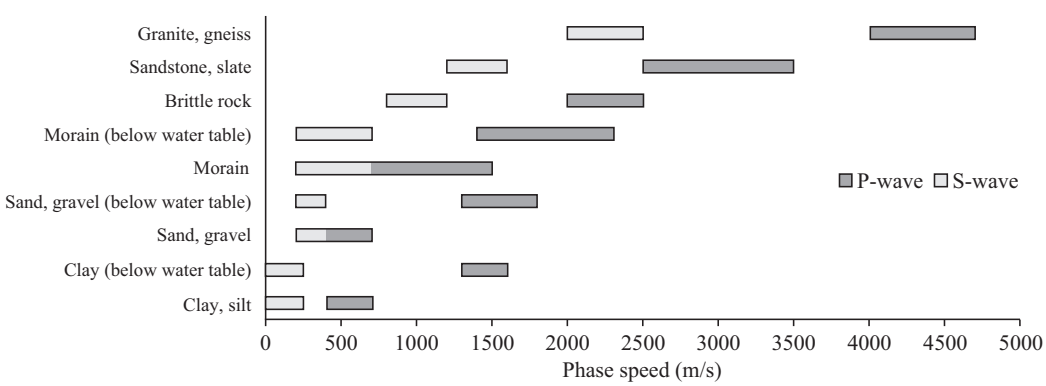

Figure 2.4: Phase velocities of P- and S-waves in some typical ground materials [7].

face wave is generally governed by the phase velocity in the lower soil layers. On the contrary, for higher frequencies, i.e. short wavelengths, when most of the surface wave is contained in the upper layer(s), the phase velocity of the Rayleigh wave in the upper layer(s) governs the velocity of the surface wave. This is illustrated in Figure 2.5, showing the so called dispersion diagrams of the P-, S- and Rayleigh waves for the two materials of a layered ground consisting of a 4 m deep clay shale layer, overlaying a half-space. The dispersion curves of the stiffer half-space material are shown in blue, whereas the corresponding curves for the soil layer are shown in red. The curves are shown in a wavenumber–frequency diagram, so that the phase velocity of each wavetype is given by the inverse of the slope in the diagram ($c = \omega/k$). The lines have a constant slope, i.e. the same phase velocity regardless of frequency. The curves are displayed over a contour plot showing the amplitude of vertical response due to a vertical harmonic excitation of the soil surface, where black indicates high response and white indicates low response. For excitation frequencies over about 15 Hz, the response for a given frequency is dominated by wavenumbers around the Rayleigh wave of the top soil material, meaning that the fundamental surface wave is practically unaffected by the higher phase velocities in the underlying half-space. An increasing number of higher order waves, faster than the fundamental surface wave, emerge for increasing frequencies. For frequencies below 5 Hz, the response on the soil surface is dominated by lower wavenumbers pertaining to the phase velocity in the underlying half-space, and in the range $\sim$ 5–15 Hz the velocity of the wave dominating the response is affected by both the top soil layer and the half-space.

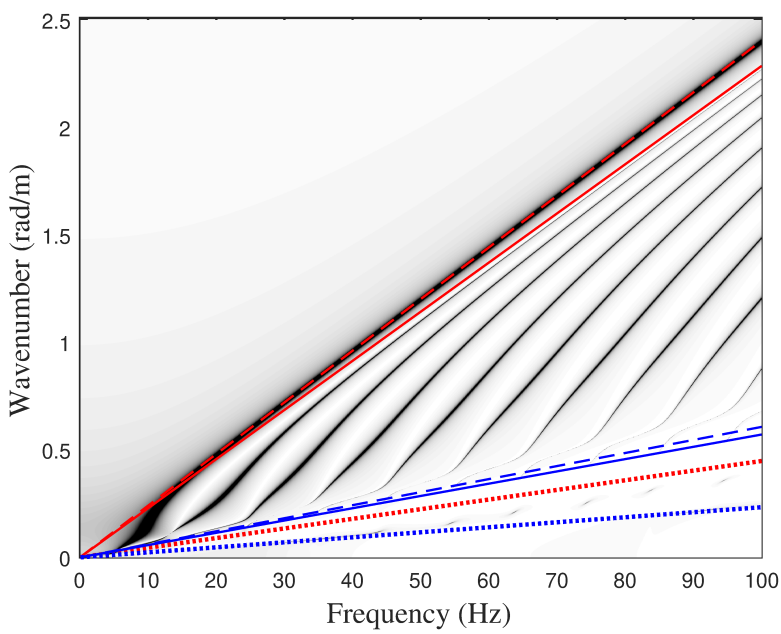

Figure 2.5: Dispersion curves for a layered half-space. Straight lines represent P-waves (dotted), S-waves (solid) and Rayleigh-waves (dashed) of the top soil (red) and the half-space material (blue).

In reality soil is not a homogeneous, linearly elastic medium. Soil is a granular material that typically displays a highly non-linear behavior. However, for the frequencies of interest in environmental vibrations, the wavelengths are much longer than the typical particle size, which makes a continuum model reasonable. For most problems relating to environmental vibrations, the strain levels remain relatively low, especially at some distance from the source, justifying a linear elastic approach. In all forthcoming sections and chapters, a linear elastic continuum approach is assumed for the soil in the numerical predictions of ground vibrations. Further, it is assumed that the soil is horizontally stratified, i.e. that it consists of horizontal layers.

2.3.2 Ground response to stationary and moving loads

The response of the ground to a dynamic load depends, apart from the site conditions (i.e. soil stratification and elastic properties), on the load distribution in space and time. The distribution in time, i.e. the load time-history signal, can be decomposed into its spectral components through a Fourier transform. The analysis of single harmonic excitation components, in contrast to a transient time-history analysis, is sometimes preferred both due to computational efficiency and physical insight.

When a harmonic load with frequency f is stationary, i.e. remains in the same position on the soil surface, the response in a stationary receiver anywhere on the soil surface is also harmonic with the same frequency. If the load is moving with a constant velocity on the soil surface, the response in a receiver moving with the same velocity is also harmonic with the frequency of the load. However, if the receiver position remains fixed and the load is moving (or vice versa), the response in the receiver becomes transient. The response amplitude increases as the load approaches the receiver, and decreases as the load recedes away from the receiver. Furthermore, the response in the stationary receiver contains more frequencies than the excitation frequency f of the moving load. When the load is approaching the receiver, the wavelengths of the waves reaching the receiver are compressed, and instead elongated as the load moves away from the receiver. This is known as the Doppler effect. This phenomenon is illustrated in Figure 2.6, for a unit harmonic load at $f = 40$ Hz distributed over a circular area ($r = 0.5$ m) on the soil surface. Figure 2.6 (a) shows the wavefield on the soil surface when the load is stationary, whereas in (b) the load is moving with a velocity of $v = 0.38c_R = 100$ m/s along the positive x-axis. The time-history response of a stationary point, located at $(x, y) = (0, 15)$, is shown in Figure 2.7, for the case of a stationary load (a), and for the case of the moving load (b). In figure (b), for the moving load, the time $t = 0$ corresponds to when the load is located at $(x, y) = (0, 0)$. The difference in time periods for one cycle of vibration in the beginning and the end of the event is clearly seen.

A moving load generates vibrations in a stationary receiver even when the load is constant. This is because the constant load causes a deflection of the soil surface that follows the moving load, and as the deflected soil surface passes the receiver a transient movement is registered. The response of the soil surface when the constant load moves at a velocity of $v = 0.38c_R$,

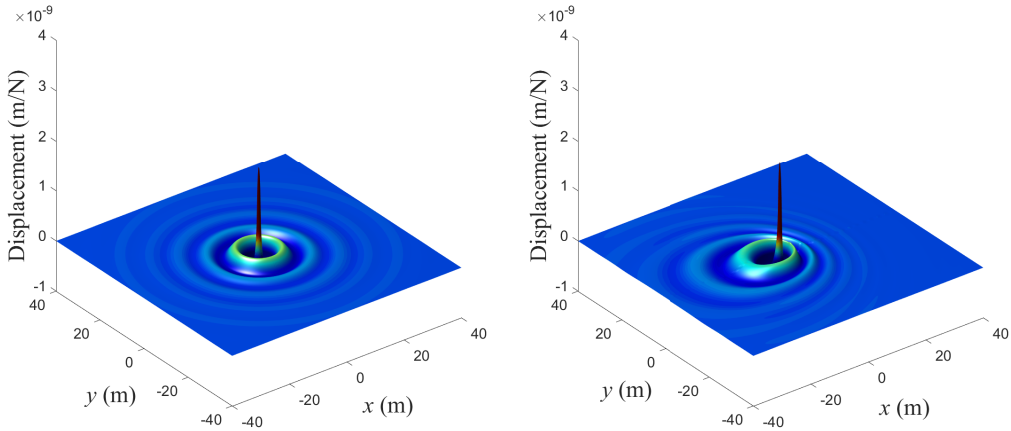

Figure 2.6: Wavefield generated by a harmonic unit load at $f = 40$ Hz that is stationary (a), and moving along the x-axis at the speed $v = 0.38c_R = 100$ m/s (b) .

well below the Rayleigh wave speed in the soil material, is shown in Figure 2.8 (a). When the load velocity approaches the Rayleigh wave speed, the soil displacement increases as shown in Figure 2.8 (b). When the load velocity exceeds the Rayleigh wave speed, a number of waves are generated behind the load, as shown in Figure 2.8 (c). High-speed trains on poor soil conditions, moving at critical speed, close to or faster than the wave speed of the soil material, generating high vibration amplitudes in the track and the surrounding soil, is a well-known phenomenon and has been studied by several researchers. A famous example from Sweden is that of Ledsgård, where the passenger train X-2000 generated very high ground vibrations due to poor soil conditions [8].

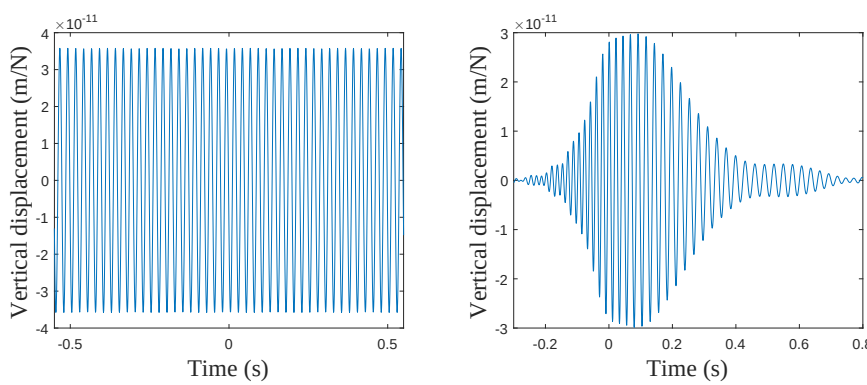

Figure 2.7: Time-history of the displacements in a stationary point 15 m from a harmonic unit load at $f = 40$ Hz that is stationary (a), and moving along the x-axis at the speed $v = 0.38c_R = 100$ m/s (b) .

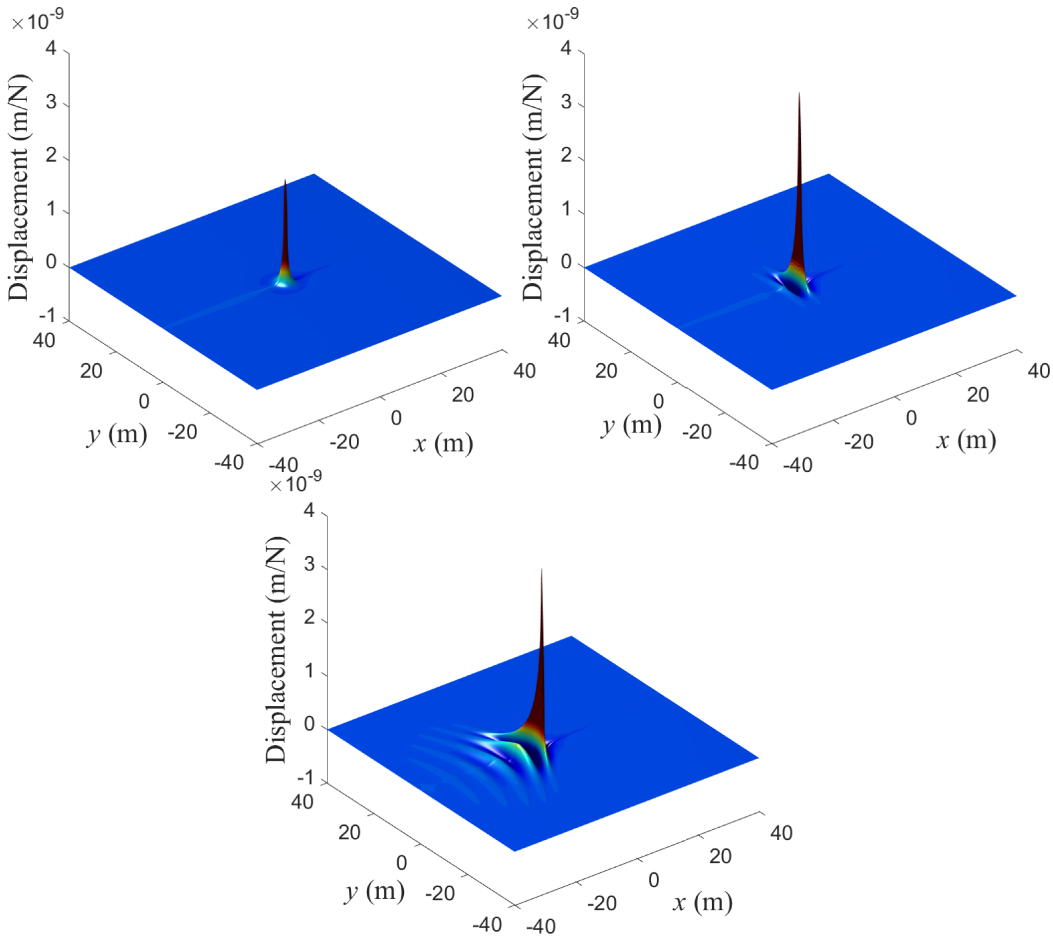

Figure 2.8: Constant unit load moving along the x-axis at the speeds $v = 0.38c_R$ (a), $v = 1.0c_R$ (b) and $v = 1.15c_R$ (c).

2.4 VIBRATION REDUCTION METHODS

With reference to Figure 2.1, measures to reduce the ground-borne vibrations experienced by a receiver may be directed to the source, the transmission path or the receiver.

When vibration mitigation measures are directed to the source, the general idea is to reduce the forces transmitted from the source to the ground. This may be achieved by introducing a resilient element under the source that modifies the transmissibility, i.e. the ratio of the transmitted force to the applied force. This concept is illustrated in Figure 2.9, showing the transmissibility of a single-degree-of-freedom (SDoF) system subjected to a harmonic load. Depending on the relation between the frequency of the applied load, ω, and the resonance frequency of the SDoF system, ω_n, different amounts of the applied load P_0 are transferred

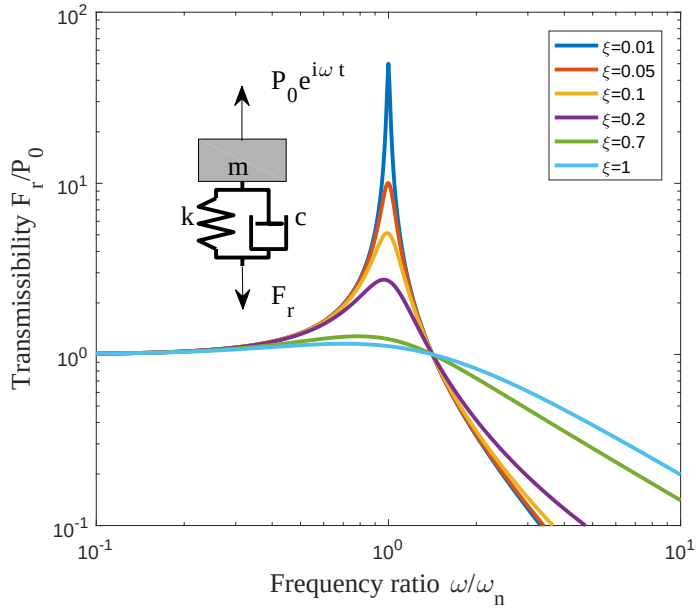

Figure 2.9: Transmissibility for harmonic excitation, for different factors of critical damping ξ. After [9].

to the support. Hence, when a resilient element is introduced under the source, the resonance frequency of the system decreases, increasing the ratio ω/ω_n. For loading frequencies higher than the new resonance frequency of the system, the transmissibility decreases, thereby dynamically isolating the mass. This comes at the cost, however, of an increased transmissibility around the new resonance frequency. Apart from the elastic properties of the resilient element, the transmissibility is governed also by the damping properties, as indicated by the difference between the curves in the diagram.

For railway tracks an example of a resilient element is an elastic mat placed under the ballast, a so called under-ballast mat, in the case of a conventional ballasted track, or underneath the slab in the case of a slab track resulting in a so called floating slab. Resilient elements may also be introduced higher up in the track structure, e.g. in the rail fasteners. However, to dynamically isolate the track for frequencies relevant to ground vibration ($<$ 80 Hz), a large portion of the track mass should be located over the resilient element [10]. The resilient element should, with reference to Figure 2.9, provide a resonance frequency as low as possible for the track structure. A lower limit exists due to limitations in the maximum allowable static deflection. Another way of addressing train-induced ground vibrations at the source, is to improve the soil conditions under the track.

Ground-borne vibrations may also be reduced by modifications in the transmission path between the source and the receiver. Typical examples include trenches and solid barriers, where the

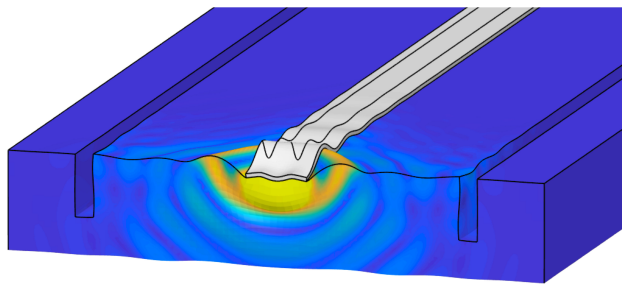

Figure 2.10: A trench between the source and receiver may be an effective means of reducing vibrations.

idea is to shield an area containing the receiver(s) from incoming waves; see Figure 2.10.

Similarly to the case of introducing a resilient layer underneath the source, the receiver may be dynamically isolated through the use of a resilient support. It can be shown that the curves presented in Figure 2.9 for the force transmissibility are identical to those for acceleration transmissibility. In the latter case, the input to the SDOF system is a harmonic acceleration at the support, and the measured response is the acceleration of the mass. In regions prone to earthquakes, seismic base isolation of entire buildings is often based on this principle. However, in the case of environmental vibrations, a more common use of the principle is to dynamically isolate sensitive equipment. Great reductions in the response of the receiver can be achieved by introducing a resilient element at its support. Again, the drawback is the increased transmissibility for excitation frequencies close to the resonance frequency of the isolated receiver.

When evaluating mitigation efforts, the concept of insertion loss (IL) is often used for quantifying the vibration reduction. The insertion loss is expressed in decibels and signifies the difference in power of two signals. The kinetic energy, and hence power p, of a vibrating mechanical system, is proportional to the squared displacement u, i.e.

$$\mathrm{IL} = 10\log\Big(\frac{p_{ref}}{p_{iso}}\Big) = 10\log\Big(\frac{u_{ref}^2}{u_{iso}^2}\Big) = 20\log\Big(\frac{u_{ref}}{u_{iso}}\Big), \tag{2.1}$$

where u_{ref} denotes the displacement obtained for the reference case, without any installed mitigation measure, and u_{iso} denotes the displacement obtained after the installation of a mitigation measure.

2.5 PREDICTING VIBRATIONS FROM RAILWAY TRAFFIC

A prediction model should, based on given input conditions, provide as output an estimation of some sought quantity. Such a model can be empirical; e.g. by using some statistical method of analyzing data, the model predicts the response quantity for given input conditions based

on a large set of previously collected data (conditions and response quantities). Generally, such empirical models do not explain the underlying physics of the predicted response, but rely on that the previously collected data covers all the conditions for the situation to be predicted. Nonetheless, such models can be useful and provide satisfactory results in several situations.

Here, however, focus will be on computational methods with the aim of simulating the generation and propagation of ground-borne vibrations, specifically those generated by railway traffic. For a computational model to provide accurate predictions, it needs detailed descriptions of the source (i.e. the train and the excitation mechanisms), the transmission path, and the receiver. However, a common approach is to use a multi-step procedure for the analysis of the different sub-systems, instead of having one large model simulating the source, the wave propagation in the ground and the receiver response at once. The discussion here is limited to that of the train–track interaction and the resulting wavefield in the ground.

2.5.1 Excitation mechanisms

The vibrations generated by a train moving along a railway track can be divided into a quasi-static contribution and a dynamic contribution. The quasi-static contribution refers to the effect of the moving constant dead load of the train that causes a deflection of the soil surface. As previously described, this moving static deflection of the soil surface is experienced as a transient vibration by a stationary observer next to the track. The dynamic contribution, however, is much more complex and originates from several different mechanisms.

Since the rail is not perfectly smooth, dynamic contact forces arise in the wheel–rail interfaces as the vehicle moves over the rough rail surface. The frequency content of these dynamic contact forces depends on the vehicle speed. A specific rail unevenness component of wavelength λ, generates a dynamic load at frequency $f = v/\lambda$ where v is the vehicle speed. For example, for a vehicle moving at $v = 30$ m/s, dynamic excitation in the frequency range $1 - 80$ Hz result from unevenness wavelengths in the range $0.375 - 30$ m.

Similarly, the wheels are not perfectly round. Out-of-roundness and uneven tear causes periodic dynamic wheel–rail contact forces. These can be severe in the presence of so called wheel-flats. A wheel-flat occurs when the wheel locks during breaking or due to to slippery conditions, causing a flat spot on the wheel that generates large impact forces for each revolution.

Further, dynamic wheel–rail forces are generated by changes in the conditions under the rail along the track, e.g. varying soil- or ballast stiffness. In addition, in most track systems the rail is discretely supported by sleepers, causing a variation of the rail stiffness over the span of one sleeper bay which in turn generates a dynamic excitation at the sleeper-passing frequency $f = v/d$, where d is the sleeper spacing. Other excitation mechanisms include impact excitation due to switches, crossings, joints, etc.

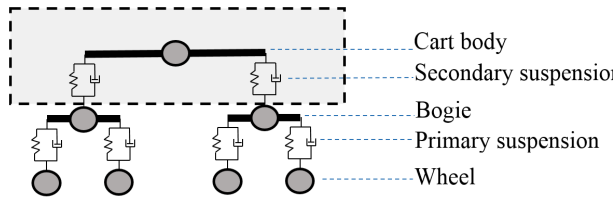

Figure 2.11: Planar vehicle model consisting of lumped masses, springs and dashpots.

2.5.2 Numerical modeling

The calculation of the train–track interaction forces are often carried out using simple 2D multi-body vehicle models where the features most important for the dynamic behavior, such as unsprung/sprung masses and primary/secondary suspensions, are included, see Figure 2.11. The vehicle model is connected to a model of the railway track that should provide an accurate stiffness of the rail, since this stiffness strongly influences the wheel–rail contact forces. Conventional ballasted tracks usually consist of rails supported by rail pads, sleepers and ballast. In slab tracks, the rail can either be continuously or discretely supported. Track models are often 2D finite element models, comprising Bernoulli–Euler or Timoshenko beams representing the rail. In the case of conventional ballasted tracks, the rail is connected to a series of discrete springs, dashpots and masses, representing rail pads, sleepers, ballast and subsoil [11–14]. In models of slab tracks, the rail is usually connected to beam representations of the slab and support layer, with spring and dashpot connections between the layers [15–17].

Analyses of such track models are typically performed in time domain, in a fixed Cartesian coordinate system. Time-domain analyses allow for inclusion of non-linear behavior, for example in the contact condition between the vehicle and the rail. Such models have been used by many different authors to study different mechanisms such as rail unevenness, wheel flats, transition zones, etc. These analyses may be used for studying effects on the track or riding comfort in the vehicle, but the forces obtained in any of the interfaces (e.g. wheel–rail or track–subsoil) may also be used in a subsequent model to study the ground-vibrations generated by these forces, see e.g. [14, 18, 19]. Some authors [15, 20–22] have used similar track models formulated in a moving frame of reference following the vehicle at a fixed speed, by applying a Galilean coordinate transformation to the governing equations. A benefit of such an approach is that the vehicle never leaves the computational domain, enabling the use of a smaller model. Also, the wheel–rail contact formulation becomes less complicated because the wheels interact with the same rail elements throughout the analysis. The coordinate transformation implies that the track is invariant in the track direction, so for example discrete rail supports are modeled as being continuously distributed and track stiffness variation cannot be treated in a straight-forward manner. However, it has been shown [23] that the contribution to the interaction forces, and the resulting free-field vibrations, by the track stiffness variation is much smaller than the contribution from track unevenness. From the excitation mechanisms described in Section 2.5.1, track unevenness is the one most often accounted for in predictions of ground-borne vibrations.

The wave propagation in the ground resulting from the dynamic loads on the track can be calculated using numerous numerical techniques. FEM offers a large flexibility regarding modeling capabilities in terms of geometrical conditions and material properties. However, the need for discretizing a large soil volume, under and between the source and the receiver, can generate very large systems of equations that are time-consuming or practically impossible to solve. The maximum element size is governed by the wavelengths of the propagating waves, and for moving loads these wavelengths decrease in front of the load, requiring a finer mesh. Furthermore, special techniques need to be employed at the fictitious boundaries of the truncated soil volume to avoid spurious reflections of waves. So called impedance boundary conditions [24], which are basically tuned dashpot dampers, can be used to cancel out P- and S-waves impinging orthogonally to the boundary – however, surface waves and P- and S-waves impinging with an angle are partially reflected, compromising the solution, especially close to the truncated ends of the domain. A more recent technique to avoid reflecting waves is the use of a so called perfectly matched layer (PML), which uses a complex coordinate stretching to artificially dampen the incoming waves over a few elements [25].

The boundary element method (BEM) overcomes some of the shortcomings of FEM. For instance, non-reflecting boundaries are inherent to the governing boundary integrals. Furthermore, the soil interior domain does not need to be modeled explicitly, if only the response of the soil surface is required. BEM uses a Green's function (fundamental solution) as a weight function. In the simplest case, the Green's function of a homogeneous full-space is used, requiring discretization of (introduction of elements to) every soil layer interface. Assembling the system matrices is a much more complex and time-consuming procedure than in FEM. For every node of the model, the Green's function for displacement and traction are integrated over the entire boundary. Due to singularities of the Green's functions, this matter is not straight-forward. Furthermore, the system matrices become fully populated. 3D models employing FE or/and BE have been used by a number of researchers to study train-induced vibrations [26–29], and can be used for both time domain and frequency domain analysis.

By assuming constant geometry in the load travel direction, computational savings can be made by applying a so called 2.5D technique, where only a cross section of the soil and railway track is discretized. By means of a Fourier transform with respect to time and the track direction coordinate, a sequence of 2D problems are solved for a number of discrete wavenumbers, and the 3D response is recovered by an inverse Fourier transform of the wavenumber domain response. Such a methodology has been applied to both FE and BE formulations, and mixed BE–FE models, by several authors, see e.g. [30–34].

If the soil is assumed to consist of horizontally oriented visco-elastic layers, a (semi-)analytical approach can be used to obtain the response for a given load in frequency–wavenumber domain, by applying a Fourier transform on the governing equations with respect to the horizontal coordinates and time. The response is then obtained in spatial coordinates by an inverse Fourier transform of the wavenumber domain solution. The accuracy of the solution, and the size of the covered soil surface area, is governed by the size and number of wavenumber increments. Generally, the solution can be obtained at rather large distances from the load, at

a much lower computational effort than with FEM or BEM. Figures 2.5–2.8 were produced using this technique, further described in Section 4.2. A track model can be incorporated into such a semi-analytical model [35–38], and the effect of a vehicle running over an uneven rail can be analyzed in frequency domain by describing the uneveness in terms of its wavenumber content and summing the responses from the excitation from a number of discrete wavenumbers, in the moving frame of reference.

Regardless of the choice of numerical method, large uncertainties are generally associated with predicted ground-borne vibration levels, due to the limited knowledge of the values of the governing parameters. In addition, simplifications are necessary to produce practically feasible models. However, if the most important characteristics of the vibration excitation and transmission path can be identified and modeled, numerical predictions can nevertheless be meaningful for evaluating different designs and mitigation measures.

3 Structural Dynamics and Elastic Waves

3.1 EQUATIONS OF MOTION

By studying the forces acting on an infinitesimal cube within a continuum and applying Newton's second law, it can be shown that independently of the stress–strain behavior of the continuum, equilibrium requires that

$$\frac{\partial \sigma_{ij}}{\partial x_j} + b_i = \rho \frac{\partial^2 u_i}{\partial t^2}, \tag{3.1}$$

which is the Cauchy equation of motion. Here $\sigma_{ij} = \sigma_{ij}(x_1, x_2, x_3, t)$ is the Cauchy stress tensor, $u_i = u_i(x_1, x_2, x_3, t)$ is the displacement in direction i, $b_i = b_i(x_1, x_2, x_3, t)$ is the body forces per unit volume in direction i. Further, $\rho = \rho(x_1, x_2, x_3)$ is the material density, t denotes time and x_j is the coordinate in direction j of the Cartesian space. Note that Eq. (3.1) actually contains three equations, one for each coordinate-direction $i = 1, 2, 3$. As will be shown in Section 4.1, these equations are the starting point when formulating the FE equations for a solid continuum.

Assuming small strains and a linear elastic material behavior, the stress-strain relationship follows Hooke's law,

$$\sigma_{ij}(x_1, x_2, x_3, t) = E_{ijkl}\epsilon_{kl}, \tag{3.2}$$

where E_{ijkl} is the elasticity tensor and the small-strain tensor is

$$\epsilon_{ij} = \epsilon_{ij}(x_1, x_2, x_3, t) = \frac{1}{2}\Big(\frac{\partial u_i}{\partial x_j} + \frac{\partial u_j}{\partial x_i}\Big). \tag{3.3}$$

For a homogeneous material with linear elastic properties, the stress tensor can be written as

$$\sigma_{ij}(x_1, x_2, x_3, t) = \lambda \Delta \delta_{ij} + 2\mu\epsilon_{ij}, \tag{3.4}$$

where λ and μ are the Lame' parameters defined as functions of Young's modulus E and Poisson's ratio v, as

$$\lambda = \tfrac{\nu E}{(1+\nu)(1-2\nu)}, \qquad \mu = \tfrac{E}{2(1+\nu)}. \tag{3.5}$$

Further, δ_{ij} is the Kronecker delta function, and Δ is the dilation defined as

$$\Delta = \Delta(x_1, x_2, x_3, t) = \epsilon_{11} + \epsilon_{22} + \epsilon_{33} = \frac{\partial u_k}{\partial x_k}. \tag{3.6}$$

It can be shown that these definitions together with Eq. (3.1) lead to the Navier equations

$$(\lambda + \mu)\frac{\partial^2 u_j}{\partial x_i \partial x_j} + \mu \frac{\partial^2 u_i}{\partial x_j \partial x_j} + b_i = \rho \frac{\partial^2 u_i}{\partial t^2}, \tag{3.7}$$

which can also be written as

$$(\lambda + \mu)\frac{\partial \Delta}{\partial x_i} + \mu \nabla^2 u_i + b_i = \rho \frac{\partial^2 u_i}{\partial t^2}, \tag{3.8}$$

with the Laplacian operator ∇^2 defined as

$$\nabla^2 = \frac{\partial^2}{\partial x_1^2} + \frac{\partial^2}{\partial x_2^2} + \frac{\partial^2}{\partial x_3^2} = \frac{\partial^2}{\partial x_j \partial x_j}. \tag{3.9}$$

3.2 STRUCTURAL DYNAMICS

A linearly elastic mechanical system can be described by its mass, elastic and damping properties. The simplest possible system having all these three properties is the so called single-degree-of-freedom (SDoF) system shown in Figure 3.1, consisting of a mass, a (weightless) spring and a (weightless) viscous damper (dashpot). The degree-of-freedom (DoF) refers to the possible movement of the mass, which in this example is constrained to the horizontal axis. The elastic force in the spring is proportional to the displacement u of the mass and the spring stiffness k, i.e. $f_e = ku$, whereas the force in the dashpot is proportional to the velocity $\dot{u}$ of the mass and the damping coefficient c, i.e. $f_d = c\dot{u}$. Using d'Alemberts principle, the inertia force of the mass m is proportional to the acceleration $\ddot{u}$, i.e. $f_i = m\ddot{u}$ and acting in the opposite direction of the acceleration. When a time dependent external load $p(t)$ is applied to the mass,

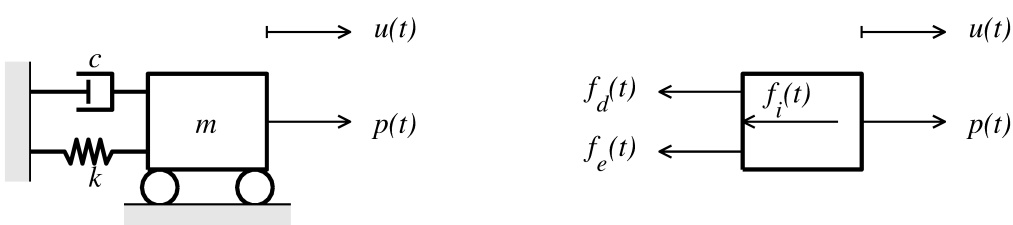

Figure 3.1: Single-degree-of-freedom system subjected to a time-dependent force $p(t)$. After [39].

the equation of motion for the mass is obtained by expressing the equilibrium of the forces acting on it, as

$$f_i(t) + f_d(t) + f_e(t) = p(t), \tag{3.10}$$

which, by using the previous expressions for the individual components, can be written as

$$m\ddot{u}(t) + c\dot{u}(t) + ku(t) = p(t). \tag{3.11}$$

For a multi-degree-of-freedom (MDoF) system involving several components, the equation of motion for that system can be written as

$$\mathbf{M}\ddot{\mathbf{u}}(t) + \mathbf{C}\dot{\mathbf{u}}(t) + \mathbf{K}\mathbf{u}(t) = \mathbf{p}(t), \tag{3.12}$$

where $\mathbf{M}$, $\mathbf{C}$ and $\mathbf{K}$ are the systems mass, damping and stiffness matrices, respectively. Further, $\ddot{\mathbf{u}}(t)$, $\dot{\mathbf{u}}(t)$, $\mathbf{u}(t)$, and $\mathbf{p}(t)$ denote vectors containing the acceleration, velocity, displacement and external loading, respectively, for each DoF. In fact, this is also the system of equations that is solved when applying the FE method as described in Section 4.1.

3.2.1 Free vibration

When no external loading acts on the SDoF system, the solution $u(t)$ to the homogeneous equation

$$m\ddot{u}(t) + c\dot{u}(t) + ku(t) = 0, \tag{3.13}$$

is found on the form

$$u(t) = Ge^{st}, \tag{3.14}$$

where G is an arbitrary complex constant. By noting that $\dot{u}(t) = sGe^{st}$ and $\ddot{u}(t) = s^2Ge^{st}$, insertion into Eq. (3.13) yields

$$(ms^2 + cs + k)Ge^{st} = 0. \tag{3.15}$$

Non-trivial solutions require that $ms^2 + cs + k = 0$, which can be written as

$$s^2 + \frac{c}{m}s + \omega_n^2 = 0, \tag{3.16}$$

where the variable

$$\omega_n = \sqrt{\frac{k}{m}}, \tag{3.17}$$

has been introduced. The solutions s to Eq. (3.16) are found as

$$s_{1,2} = -\frac{c}{2m} \pm \sqrt{\left(\frac{c}{2m}\right)^2 - \omega_n^2}. \tag{3.18}$$

If no damping is present, i.e. $c = 0$, then

$$s_{1,2} = \pm\sqrt{-\omega_n^2} = \pm \mathrm{i}\omega_n, \tag{3.19}$$

where i is the imaginary unit, $\mathrm{i} = \sqrt{-1}$, and it can be shown [39] that the resulting motion $u(t)$ may be written as

$$u(t) = A\cos(\omega_n t + \phi), \tag{3.20}$$

where the real constant A and the phase angle ϕ depend on the initial conditions. Further, it is seen that ω_n is the frequency of vibration, i.e. the natural frequency of the undamped SDoF system.

When damping is present, the nature of the solution depends on the relation of the damping coefficient c to the mass m and stiffness k. When the expression under the square root sign in Eq. (3.18) becomes zero, i.e.

$$c = c_c = 2m\omega_n, \tag{3.21}$$

the system is said to be critically damped, and the resulting free vibration does not contain any oscillations, but returns asymptotically to rest as

$$u(t) = (A + Bt)e^{-\omega_n t}, \tag{3.22}$$

where A and B are real constants determined from the initial conditions [39].

The damping ratio ξ is defined as

$$\xi = \frac{c}{c_c}. \tag{3.23}$$

When $\xi < 1$, the system is said to be underdamped and the free vibration is obtained as

$$u(t) = A\cos(\omega_D t + \phi)e^{-\xi\omega_n t}, \tag{3.24}$$

where $\omega_D = \omega_n\sqrt{1-\xi^2}$ is the damped frequency of vibration, and the real constant A and phase angle ϕ are determined from the initial conditions.

For the undamped case of the MDoF system, the homogeneous differential equation

$$\mathbf{M}\ddot{\mathbf{u}}(t) + \mathbf{K}\mathbf{u}(t) = 0, \tag{3.25}$$

is solved by assuming a harmonic solution of the form $\mathbf{u}(t) = \mathbf{\Phi}\hat{U}e^{\mathrm{i}\omega t}$, where $\mathbf{\Phi}$ is a constant vector, $\hat{U}$ is a complex amplitude and ω is the angular frequency of vibration. Inserting the assumed solution into Eq. (3.25) yields

$$(-\omega^2\mathbf{M} + \mathbf{K})\mathbf{\Phi}\hat{U}e^{\mathrm{i}\omega t} = 0, \tag{3.26}$$

and non-trivial solutions require that

$$\det(-\omega^2\mathbf{M} + \mathbf{K}) = 0. \tag{3.27}$$

If the system has N DoFs, then N solutions to Eq. (3.27) exist, with the eigenvalues (natural frequencies) $\omega_i = \omega_1, .., \omega_N$ and corresponding eigenvectors (natural modes, eigenmodes)

$\mathbf{\Phi}_i = \mathbf{\Phi}_1, .., \mathbf{\Phi}_N$. The modes can be used as base vectors for describing any displacement of the system as

$$\mathbf{u}(t) = \sum_{i=1}^{i=N} q_i(t)\mathbf{\Phi}_i, \tag{3.28}$$

where $q_i(t)$ is the modal coordinate. Further, the modes are mass and stiffness orthogonal, and can be used for diagonalizing the mass and stiffness matrices, providing a set of N uncoupled equations. Hence, the response of each mode can solved separately, analogously to a SDoF system and the total system response is obtained by Eq. (3.28). This is also true for a damped MDoF system, if so called classical damping is utilized, meaning that the modes also diagonalize the damping matrix.

3.2.2 Steady-state response to harmonic loading

When a SDoF system is subjected to a harmonic load, i.e. $p(t) = \hat{p}e^{\mathrm{i}\omega t}$, the steady-state solution to Eq. (3.11) is found by assuming that the response is also harmonic with the excitation frequency, i.e. $u(t) = \hat{u}e^{\mathrm{i}\omega t}$. Insertion into Eq. (3.11) yields

$$(-\omega^2 m + \mathrm{i}\omega c + k)\hat{u} = \hat{p}, \tag{3.29}$$

or equivalently

$$\hat{u} = \frac{\hat{p}}{(-\omega^2 m + \mathrm{i}\omega c + k)}. \tag{3.30}$$

Using Eq. (3.21) and Eq. (3.23), this can be written as

$$\hat{u} = \frac{\hat{p}}{k(1 - \frac{\omega^2}{\omega_n^2} + 2\mathrm{i}\frac{\omega}{\omega_n}\xi)}. \tag{3.31}$$

The steady-state forces in the spring and dashpot are $f_e = ku = k\hat{u}e^{\mathrm{i}\omega t}$ and $f_d = c\dot{u} = \mathrm{i}\omega c\hat{u}e^{\mathrm{i}\omega t}$, respectively, and hence the total reaction force becomes

$$f_r = f_e + f_d = \frac{(k + \mathrm{i}\omega c)\hat{p}}{k(1 - \frac{\omega^2}{\omega_n^2} + 2\mathrm{i}\frac{\omega}{\omega_n}\xi)} = \frac{(1 + 2\mathrm{i}\xi\frac{\omega}{\omega_n})\hat{p}}{(1 - \frac{\omega^2}{\omega_n^2} + 2\mathrm{i}\frac{\omega}{\omega_n}\xi)}. \tag{3.32}$$

When divided by $\hat{p}$, this provides the transmissibility of the SDoF system, i.e. the ratio of the reaction force to the applied force. In Figure 2.9 this expression is plotted for different values of ω/ω_n and ξ .

The transfer function $H(\omega)$, or frequency response function (FRF), of the SDoF system is obtained by dividing Eq. (3.31) by $\hat{p}$,

$$H(\omega) = \frac{\hat{u}}{\hat{p}} = \frac{1}{k(1 - \frac{\omega^2}{\omega_n^2} + 2\mathrm{i}\frac{\omega}{\omega_n}\xi)}, \tag{3.33}$$

giving the complex displacement response of the SDoF system due to a unit load of frequency ω. Clearly, for zero damping, $\xi = 0$, the response goes to infinity for $\omega = \omega_n$.

For the MDoF system, governed by Eq. (3.12), subjected to harmonic loading, $\mathbf{p}(t) = \hat{\mathbf{p}}e^{\mathrm{i}\omega t}$, harmonic response is assumed as $\mathbf{u}(t) = \hat{\mathbf{u}}e^{\mathrm{i}\omega t}$. Here, each element of the vectors $\hat{\mathbf{p}}$ and $\hat{\mathbf{u}}$ are complex numbers. Similarly to the SDoF system, the following equation is obtained by insertion of the assumed solution into Eq. (3.12),

$$(-\omega^2\mathbf{M} + \mathrm{i}\omega\mathbf{C} + \mathbf{K})\hat{\mathbf{u}} = \mathbf{D}(\omega)\hat{\mathbf{u}} = \hat{\mathbf{p}}, \tag{3.34}$$

where the dynamic stiffness matrix, $\mathbf{D}(\omega) = (-\omega^2\mathbf{M} + \mathrm{i}\omega\mathbf{C} + \mathbf{K})$ has been introduced. The solution $\hat{\mathbf{u}}$ is obtained as

$$\hat{\mathbf{u}} = \mathbf{D}^{-1}(\omega)\hat{\mathbf{p}}. \tag{3.35}$$

The inverse of the dynamic stiffness matrix, $\mathbf{D}^{-1}(\omega)$, contains transfer functions between the different DoFs; i.e. element (i, j) of $\mathbf{D}^{-1}(\omega)$ contains the response in DoF i, due to a unit harmonic load applied at DoF j.

3.2.3 Frequency-independent damping

Damping generally refers to a mechanism in which mechanical energy is being dissipated, causing a reduction of the vibration response. Material damping, more specifically, refers to the dissipation of mechanical energy within the material due to internal mechanisms. To model such energy dissipation mathematically, the stress in the material is assumed to consist of an elastic part depending on the strain level, and a viscous part depending on the strain-rate. Using the analogy of a SDoF system, the elastic part refers to the force in the spring and the viscous part refers to force in the dashpot. With harmonic displacement loading, i.e.

$$u = u_0 e^{\mathrm{i}\omega t}, \tag{3.36}$$

the sum of the elastic and viscous force can be written as

$$f_r = \Big(ku_0 + \mathrm{i}\omega c u_0\Big)e^{\mathrm{i}\omega t}. \tag{3.37}$$

One cycle of vibration generates an ellipse in the force–displacement diagram, the hysteresis loop, as indicated in Figure 3.2. The area within the hysteresis loop signifies the energy dissipated over the cycle. The dissipated energy over one cycle of vibration is calculated as

$$\Delta W = \int_0^{\frac{2\pi}{\omega}} f_r \frac{\partial u}{\partial t}\mathrm{d}t = \pi c\omega u_0^2. \tag{3.38}$$

The maximum strain energy stored during one cycle is $W_s = \frac{1}{2}ku_0^2$, and it can be shown [40] that the dissipated energy ΔW is related to the damping factor ξ through the maximum strain energy W_s as

$$\xi = \frac{1}{4\pi}\frac{\Delta W}{W_s} = \frac{c\omega}{2k}. \tag{3.39}$$

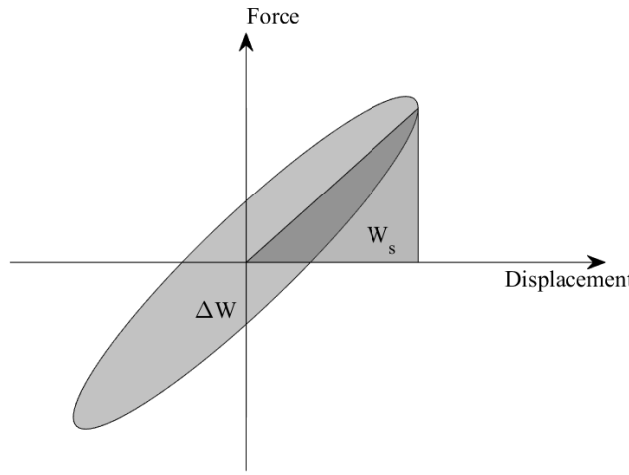

Figure 3.2: Hysteresis loop showing the dissipated energy ΔW during one cycle of vibration and the maximum strain energy W_s.

Here it is seen that the damping factor is proportional to the frequency of the loading ω. To obtain a frequency-independent damping, the damping coefficient c is expressed using Eq. (3.39), as

$$c = \frac{2k\xi}{\omega}. \tag{3.40}$$

Insertion of this expression for c into Eq. (3.37) yields

$$f_r = \Big(ku_0 + \mathrm{i}\omega c u_0\Big)e^{\mathrm{i}\omega t} = k\Big(1 + 2\mathrm{i}\xi\Big)u_0 e^{\mathrm{i}\omega t} = k^* u_0 e^{\mathrm{i}\omega t}. \tag{3.41}$$

Here, $k^* = k\Big(1 + 2\mathrm{i}\xi\Big) = k\Big(1 + \mathrm{i}\eta\Big)$ is the complex stiffness, and $\eta = 2\xi$ is known as the loss factor. Now, Eq.(3.40) can be written as

$$c = \frac{k\eta}{\omega}. \tag{3.42}$$

Generalizing Eq. (3.42) to a MDoF system gives

$$\mathbf{C} = \mathbf{K}\frac{\eta}{\omega}, \tag{3.43}$$

which inserted into Eq. (3.34) provides

$$\Big(-\omega^2\mathbf{M} + \mathrm{i}\omega\mathbf{C} + \mathbf{K}\Big)\hat{\mathbf{u}} = \Big(-\omega^2\mathbf{M} + \mathbf{K}(1 + \mathrm{i}\eta)\Big)\hat{\mathbf{u}} = \mathbf{D}(\omega)\hat{\mathbf{u}} = \hat{\mathbf{p}}, \tag{3.44}$$

with the dynamic stiffness defined as $\mathbf{D}(\omega) = -\omega^2\mathbf{M} + \mathbf{K}(1 + \mathrm{i}\eta)$. This type of frequency-independent damping is often referred to as structural damping.

3.3 ELASTIC WAVES

3.3.1 Wave propagation in structural elements

A disturbance of the static equilibrium of a structural element causes a stress field to propagate through the member as elastic waves. Different wave types propagate with different phase velocities that may or may not depend on the frequency. When the phase velocity depends on the frequency, the waves are called dispersive. When waves are dispersive, a pulse of waves with different frequencies will spread, or disperse, due to the different propagation velocities.

Longitudinal waves in an infinite rod

First, a simple case of an infinite rod with constant Young's modulus E, section area A and density ρ is considered. The equation for the rod can be written as

$$EA\frac{\partial^2 u(x,t)}{\partial x^2} + p(x,t) = \rho A\frac{\partial^2 u(x,t)}{\partial t^2}, \tag{3.45}$$

where $u = u(x,t)$ is the displacement of the rod at position x and time t, and $p(x,t)$ denotes an external force. The homogeneous equation, i.e. without external force, can then be written as

$$EA\frac{\partial^2 u(x,t)}{\partial x^2} - \rho A\frac{\partial^2 u(x,t)}{\partial t^2} = 0, \tag{3.46}$$

or equivalently

$$\frac{\partial^2 u(x,t)}{\partial x^2} - \frac{1}{c^2}\frac{\partial^2 u(x,t)}{\partial t^2} = 0. \tag{3.47}$$

Here, the variable $c = \sqrt{\frac{E}{\rho}}$ has been introduced. This is the one-dimensional wave equation. It is easily checked that both the functions $\phi(x-ct)$ and $\psi(x+ct)$ satisfy the equation. The shape of the functions $\phi(x-ct)$ and $\psi(x+ct)$ do not change. They represent a displacement field that propagates as a wave along the x-axis in the positive and negative direction, respectively, with the speed c [41]. Hence, for the rod, waves propagate with the so called phase velocity $c = \sqrt{\frac{E}{\rho}}$. Now, it is assumed that the solution is harmonic in time, i.e. a complex solution is prescribed as $u(x,t) = \tilde{u}(x)e^{\mathrm{i}\omega t}$. Here, ω is the circular frequency of vibration. Insertion into Eq. (3.46) and rearranging yields

$$\frac{\partial^2 \tilde{u}(x)}{\partial x^2} + \frac{\rho}{E}\omega^2\tilde{u}(x) = 0. \tag{3.48}$$

This is a second-order differential equation, and solutions are of the form $\tilde{u}(x) = Ce^{ikx}$. Using this expression in Eq. (3.48) yields the dispersion relation,

$$k^2 - \frac{\rho}{E}\omega^2 = 0, \tag{3.49}$$

which has two roots. Both roots are real, $k_{1,2} = \pm\omega\sqrt{\frac{\rho}{E}} = \pm k_L$. The general solution to Eq. (3.46) is therefore

$$u(x,t) = C_1 e^{(\mathrm{i}\omega t + \mathrm{i}k_L x)} + C_2 e^{(\mathrm{i}\omega t - \mathrm{i}k_L x)}, \tag{3.50}$$

where the two terms represent harmonic waves propagating in the negative and positive directions, respectively, of the $x-$axis. This becomes clear if the phase of the first exponential is studied. For a certain time t_0 and position along the rod x_0, the phase is

$$\xi = \omega t_0 + k_L x_0. \tag{3.51}$$

At a later instant in time, $t_1 = t_0 + \Delta t$, this phase is found at $x_1 = x_0 + \Delta x$, i.e

$$\xi = \omega(t_0 + \Delta t) + k_L(x_0 + \Delta x). \tag{3.52}$$

Subtracting Eq. (3.51) from Eq. (3.52) yields

$$\Delta x = -\frac{\omega}{k_L}\Delta t. \tag{3.53}$$

Since k_L is positive and real, Δx is negative, i.e. the wave has propagated in the negative $x-$direction, and it has done so with the phase velocity $c_L = \omega/k_L = \sqrt{E/\rho}$. The term k_L is called the longitudinal wavenumber and it is related to the wavelength λ_L as $k_L = 2\pi/\lambda_L$.

The fact that the phase velocity does not depend on the frequency ω, means that the longitudinal waves are non-dispersive. As shown in the next section, the situation is different for flexural waves.

Transversal waves in an infinite Bernoulli beam

For a uniform Bernoulli–Euler beam, the homogeneous equation can be written as

$$EI\frac{\partial^4 w(x,t)}{\partial x^4} + \rho A\frac{\partial^2 w(x,t)}{\partial t^2} = 0, \tag{3.54}$$

where EI is the bending stiffness, ρ is the mass density, A is the cross-section area and w is the vertical displacement. As for the rod in the previous section, a harmonic solution is assumed as $w(x,t) = \tilde{w}(x)e^{\mathrm{i}\omega t}$. Insertion into Eq. (3.54) yields

$$\frac{\partial^4 \tilde{w}(x)}{\partial x^4} + \frac{\rho A}{EI}\omega^2\tilde{w}(x) = 0, \tag{3.55}$$

to which solutions are of the form $\tilde{w}(x) = Ce^{\mathrm{i}kx}$. Using this expression in Eq. (3.55) yields the dispersion relation,

$$k^4 - \frac{\rho A}{EI}\omega^2 = 0. \tag{3.56}$$

This equation has two real and two imaginary roots; $k_{1,2} = \pm k_B$ and $k_{3,4} = \pm \mathrm{i}k_B$ where $k_B = \sqrt{\omega}\left(\frac{\rho A}{EI}\right)^{1/4}$ is the flexural wavenumber. The general solution to Eq. (3.54) is therefore

$$w(x,t) = C_1 e^{(\mathrm{i}\omega t + \mathrm{i}k_B x)} + C_2 e^{(\mathrm{i}\omega t - \mathrm{i}k_B x)} + C_3 e^{(\mathrm{i}\omega t - k_B x)} + C_4 e^{(\mathrm{i}\omega t + k_B x)}. \tag{3.57}$$

Here, the terms involving C_1 and C_2 represent propagating waves, whereas the two remaining terms represent evanescent waves. The phase velocity is $c_B = \frac{\omega}{k_B} = \sqrt{\omega}\left(\frac{EI}{\rho A}\right)^{1/4}$. The phase velocity is frequency-dependent, i.e. the flexural waves are dispersive.

3.3.2 Wave propagation in an elastic continuum

In Section 3.1 the Navier equations, expressing the equation of motion for a homogeneous, linearly elastic continuum, was presented. Disregarding body forces, the Navier equations become

$$(\lambda + \mu)\frac{\partial^2 u_j}{\partial x_i \partial x_j} + \mu \frac{\partial^2 u_i}{\partial x_j \partial x_j} = \rho \frac{\partial^2 u_i}{\partial t^2}. \tag{3.58}$$

For a homogeneous infinite domain, i.e. a so called full-space, there are two different solutions to this equation: the dilational P-wave and the equivoluminal S-wave. These are called body waves. However, for a homogeneous domain with a free surface, i.e. a so called half-space, a coupling occurs between the P-wave and the S-wave. This coupling results in a surface wave, the Rayleigh wave, propagating in a direction parallel with the surface.

The P-wave

It can be shown [6] that by taking the divergence of Eq. (3.58), a scalar wave equation is obtained in terms of the previously defined dilation $\Delta(x_1, x_2, x_3, t)$, as

$$\frac{\partial^2 \Delta}{\partial x_k \partial x_k} = \frac{1}{c_p^2}\frac{\partial^2 \Delta}{\partial t^2}, \tag{3.59}$$

with

$$c_p = \sqrt{\frac{\lambda + 2\mu}{\rho}}. \tag{3.60}$$

This means that the solution to Eq. (3.59) represents a wave where the dilation Δ propagates with the velocity c_p. This wave is frequently called the P-wave, pressure wave, or primary wave, where primary refers to the fact that it is the fastest traveling wave and hence the first wave to arrive at a receiver.

The S-wave

Taking the rotation of Eq. (3.58), leads to the following three-dimensional wave equation [6]

$$\frac{\partial^2 w_i}{\partial x_j \partial x_j} = \frac{1}{c_s^2}\frac{\partial^2 w_i}{\partial t^2}, \tag{3.61}$$

where $w_i = w_i(x_1, x_2, x_3, t)$ denotes the rotation of the displacement field, defined as

$$w_1 = \tfrac{1}{2}(\tfrac{\partial u_3}{\partial x_2} - \tfrac{\partial u_2}{\partial x_3}), \qquad w_2 = \tfrac{1}{2}(\tfrac{\partial u_1}{\partial x_3} - \tfrac{\partial u_3}{\partial x_1}), \qquad w_3 = \tfrac{1}{2}(\tfrac{\partial u_2}{\partial x_1} - \tfrac{\partial u_1}{\partial x_2}), \tag{3.62}$$

and

$$c_s = \sqrt{\frac{\mu}{\rho}}. \tag{3.63}$$

The solution to Eq. (3.61) describes the propagation of a pure rotational wave, with the phase speed c_s. This wave is usually called the S-wave, shear wave or secondary wave. The particle motion is perpendicular to the propagation direction. Often the S-wave is divided into two components of horizontal and vertical motion, referred to as SH- and SV-waves.

The Rayleigh wave

Here, a plane surface wave propagating in the positive x_1-direction of a homogeneous half-space is considered. The depth coordinate, x_3, is pointing into the interior of the half-space. The particle displacement is independent of the x_2-coordinate. The displacements in the x_1- and x_3-directions are now expressed in terms of two potential functions Φ and Ψ:

$$u_1 = \frac{\partial \Phi}{\partial x_1} + \frac{\partial \Psi}{\partial x_3}, \qquad u_3 = \frac{\partial \Phi}{\partial x_3} - \frac{\partial \Psi}{\partial x_1}, \tag{3.64}$$

which inserted into Eq. (3.58) yields the two equations [6]

$$\nabla^2 \Phi = \frac{1}{c_p^2}\frac{\partial^2 \Phi}{\partial t^2}, \qquad \nabla^2 \Psi = \frac{1}{c_s^2}\frac{\partial^2 \Psi}{\partial t^2}. \tag{3.65}$$

The wavefield is allowed to propagate along the x_1-axis only. Harmonic solutions to Eqs. (3.65) are therefore sought in the form

$$\Phi = F(x_3)e^{\mathrm{i}(\omega t - k_R x_1)}, \qquad \Psi = G(x_3)e^{\mathrm{i}(\omega t - k_R x_1)}, \tag{3.66}$$

where $F(x_3)$ and $G(x_3)$ are amplitude functions, and k_R is the wavenumber of the Rayleigh wave, $k_R = 2\pi/\lambda_R$. Insertion of these expressions into Eq. (3.65) leads to the following ordinary differential equations for F and G,

$$\frac{\mathrm{d}^2 F(x_3)}{\mathrm{d}x_3^2} - \gamma_p^2 F(x_3) = 0, \qquad \frac{\mathrm{d}^2 G(x_3)}{\mathrm{d}x_3^2} - \gamma_s^2 G(x_3) = 0, \tag{3.67}$$

where $\gamma_p^2 = k_R^2 - k_p^2$ and $\gamma_s^2 = k_R^2 - k_s^2$. The solution to Eqs. (3.67) are sought on the form

$$F(x_3) = A_1 e^{(-\gamma_p x_3)} + B_1 e^{(\gamma_p x_3)}, \quad G(x_3) = A_2 e^{(-\gamma_s x_3)} + B_2 e^{(\gamma_s x_3)}. \tag{3.68}$$

The constants $B_1 = B_2 = 0$, since an amplitude increasing to infinity with the depth coordinate x_3 is physically invalid. Hence, from Eqs. (3.66) and (3.68), the following expressions are obtained for the potential functions

$$\Phi = A_1 e^{(-\gamma_p x_3)} e^{\mathrm{i}(\omega t - k_R x_1)}, \quad \Psi = A_2 e^{(-\gamma_s x_3)} e^{\mathrm{i}(\omega t - k_R x_1)}. \tag{3.69}$$

The free surface is traction free, i.e. $\sigma_{33} = \sigma_{13} = 0$. Using these boundary conditions, with the expression for the stress tensor in Eq. (3.4), the displacements in Eq. (3.64), and the potentials in Eq. (3.69), the following relations are obtained

$$\begin{aligned} &\frac{A_1}{A_2}\frac{(\lambda + 2\mu)\gamma_p^2 - \lambda k_R^2}{2\mathrm{i}\mu k_R \gamma_S} - 1 = 0, \\ &\frac{A_1}{A_2}\frac{2\gamma_p \mathrm{i} k_R}{\gamma_s^2 + k_R^2} + 1 = 0. \end{aligned} \tag{3.70}$$

It can be shown [6] that from these relations, the following expression may be obtained relating the Rayleigh wave velocity c_R and the S-wave velocity c_s,

$$K^6 - 8K^4 + (24 - 16\alpha^2)K^2 + 16(\alpha^2 - 1) = 0, \tag{3.71}$$

where $K = \frac{c_R}{c_s}$ and $\alpha = \frac{c_s}{c_p}$. The relation between the Poisson's ratio, and the phase velocities of the P-, S- and Rayleigh waves are shown in Figure 3.3 (left). The phase velocity of the Rayleigh wave is frequency independent, i.e. the Rayleigh wave is non-dispersive.

Inserting the potential functions in Eq. (3.69) into Eq. (3.64) yields the following expressions for the displacements,

$$\begin{aligned} u_1 &= -A_1 \mathrm{i} k_R e^{(-\gamma_p x_3)} e^{\mathrm{i}(\omega t - k_R x_1)} - A_2 \gamma_s e^{(-\gamma_s x_3)} e^{\mathrm{i}(\omega t - k_R x_1)}, \\ u_3 &= -A_1 \gamma_p e^{(-\gamma_p x_3)} e^{\mathrm{i}(\omega t - k_R x_1)} + A_2 \mathrm{i} k_R e^{(-\gamma_s x_3)} e^{\mathrm{i}(\omega t - k_R x_1)}. \end{aligned} \tag{3.72}$$

Using the relation between A_1 and A_2 established in Eq. (3.70), these displacements may be written as

$$\begin{aligned} u_1 &= A_1 \mathrm{i} k_R \Big(- e^{(-\gamma_p x_3)} + \frac{2\gamma_s \gamma_p}{\gamma_s^2 + k_R^2} e^{(-\gamma_s x_3)} \Big) e^{\mathrm{i}(\omega t - k_R x_1)}, \\ u_3 &= A_1 k_R \Big(- \frac{\gamma_p}{k_R} e^{(-\gamma_p x_3)} + \frac{2\gamma_p k_R}{\gamma_s^2 + k_R^2} e^{(-\gamma_s x_3)} \Big) e^{\mathrm{i}(\omega t - k_R x_1)}. \end{aligned} \tag{3.73}$$

The terms inside the main brackets signify the difference in amplitudes for the horizontal and vertical particle motion. The presence of i in u_1 means that the horizontal particle motion is out-of-phase with the vertical motion by 90°, indicating that the particle movement follows an elliptical path. The relative amplitudes of the horizontal and vertical particle motion is shown in Figure 3.3 (right), for various values of Poisson's ratio.

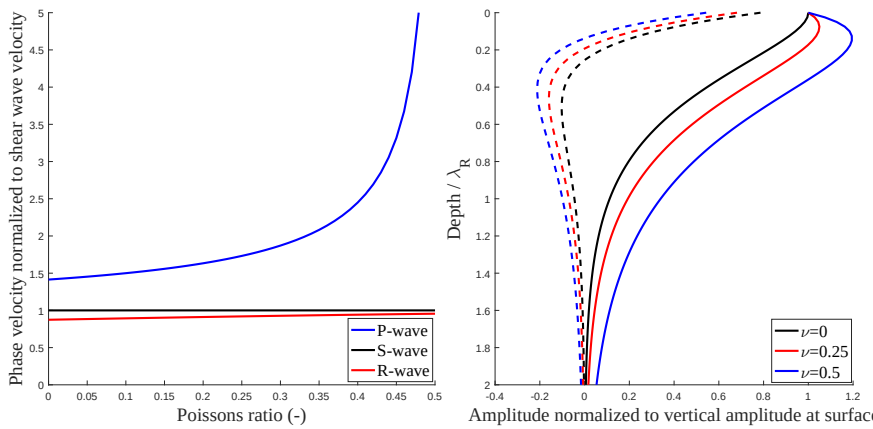

Figure 3.3: Left: Relation between Poisson's ratio and phase velocities of the P-, S- and Rayleigh wave. Right: Relative amplitudes of vertical (solid) and horizontal (dashed) particle motion in Rayleigh wave for various Poisson's ratio.

Damping

For soils, material damping effects occur due to friction between particles and structural rearrangement of the particles. Experimental studies suggests that the damping ratio is rather insensitive to the frequency of vibration. Hence, in computational models, soil material damping is most often introduced as a loss factor by using complex stiffness values as described in Section 3.2.3.

Another form of "damping" relevant for ground vibrations, is the attenuation of the vibration response at an increasing distance from the source, which is due to the spreading of the energy over a successively larger domain. This is usually called geometrical damping or geometrical attenuation. P- and S-waves originating from a point source on the soil surface spread radially with hemi-spherical wavefronts. At the time t the distance to the wave front, i.e. the radius of the half-sphere, is $r = c \times t$ and the surface area of the half-sphere is $2\pi r^2$. The amount of energy contained in the wavefront does not change, meaning that the energy density is inversely proportional to the wavefront surface area. Hence, the energy of body waves spreads as $1/r^2$. Since the mechanical energy (strain energy + kinetic energy) is proportional to the squared displacements, the displacement amplitude of body waves decreases as $1/r$. However, when the source is a line load, the body waves spread radially with cylindrical wavefronts, and by the same reasoning the energy and displacement amplitude can be shown to decrease as $1/r$ and $1/\sqrt{r}$, respectively. Surface waves that originate from a point source on the soil surface, spread radially along the surface with circular wavefronts, with the energy density being proportional to the wavefront circumference. Hence, the energy of Rayleigh waves decreases as $1/r$, and the displacement amplitude decreases as $1/\sqrt{r}$. In the case of a line load, there is no geometrical attenuation at all of the surface waves [42].

4 Numerical Solution Methods

In the current work, several numerical solution methods have been used for calculating the ground vibrations from loads on a railway track. Various formulations of the finite element method, described in Section 4.1, has been used for modeling the railway track. To model the wave propagation in the ground, a time efficient semi-analytical method described in Section 4.2 has been used as well as finite element modeling of the soil domain. The coupling of the methods used for the track and soil is described in Chapter 5.

4.1 THE FINITE ELEMENT METHOD

4.1.1 General remarks

In physics and engineering, many phenomena are mathematically described by partial differential equations (PDEs). Analytical solutions to such PDEs can usually only be found for very simple geometries, domain properties, boundary conditions and loads. For more complex cases, numerical methods are employed to find approximations to the true solution. One commonly used method is the finite element method (FEM), in which the computational domain is divided into smaller elements forming an element mesh. Each element is geometrically defined by its nodes, and in the general case also by some function defining the element boundary between the nodes. The physical field is discretized onto the nodes, and inside each element the field is assumed to vary according to some predefined function which is usually a simple polynomial function. The method is very versatile and can be formulated to account for very complex behavior such as geometric and material non-linearities etc.

The FE formulation leads to a system of equations where the values of the physical field in the nodes are the unknowns. Smaller elements in general lead to a more accurate solution, since the error due to the assumed variation within each element decreases. At the same time the computational cost increases, because the size of the system of equations increases with increasing number of nodes. For problems where the physical field is a scalar function, e.g. temperature, each node has only one degree-of-freedom (DoF). However, for problems where the physical field is a vector function, such as structural mechanics problems, each node is gen-

erally associated with a number of DoFs, e.g. the displacements in the (x_1, x_2, x_3)-directions. As mentioned in Section 3.2, the system of equations obtained when applying the FE method can be written as

$$\mathbf{M}\ddot{\mathbf{u}}(t) + \mathbf{C}\dot{\mathbf{u}}(t) + \mathbf{K}\mathbf{u}(t) = \mathbf{f}(t). \tag{4.1}$$

Here, $\mathbf{M}$, $\mathbf{C}$ and $\mathbf{K}$ are the mass, damping and stiffness matrices, respectively. These matrices are $(N \times N)$, where N is the number of DoFs. Further, $\ddot{\mathbf{u}}(t)$, $\dot{\mathbf{u}}(t)$, $\mathbf{u}(t)$, and $\mathbf{f}(t)$ are $(N \times 1)$ column vectors containing the acceleration, velocity, displacement and external loading, respectively, for each DoF. Often, the steady-state response due to harmonic excitation, $\mathbf{f}(t) = \hat{\mathbf{f}}e^{\mathrm{i}\omega t}$, is of interest. As mentioned in Section 3.2, this steady-state response is solved by assuming a harmonic response with the same frequency, $\mathbf{u}(t) = \hat{\mathbf{u}}e^{\mathrm{i}\omega t}$, resulting in

$$(-\omega^2\mathbf{M} + \mathrm{i}\omega\mathbf{C} + \mathbf{K})\hat{\mathbf{u}} = \mathbf{D}(\omega)\hat{\mathbf{u}} = \hat{\mathbf{f}}. \tag{4.2}$$

In Section 4.1.2 below, the standard FE equations for a 3D linear elastic continuum are presented. These equations are also used in Sections 4.1.3–4.1.4 where FE formulations are presented for a moving frame of reference, and for so called 2.5D FEM, respectively. Although presented here only for solid continuum elements, the concepts presented in Sections 4.1.3–4.1.4 apply analogously also to structural elements such as beam and shell elements, whose derivations in the fixed frame of reference can be found in standard textbooks on FEM, e.g. [43]. Section 4.1.5 contains a brief description of perfectly matched layers (PMLs), that are used for artificially attenuating waves at the truncated ends of a FE model.

4.1.2 Finite element equations for 3D elasticity

The Cauchy equation of motion, governing the dynamic equilibrium of a continuum, was presented in Section 3.1 and is repeated here for clarity,

$$\frac{\partial \sigma_{ij}}{\partial x_j} + b_i = \rho \frac{\partial^2 u_i}{\partial t^2}. \tag{4.3}$$

Defining the matrix differential operator $\tilde{\boldsymbol{\nabla}}$, the stress vector $\boldsymbol{\sigma}$, the body force vector $\mathbf{b}$ and the displacement vector $\mathbf{u}$ as

$$\tilde{\boldsymbol{\nabla}}^{\mathrm{T}} = \begin{bmatrix} \frac{\partial}{\partial x_1} & 0 & 0 & \frac{\partial}{\partial x_2} & \frac{\partial}{\partial x_3} & 0 \\ 0 & \frac{\partial}{\partial x_2} & 0 & \frac{\partial}{\partial x_1} & 0 & \frac{\partial}{\partial x_3} \\ 0 & 0 & \frac{\partial}{\partial x_3} & 0 & \frac{\partial}{\partial x_1} & \frac{\partial}{\partial x_2} \end{bmatrix}, \tag{4.4}$$

$$\boldsymbol{\sigma}^{\mathrm{T}} = \begin{bmatrix} \sigma_{11} & \sigma_{22} & \sigma_{33} & \sigma_{12} & \sigma_{13} & \sigma_{23} \end{bmatrix}, \tag{4.5}$$

$$\mathbf{b}^{\mathrm{T}} = \begin{bmatrix} b_1 & b_2 & b_3 \end{bmatrix}, \tag{4.6}$$

$$\mathbf{u}^{\mathrm{T}} = \begin{bmatrix} u_1 & u_2 & u_3 \end{bmatrix}, \tag{4.7}$$

Eq. (4.3) is written as

$$\tilde{\boldsymbol{\nabla}}^{\mathrm{T}}\boldsymbol{\sigma} + \mathbf{b} = \rho\frac{\partial^2\mathbf{u}}{\partial t^2}. \tag{4.8}$$

The weak form is obtained by multiplying Eq. (4.8) by an arbitrary weight function vector $\mathbf{g} = \mathbf{g}(x_1, x_2, x_3)$ and integrating it over the region [43]. The resulting weak form, after partial integration of the first term, becomes

$$\int_V (\tilde{\boldsymbol{\nabla}}\mathbf{g})^{\mathrm{T}}\boldsymbol{\sigma}\,\mathrm{d}V + \rho\int_V \mathbf{g}^{\mathrm{T}}\frac{\partial^2\mathbf{u}}{\partial t^2}\,\mathrm{d}V = \int_S \mathbf{g}^{\mathrm{T}}\mathbf{t}\,\mathrm{d}S + \int_V \mathbf{g}^{\mathrm{T}}\mathbf{b}\,\mathrm{d}V, \tag{4.9}$$

where $\mathbf{t}$ is the traction vector.

To obtain the FE formulation, the displacements $\mathbf{u}(x_1, x_2, x_3, t)$ are approximated using the nodal values $\mathbf{a}(t)$ and the shape functions $\mathbf{N}(x_1, x_2, x_3)$ as $\mathbf{u} = \mathbf{N}\mathbf{a}$. The shape function matrix $\mathbf{N}$ is written as

$$\mathbf{N}(x_1, x_2, x_3) = \begin{bmatrix} N_1 & 0 & 0 & N_2 & 0 & 0 & \dots & N_n & 0 & 0 \\ 0 & N_1 & 0 & 0 & N_2 & 0 & \dots & 0 & N_n & 0 \\ 0 & 0 & N_1 & 0 & 0 & N_2 & \dots & 0 & 0 & N_n \end{bmatrix}, \tag{4.10}$$

where n is the number of nodes and $N_i = N_i(x_1, x_2, x_3)$. Further, the stress vector is expressed as $\boldsymbol{\sigma} = \mathbf{D}\boldsymbol{\epsilon} = \mathbf{D}\tilde{\boldsymbol{\nabla}}\mathbf{u} = \mathbf{D}\tilde{\boldsymbol{\nabla}}\mathbf{N}\mathbf{a}$. Here, $\mathbf{D}$ is the constitutive matrix for isotropic elasticity,

$$\mathbf{D} = \frac{E}{(1+v)(1-2v)}\begin{bmatrix} 1-v & v & v & 0 & 0 & 0 \\ v & 1-v & v & 0 & 0 & 0 \\ v & v & 1-v & 0 & 0 & 0 \\ 0 & 0 & 0 & \frac{1}{2}(1-2v) & 0 & 0 \\ 0 & 0 & 0 & 0 & \frac{1}{2}(1-2v) & 0 \\ 0 & 0 & 0 & 0 & 0 & \frac{1}{2}(1-2v) \end{bmatrix}. \tag{4.11}$$

Adopting the Galerkin method, the weight function $\mathbf{g}(x_1, x_2, x_3)$ is approximated using the same shape functions as for the displacement field, i.e. $\mathbf{g} = \mathbf{N}\mathbf{c}$. Here, $\mathbf{c}$ is an arbitrary vector. Inserting these approximations for $\mathbf{u}$ and $\mathbf{g}$ into Eq. (4.9) and noting that $\mathbf{c}$ is arbitrary, the mass and stiffness matrices and the load vector, are identified as

$$\begin{aligned} \mathbf{K} &= \int_V (\tilde{\boldsymbol{\nabla}}\mathbf{N})^{\mathrm{T}}\mathbf{D}(\tilde{\boldsymbol{\nabla}}\mathbf{N})\,\mathrm{d}V, \\ \mathbf{M} &= \rho\int_V \mathbf{N}^{\mathrm{T}}\mathbf{N}\,\mathrm{d}V, \\ \mathbf{f}_{\mathrm{l}} &= \int_S \mathbf{N}^{\mathrm{T}}\mathbf{t}\,\mathrm{d}S + \int_V \mathbf{N}^{\mathrm{T}}\mathbf{b}\,\mathrm{d}V. \end{aligned} \tag{4.12}$$

Although the expressions of the matrices in Eqs. (4.12) are for the entire computational domain V with the boundary surface S, they are equally valid, and generally evaluated, for each element separately. This is done by exchanging the integration limits from those of the entire domain (V and S) to those of the individual element (V^{e} and S^{e}) and further by changing $\mathbf{N}$, describing

the shape functions of all the elements, to $\mathbf{N}^{\mathrm{e}}$, describing the shape functions solely for the individual element. The so obtained element matrices ($\mathbf{K}^{\mathrm{e}}$, $\mathbf{M}^{\mathrm{e}}$, $\mathbf{f}_{\mathrm{l}}^{\mathrm{e}}$) are then assembled into their position of the respective global matrices ($\mathbf{K}$, $\mathbf{M}$, $\mathbf{f}_{\mathrm{l}}$), determined by the global numbering of the element DoFs.

4.1.3 Formulation in a moving frame of reference

When analyzing moving loads, such as a train moving along a railway track, a traditional 3D FE approach can lead to a very large system of equations. Because the load is moving, it will eventually leave the computational domain. Hence, it may be necessary to use a very large model. If the geometry and the material properties are invariant in the direction of the moving load, a computationally more efficient model may be obtained, by formulating the governing equations in a reference frame that follows the moving load at a fixed velocity. In such a formulation, the moving load remains fixed in the same position of the model, enabling the use of a smaller computational domain. Furthermore, the problem can be analyzed using frequency-domain methods instead of time-stepping procedures, which may be beneficial both in terms of computational cost and understanding of physical phenomena.

Here, the load is assumed to move at a fixed speed v along the positive x_1-axis. A coordinate transformation is introduced as

$$(\tilde{x}_1, \tilde{x}_2, \tilde{x}_3) = (x_1 - vt, x_2, x_3), \tag{4.13}$$

where $\tilde{x}_1, \tilde{x}_2, \tilde{x}_3$ denotes the coordinates in the moving frame of reference. Partial derivatives in the two reference frames are related as [42]

$$\frac{\partial}{\partial x_1} = \frac{\partial}{\partial \tilde{x}_1}, \qquad \frac{\partial}{\partial t}\Big|_{x_1} = \frac{\partial}{\partial t}\Big|_{\tilde{x}_1} - v\frac{\partial}{\partial \tilde{x}_1}. \tag{4.14}$$

Applying this coordinate transformation to the Cauchy equation of motion, Eq. (4.3), yields

$$\frac{\partial \tilde{\sigma}_{ij}}{\partial \tilde{x}_j} + \tilde{b}_i = \rho\Big(\frac{\partial^2 \tilde{u}_i}{\partial t^2} - 2v\frac{\partial^2 \tilde{u}_i}{\partial t \partial \tilde{x}_1} + v^2\frac{\partial^2 \tilde{u}_i}{\partial^2 \tilde{x}_1}\Big), \tag{4.15}$$

where $\tilde{}$ denotes that a variable is expressed in the moving frame of reference. With a notation analogous to Eq. (4.8), this equation can be written as

$$\tilde{\boldsymbol{\nabla}}^{\mathrm{T}}\tilde{\boldsymbol{\sigma}} + \tilde{\mathbf{b}} = \rho\Big(\frac{\partial^2 \tilde{\mathbf{u}}}{\partial t^2} - 2v\frac{\partial^2 \tilde{\mathbf{u}}}{\partial t \partial \tilde{x}_1} + v^2\frac{\partial^2 \tilde{\mathbf{u}}}{\partial^2 \tilde{x}_1}\Big). \tag{4.16}$$

Now the ordinary procedure is followed to reach the FE formulation. The weak form is obtained by multiplying with an arbitrary weight function $\mathbf{g} = \mathbf{g}(\tilde{x}_1, \tilde{x}_2, \tilde{x}_3)$ and integrating

over the region, resulting in

$$\begin{aligned}\int_V (\tilde{\boldsymbol{\nabla}}\mathbf{g})^{\mathrm{T}}\tilde{\boldsymbol{\sigma}}\,\mathrm{d}V \;&+\rho\int_V \mathbf{g}^{\mathrm{T}}\frac{\partial^2\tilde{\mathbf{u}}}{\partial t^2}\,\mathrm{d}V \;-2\rho\, v\int_V \mathbf{g}^{\mathrm{T}}\frac{\partial^2\tilde{\mathbf{u}}}{\partial t\partial\tilde{x}_1}\,\mathrm{d}V + \\ \rho\, v^2\int_S \mathbf{g}^{\mathrm{T}}\frac{\partial\tilde{\mathbf{u}}}{\partial\tilde{x}_1}\,n_x\,\mathrm{d}S \;&-\rho\, v^2\int_V \frac{\partial\tilde{\mathbf{g}}}{\partial\tilde{x}_1}^{\mathrm{T}}\frac{\partial\tilde{\mathbf{u}}}{\partial\tilde{x}_1}\,\mathrm{d}V = \\ \int_S \mathbf{g}^{\mathrm{T}}\tilde{\mathbf{t}}\,\mathrm{d}S &+\int_V \mathbf{g}^{\mathrm{T}}\tilde{\mathbf{b}}\,\mathrm{d}V,\end{aligned} \tag{4.17}$$

after partial integration of the first term. The displacements $\tilde{\mathbf{u}}(\tilde{x}_1,\tilde{x}_2,\tilde{x}_3,t)$ are approximated using the nodal values $\tilde{\mathbf{a}}(t)$ and the shape functions $\mathbf{N}(\tilde{x}_1,\tilde{x}_2,\tilde{x}_3)$ as $\tilde{\mathbf{u}}=\mathbf{N}\tilde{\mathbf{a}}$. It is emphasized that the nodal values now represent displacements in the moving frame of reference. The weight function $\mathbf{g}(\tilde{x}_1,\tilde{x}_2,\tilde{x}_3)$ is approximated using the same shape functions, i.e. $\mathbf{g}=\mathbf{N}\tilde{\mathbf{c}}$, where $\tilde{\mathbf{c}}$ is an arbitrary vector. Inserting these approximations into Eq. (4.17) yields the mass, damping and stiffness matrices, as well as the load vector, as

$$\begin{aligned}\mathbf{K} &= \int_V (\tilde{\boldsymbol{\nabla}}\mathbf{N})^{\mathrm{T}}\mathbf{D}(\tilde{\boldsymbol{\nabla}}\mathbf{N})\,\mathrm{d}V \;-\rho v^2\int_V \frac{\partial\mathbf{N}}{\partial\tilde{x}_1}^{\mathrm{T}}\frac{\partial\mathbf{N}}{\partial\tilde{x}_1}\,\mathrm{d}V+\rho v^2\int_S \mathbf{N}^{\mathrm{T}}\frac{\partial\mathbf{N}}{\partial\tilde{x}_1}n_x\,\mathrm{d}S,\\ \mathbf{C} &= -2\rho v\int_V \mathbf{N}^{\mathrm{T}}\frac{\partial\mathbf{N}}{\partial\tilde{x}_1}\,\mathrm{d}V,\\ \mathbf{M} &= \rho\int_V \mathbf{N}^{\mathrm{T}}\mathbf{N}\,\mathrm{d}V,\\ \mathbf{f}_{\mathrm{l}} &= \int_S \mathbf{N}^{\mathrm{T}}\tilde{\mathbf{t}}\,\mathrm{d}S+\int_V \mathbf{N}^{\mathrm{T}}\tilde{\mathbf{b}}\,\mathrm{d}V.\end{aligned} \tag{4.18}$$

Comparing Eqs. (4.18) with Eqs. (4.12) it is seen that due to the coordinate transformation, some velocity dependent terms have arised in the stiffness matrix and the damping matrix. These terms are called convective terms. It is also emphasized that if the load speed is set to $v=0$, the expressions in Eqs. (4.18) are identical to Eqs. (4.12). As pointed out in [42], convection may lead to unstable numerical solutions in time domain analyses if the standard Galerkin approach is used, and there are different ways to stabilize the solution. However, in the present work the formulation above is used merely for frequency domain analyses, see Chapter 5 and the appended papers.

4.1.4 FE formulation in 2.5D

When the problem geometry is invariant in one direction, an efficient solution method can be established by Fourier transforming the governing equations with respect to the invariant coordinate axis [30, 31, 44]. This is often called 2.5D FEM or wavenumber FEM.

The weak form for 3D elasticity was established in Eq. 4.9 and is repeated here for convenience.

$$\int_V (\tilde{\boldsymbol{\nabla}}\mathbf{g})^{\mathrm{T}}\boldsymbol{\sigma}\,\mathrm{d}V+\rho\int_V \mathbf{g}^{\mathrm{T}}\frac{\partial^2\mathbf{u}}{\partial t^2}\,\mathrm{d}V=\int_S \mathbf{g}^{\mathrm{T}}\mathbf{t}\,\mathrm{d}S+\int_V \mathbf{g}^{\mathrm{T}}\mathbf{b}\,\mathrm{d}V. \tag{4.19}$$

The volume V is now assumed to be limited in the (x_2, x_3) directions by the area A, and to have infinite length in the x_1-direction. This means that the equation can be written as

$$\begin{aligned}\int_{\infty}^{\infty}\int_{A}(\tilde{\boldsymbol{\nabla}}\mathbf{g})^{\mathrm{T}}\boldsymbol{\sigma}\,\mathrm{d}A\,\mathrm{d}x_1+\int_{\infty}^{\infty}\int_{A}\mathbf{g}^{\mathrm{T}}\frac{\partial^2\mathbf{u}}{\partial t^2}\,\mathrm{d}A\,\mathrm{d}x_1-\\ \int_{\infty}^{\infty}\int_{A}\mathbf{g}^{\mathrm{T}}\mathbf{b}\,\mathrm{d}A\,\mathrm{d}x_1-\int_{\infty}^{\infty}\oint_{\Gamma_A}\mathbf{g}^{\mathrm{T}}\mathbf{t}\,\mathrm{d}\Gamma_A\,\mathrm{d}x_1=0,\end{aligned} \tag{4.20}$$

where Γ_A denotes the circumference of the area A. Now, the FE mesh is defined on the surface A in the (x_2, x_3)-plane. The shape function matrix is written as

$$\mathbf{N}(x_2,x_3)=\begin{bmatrix}N_1 & 0 & 0 & N_2 & 0 & 0 & \dots & N_n & 0 & 0\\ 0 & N_1 & 0 & 0 & N_2 & 0 & \dots & 0 & N_n & 0\\ 0 & 0 & N_1 & 0 & 0 & N_2 & \dots & 0 & 0 & N_n\end{bmatrix}, \tag{4.21}$$

where n is the number of nodes and $N_i = N_i(x_2, x_3)$. Further, the displacement vector $\mathbf{u}$,

$$\mathbf{u}(x_1,x_2,x_3)=\begin{bmatrix}u_1(x_1,x_2,x_3) & u_2(x_1,x_2,x_3) & u_3(x_1,x_2,x_3)\end{bmatrix}^{\mathrm{T}}, \tag{4.22}$$

is now approximated using the shape functions and the nodal displacement vector as $\mathbf{u}(x_1, x_2, x_3) = \mathbf{N}(x_2, x_3)\mathbf{a}(x_1)$, where

$$\mathbf{a}(x_1)=\begin{bmatrix}a_{1_{x_1}}(x_1) & a_{1_{x_2}}(x_1) & a_{1_{x_3}}(x_1) & a_{2_{x_1}}(x_1) & \dots & a_{n_{x_3}}(x_1)\end{bmatrix}^{\mathrm{T}}. \tag{4.23}$$

With the Galerkin approach, the weight function vector $\mathbf{g}$ is also approximated using the shape function matrix and an arbitrary nodal displacement vector as $\mathbf{g}(x_1, x_2, x_3) = \mathbf{N}(x_2, x_3)\mathbf{c}(x_1)$. As usual, the stress vector is expressed as $\boldsymbol{\sigma} = \mathbf{D}\boldsymbol{\epsilon} = \mathbf{D}\tilde{\boldsymbol{\nabla}}\mathbf{u} = \mathbf{D}\tilde{\boldsymbol{\nabla}}\mathbf{N}\mathbf{a}$ where $\mathbf{D}$ is the constitutive matrix for isotropic elasticity defined in Eq. (4.11). With the matrix differential

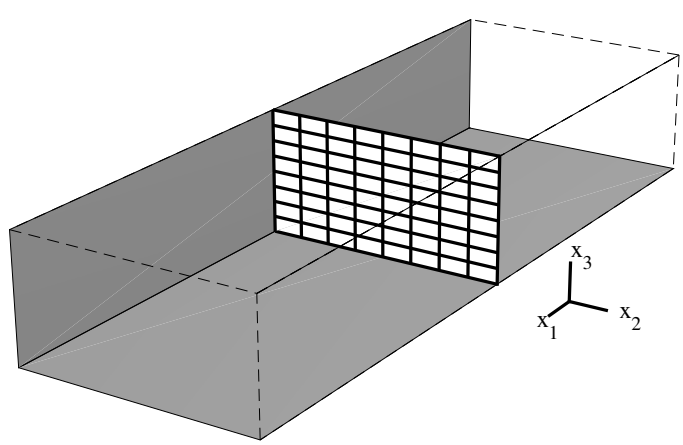

Figure 4.1: A longitudinally invariant structure with a 2D mesh defined in the (x_2, x_3)-plane.

operator $\tilde{\boldsymbol{\nabla}}$ defined by Eq. (4.4),

$$\begin{aligned}\tilde{\boldsymbol{\nabla}}\mathbf{u} &= \tilde{\boldsymbol{\nabla}}(\mathbf{N}\mathbf{a}) = \mathbf{L}_1\mathbf{N}(x_2,x_3)\mathbf{a}(x_1) + \mathbf{L}_2\mathbf{N}(x_2,x_3)\frac{\partial \mathbf{a}(x_1)}{\partial x_1} = \mathbf{B}_1\mathbf{a}(x_1) + \mathbf{B}_2\frac{\partial \mathbf{a}(x_1)}{\partial x_1},\\ \tilde{\boldsymbol{\nabla}}\mathbf{g} &= \tilde{\boldsymbol{\nabla}}(\mathbf{N}\mathbf{c}) = \mathbf{L}_1\mathbf{N}(x_2,x_3)\mathbf{a}(x_1) + \mathbf{L}_2\mathbf{N}(x_2,x_3)\frac{\partial \mathbf{c}(x_1)}{\partial x_1} = \mathbf{B}_1\mathbf{a}(x_1) + \mathbf{B}_2\frac{\partial \mathbf{c}(x_1)}{\partial x_1},\end{aligned} \tag{4.24}$$

where

$$\mathbf{L}_1^T = \begin{bmatrix} 0 & 0 & 0 & \frac{\partial}{\partial x_2} & \frac{\partial}{\partial x_3} & 0 \\ 0 & \frac{\partial}{\partial x_2} & 0 & 0 & 0 & \frac{\partial}{\partial x_3} \\ 0 & 0 & \frac{\partial}{\partial x_3} & 0 & 0 & \frac{\partial}{\partial x_2} \end{bmatrix}, \tag{4.25}$$

and

$$\mathbf{L}_2^T = \begin{bmatrix} 1 & 0 & 0 & 0 & 0 & 0 \\ 0 & 0 & 0 & 1 & 0 & 0 \\ 0 & 0 & 0 & 0 & 1 & 0 \end{bmatrix}. \tag{4.26}$$

Equation 4.20 can now be written as

$$\begin{aligned}&\int_\infty^\infty \int_A \Big(\mathbf{B}_1\mathbf{c} + \mathbf{B}_2\frac{\partial \mathbf{c}}{\partial x_1}\Big)^{\mathrm{T}}\mathbf{D}\Big(\mathbf{B}_1\mathbf{a} + \mathbf{B}_2\frac{\partial \mathbf{a}}{\partial x_1}\Big)\,\mathrm{d}A\,\mathrm{d}x_1 + \\ &\quad\int_\infty^\infty \int_A \Big(\mathbf{N}\mathbf{c}\Big)^{\mathrm{T}}\rho\Big(\mathbf{N}\frac{\partial^2 \mathbf{a}}{\partial t^2}\Big)\,\mathrm{d}A\,\mathrm{d}x_1 - \int_\infty^\infty \int_A \Big(\mathbf{N}\mathbf{c}\Big)^{\mathrm{T}}\mathbf{b}\,\mathrm{d}A\,\mathrm{d}x_1 - \\ &\quad\int_\infty^\infty \oint_{\Gamma_A} \Big(\mathbf{N}\mathbf{c}\Big)^{\mathrm{T}}\mathbf{t}\,\mathrm{d}\Gamma_A\,\mathrm{d}x_1 = 0,\end{aligned} \tag{4.27}$$

which, by noting that $\mathbf{a}(x_1)$ and $\mathbf{c}(x_1)$ are independent of (x_2, x_3) and can therefore be placed outside the inner integral, can be written as

$$\begin{aligned}&\int_\infty^\infty \mathbf{c}^{\mathrm{T}} \int_A \mathbf{B}_1^{\mathrm{T}}\mathbf{D}\mathbf{B}_1\,\mathrm{d}A\,\mathbf{a}\,\mathrm{d}x_1 + \int_\infty^\infty \mathbf{c}^{\mathrm{T}} \int_A \mathbf{B}_1^{\mathrm{T}}\mathbf{D}\mathbf{B}_2\,\mathrm{d}A\,\frac{\partial \mathbf{a}}{\partial x_1}\,\mathrm{d}x_1 + \\ &\quad\int_\infty^\infty \frac{\partial \mathbf{c}}{\partial x_1}^{\mathrm{T}} \int_A \mathbf{B}_2^{\mathrm{T}}\mathbf{D}\mathbf{B}_1\,\mathrm{d}A\,\mathbf{a}\,\mathrm{d}x_1 + \int_\infty^\infty \frac{\partial \mathbf{c}}{\partial x_1}^{\mathrm{T}} \int_A \mathbf{B}_2^{\mathrm{T}}\mathbf{D}\mathbf{B}_2\,\mathrm{d}A\,\frac{\partial \mathbf{a}}{\partial x_1}\,\mathrm{d}x_1 + \\ &\quad\int_\infty^\infty \mathbf{c}^{\mathrm{T}} \int_A \mathbf{N}^{\mathrm{T}}\rho\mathbf{N}\,\mathrm{d}A\,\frac{\partial^2 \mathbf{a}}{\partial t^2}\,\mathrm{d}x_1 - \int_\infty^\infty \mathbf{c}^{\mathrm{T}} \int_A \mathbf{N}^{\mathrm{T}}\mathbf{b}\,\mathrm{d}A\,\mathrm{d}x_1 - \\ &\quad\int_\infty^\infty \mathbf{c}^{\mathrm{T}} \oint_{\Gamma_A} \mathbf{N}^{\mathrm{T}}\mathbf{t}\,\mathrm{d}\Gamma_A\,\mathrm{d}x_1 = 0.\end{aligned} \tag{4.28}$$

Now, a Fourier transform from the x_1-coordinate to the wavenumber k_1 is performed, and

the following notation is used

$$\begin{aligned}
\hat{\mathbf{a}}(k_1) &= \int_{\infty}^{\infty} \mathbf{a}(x_1) e^{-\mathrm{i}k_1 x_1}\,\mathrm{d}x_1,\\
\hat{\mathbf{c}}(k_1) &= \int_{\infty}^{\infty} \mathbf{c}(x_1) e^{-\mathrm{i}k_1 x_1}\,\mathrm{d}x_1,\\
\hat{\mathbf{b}}(k_1, x_2, x_3) &= \int_{\infty}^{\infty} \mathbf{b}(x_1, x_2, x_3) e^{-\mathrm{i}k_1 x_1}\,\mathrm{d}x_1,\\
\hat{\mathbf{t}}(k_1, x_2, x_3) &= \int_{\infty}^{\infty} \mathbf{t}(x_1, x_2, x_3) e^{-\mathrm{i}k_1 x_1}\,\mathrm{d}x_1.
\end{aligned} \tag{4.29}$$

The derivatives of $\mathbf{a}$ and $\mathbf{c}$ with respect to x_1, become

$$\begin{aligned}
\mathscr{F}\Big(\frac{\partial \mathbf{a}(x_1)}{\partial x_1}\Big) &= \mathrm{i}k_1 \hat{\mathbf{a}}(k_1),\\
\mathscr{F}\Big(\frac{\partial \mathbf{c}(x_1)}{\partial x_1}\Big) &= \mathrm{i}k_1 \hat{\mathbf{c}}(k_1).
\end{aligned} \tag{4.30}$$

To transform Eq. (4.27), from spatial x_1- to wavenumber k_1-domain, Parseval's formula is used:

$$\int_{\infty}^{\infty} \overline{g(x_1)} m(x_1)\,\mathrm{d}x_1 = \int_{\infty}^{\infty} \overline{\hat{g}(k_1)} \hat{m}(k_1)\,\mathrm{d}\frac{k_1}{2\pi}. \tag{4.31}$$

Equation (4.31) is now applied on Eq. (4.27), yielding

$$\begin{aligned}
&\int_{\infty}^{\infty} \overline{\hat{\mathbf{c}}^{\mathrm{T}}} \int_A \mathbf{B}_1^{\mathrm{T}} \mathbf{D} \mathbf{B}_1\,\mathrm{d}A\,\hat{\mathbf{a}}\,\mathrm{d}\frac{k_1}{2\pi} + \int_{\infty}^{\infty} \mathrm{i}k_1 \overline{\hat{\mathbf{c}}^{\mathrm{T}}} \int_A \mathbf{B}_1^{\mathrm{T}} \mathbf{D} \mathbf{B}_2\,\mathrm{d}A\,\hat{\mathbf{a}}\,\mathrm{d}\frac{k_1}{2\pi} +\\
&\quad \int_{\infty}^{\infty} -\mathrm{i}k_1 \overline{\hat{\mathbf{c}}^{\mathrm{T}}} \int_A \mathbf{B}_2^{\mathrm{T}} \mathbf{D} \mathbf{B}_1\,\mathrm{d}A\,\hat{\mathbf{a}}\,\mathrm{d}\frac{k_1}{2\pi} + \int_{\infty}^{\infty} k_1^2 \overline{\hat{\mathbf{c}}^{\mathrm{T}}} \int_A \mathbf{B}_2^{\mathrm{T}} \mathbf{D} \mathbf{B}_2\,\mathrm{d}A\,\hat{\mathbf{a}}\,\mathrm{d}\frac{k_1}{2\pi} +\\
&\quad \int_{\infty}^{\infty} \overline{\hat{\mathbf{c}}^{\mathrm{T}}} \int_A \mathbf{N}^{\mathrm{T}} \rho \mathbf{N}\,\mathrm{d}A\,\frac{\partial^2 \hat{\mathbf{a}}}{\partial t^2}\,\mathrm{d}\frac{k_1}{2\pi} - \int_{\infty}^{\infty} \overline{\hat{\mathbf{c}}^{\mathrm{T}}} \int_A \mathbf{N}^{\mathrm{T}} \hat{\mathbf{b}}\,\mathrm{d}A\,\mathrm{d}\frac{k_1}{2\pi} -\\
&\quad \int_{\infty}^{\infty} \overline{\hat{\mathbf{c}}^{\mathrm{T}}} \oint_{\Gamma_A} \mathbf{N}^{\mathrm{T}} \hat{\mathbf{t}}\,\mathrm{d}\Gamma_A\,\mathrm{d}\frac{k_1}{2\pi} = 0.
\end{aligned} \tag{4.32}$$

Since $\hat{\mathbf{c}}(k_1)$ is arbitrary, it can be concluded that the following equation must apply for each wavenumber k_1,

$$\mathbf{M}\ddot{\hat{\mathbf{a}}}(k_1) + \Big(\mathbf{K}_0 + \mathrm{i}k_1 \mathbf{K}_1 + k_1^2 \mathbf{K}_2\Big)\hat{\mathbf{a}}(k_1) = \hat{\mathbf{f}}_{\mathrm{l}}(k_1), \tag{4.33}$$

where $\ddot{\hat{\mathbf{a}}}(k_1) = \frac{\partial^2 \hat{\mathbf{a}}(k_1)}{\partial t^2}$ and

$$\begin{aligned}
\mathbf{M} &= \int_A \mathbf{N}^{\mathrm{T}} \rho \mathbf{N} \, \mathrm{d}A, \\
\mathbf{K}_0 &= \int_A \mathbf{B}_1^{\mathrm{T}} \mathbf{D} \mathbf{B}_1 \, \mathrm{d}A, \\
\mathbf{K}_1 &= \int_A \mathbf{B}_1^{\mathrm{T}} \mathbf{D} \mathbf{B}_2 \, \mathrm{d}A - \int_A \mathbf{B}_2^{\mathrm{T}} \mathbf{D} \mathbf{B}_1 \, \mathrm{d}A, \\
\mathbf{K}_2 &= \int_A \mathbf{B}_2^{\mathrm{T}} \mathbf{D} \mathbf{B}_2 \, \mathrm{d}A, \\
\hat{\mathbf{f}}_{\mathrm{l}} &= \int_A \mathbf{N}^{\mathrm{T}} \hat{\mathbf{b}} \, \mathrm{d}A + \oint_{\Gamma_A} \mathbf{N}^{\mathrm{T}} \hat{\mathbf{t}} \, \mathrm{d}\Gamma_A \, .
\end{aligned} \tag{4.34}$$

The terms $\mathbf{M}$, $\mathbf{K}_0$, $\mathbf{K}_1$ and $\mathbf{K}_2$ are independent of the wavenumber k_1 and only need to be evaluated once. The load vector $\hat{\mathbf{f}}_{\mathrm{l}}$ is in general, however, wavenumber dependent.

For a harmonic load $\hat{\mathbf{f}}_{\mathrm{l}}(k_1, t) = \check{\mathbf{f}}_{\mathrm{l}}(k_1) e^{\mathrm{i}\omega t}$, the response is also harmonic, $\hat{\mathbf{a}}(k_1, t) = \check{\mathbf{a}}(k_1) e^{\mathrm{i}\omega t}$ leading to,

$$\big(-\omega^2 \mathbf{M} + \mathbf{K}_0 + \mathrm{i} k_1 \mathbf{K}_1 + k_1^2 \mathbf{K}_2 \big) \check{\mathbf{a}}(k_1) = \check{\mathbf{f}}_{\mathrm{l}}(k_1). \tag{4.35}$$

The system of equations given by Eq. (4.35) is solved for a set of discrete values of the wavenumber k_1, and the nodal displacements in spatial domain $\mathbf{a}(x_1)$ are then obtained by a discrete inverse Fourier transform of $\check{\mathbf{a}}(k_1)$. When solved for N uniformly spaced wavenumbers ranging from $k_1 = -(\frac{N}{2} - 1)\Delta k_1$ to $k_1 = (\frac{N}{2})\Delta k_1$, the displacements $\mathbf{a}(x_1)$ are obtained for N uniformly spaced points on the x_1-axis, spanning the length $2\pi / \Delta k_1$.

Formulation in a moving frame of reference

Contrary to the full 3D case discussed in Section 4.1.3, no additional integrals are introduced in the FE matrices in the case of 2.5D FE, when the fixed frame of reference is replaced by one moving at velocity v along the x_1-axis. In wavenumber domain, this change of reference frames becomes particularly simple. Actually, the response is obtained in the moving frame of reference following the load at velocity v, by replacing ω in Eq. (4.35) by $\tilde{\omega} = \omega - k_1 v$. This is shown in Section 4.2.3 for the semi-analytical ground model and, by analogy, applies also to the case of FE in the wavenumber domain.

4.1.5 Perfectly matched layers

Special attention needs to be given to the fictitious boundaries of a truncated FE model in order to avoid spurious reflections of elastic waves. One efficient technique is to truncate the FE model by the use of Perfectly Matched Layers (PMLs) that absorb propagating waves with any angle of incidence. The idea behind PMLs is the introduction of a so called stretched

coordinate. Consider an elastic domain extending from $s = 0$ to $s = s_0$, and a PML region extending from $s = s_0$ to $s = s_t$, see Figure 4.2.

The stretched coordinate is defined as [25, 44]

$$\tilde{s} = \int_0^s \lambda_s(s)\mathrm{d}s = s_0 + \int_{s_0}^{s_t} \lambda_s(s)\mathrm{d}s, \tag{4.36}$$

where $\lambda_s(s)$ is a complex valued stretch function. Partial derivatives with respect to $\tilde{s}$ are written as

$$\frac{\partial}{\partial \tilde{s}} = \frac{1}{\lambda_s(s)}\frac{\partial}{\partial s}. \tag{4.37}$$

Here, a formulation for PMLs in a 2.5D context [44] is considered. Stretching is applied to the x_2- and x_3-coordinates by introducing the partial derivatives of the stretched coordinates $\tilde{x_2}$ and $\tilde{x_3}$ into the equilibrium equation; see Eq. (4.8). Disregarding body forces and assuming steady-state response with angular frequency ω, this leads to the modified equilibrium equations

$$\hat{\tilde{\boldsymbol{\nabla}}}^T \boldsymbol{\sigma} + \omega^2 \rho \mathbf{u} = 0, \tag{4.38}$$

where

$$\hat{\tilde{\boldsymbol{\nabla}}}^T = \begin{bmatrix} \frac{\partial}{\partial x_1} & 0 & 0 & \frac{1}{\lambda_2}\frac{\partial}{\partial x_2} & \frac{1}{\lambda_3}\frac{\partial}{\partial x_3} & 0 \\ 0 & \frac{1}{\lambda_2}\frac{\partial}{\partial x_2} & 0 & \frac{\partial}{\partial x_1} & 0 & \frac{1}{\lambda_3}\frac{\partial}{\partial x_3} \\ 0 & 0 & \frac{1}{\lambda_3}\frac{\partial}{\partial x_3} & 0 & \frac{\partial}{\partial x_1} & \frac{1}{\lambda_2}\frac{\partial}{\partial x_2} \end{bmatrix}. \tag{4.39}$$

It is shown in [44] that by applying a Galerkin procedure and FE discretization, Eq. (4.35)

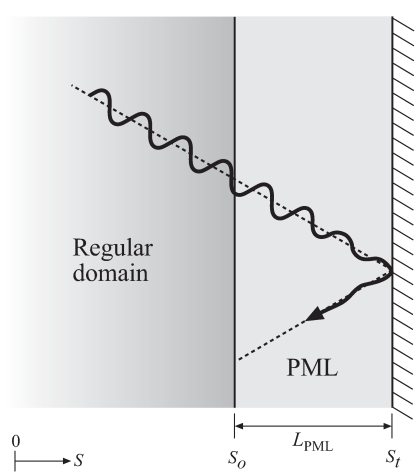

Figure 4.2: An incident wave being attenuated inside the PML.

applies with the following FE matrices for the PML region:

$$\begin{aligned}
\mathbf{M} &= \int_A \lambda_2\lambda_3 \mathbf{N}^{\mathrm{T}} \rho \mathbf{N}\, \mathrm{d}A, \\
\mathbf{K}_0 &= \int_A \lambda_2\lambda_3 \mathbf{B}_1^{\mathrm{T}} \mathbf{D} \mathbf{B}_1\, \mathrm{d}A, \\
\mathbf{K}_1 &= \int_A \lambda_2\lambda_3 \Big(\mathbf{B}_1^{\mathrm{T}} \mathbf{D} \mathbf{B}_2 - \mathbf{B}_2^{\mathrm{T}} \mathbf{D} \mathbf{B}_1 \Big)\, \mathrm{d}A, \\
\mathbf{K}_2 &= \int_A \lambda_2\lambda_3 \mathbf{B}_2^{\mathrm{T}} \mathbf{D} \mathbf{B}_2\, \mathrm{d}A, \\
\hat{\mathbf{f}}_{\mathrm{l}} &= \oint_{\Gamma_A} \lambda_2\lambda_3 \mathbf{N}^{\mathrm{T}} \hat{\mathbf{t}}\, \mathrm{d}\Gamma_A \,.
\end{aligned} \tag{4.40}$$

where $\mathbf{B}_1 = \mathbf{L}_1\mathbf{N}$ and $\mathbf{B}_2 = \mathbf{L}_2\mathbf{N}$ with

$$\mathbf{L}_1^{\mathrm{T}} = \begin{bmatrix} 0 & 0 & 0 & \frac{1}{\lambda_2}\frac{\partial}{\partial x_2} & \frac{1}{\lambda_3}\frac{\partial}{\partial x_3} & 0 \\ 0 & \frac{1}{\lambda_2}\frac{\partial}{\partial x_2} & 0 & 0 & 0 & \frac{1}{\lambda_3}\frac{\partial}{\partial x_3} \\ 0 & 0 & \frac{1}{\lambda_3}\frac{\partial}{\partial x_3} & 0 & 0 & \frac{1}{\lambda_2}\frac{\partial}{\partial x_2} \end{bmatrix}, \tag{4.41}$$

and

$$\mathbf{L}_2^{\mathrm{T}} = \begin{bmatrix} 1 & 0 & 0 & 0 & 0 & 0 \\ 0 & 0 & 0 & 1 & 0 & 0 \\ 0 & 0 & 0 & 0 & 1 & 0 \end{bmatrix}. \tag{4.42}$$

The stretching functions may be selected according to [25, 44] as

$$\lambda_j(x_j) = 1 + f_j^{\,e}(x_j) - \mathrm{i}\frac{f_j^{\,p}(x_j)}{a_0}, \tag{4.43}$$

where $a_0 = \omega L_{PML}/c_s$ is a dimensionless frequency, with L_{PML} being a characteristic length chosen as the thickness of the PML and c_s is the shear wave velocity in the medium. The functions $f_j^{\,e}(x_j)$ and $f_j^{\,p}(x_j)$ are attenuation functions, attenuating evanescent (*e*) and propagating (*p*) waves, respectively. For $\lambda_2 = \lambda_3 = 1$, it is seen that the matrices in Eq. (4.40) for the PML region equal those in Eq. (4.34) for the regular domain. This should hold at the interface between the regular domain and the PML to avoid an impedance mismatch, i.e. the attenuation functions $f_j^{\,e}(x_j)$ and $f_j^{\,p}(x_j)$ should equal zero at the interface. It is shown in [44] that using a non-zero attenuation function for the evanescent waves shortens the wavelength of propagating waves inside the PML, necessitating a denser FE mesh.

4.2 THE LAYER TRANSFER MATRIX METHOD

4.2.1 General remarks

Using FEM to analyze wave propagation problems in (semi-)infinite media such as a layered half-space poses a number of potential problems. One issue is that, depending on the problem at hand, often a large computational domain is required. The required number of elements in the computational domain depends on the wavelengths. Typically 6–10 nodes are needed per wavelength to properly resolve a propagating wave. With increasing loading frequency the wavelengths decrease, and hence the number of required elements increases.

However, if visco-elastic properties and a horizontal stratification is assumed, see Figure 4.3, a so called Green's function (a fundamental solution) can be found analytically in frequency–wavenumber domain by the layer transfer matrix (LTM) method. When the solution has been established for a set of wavenumbers, it is brought back to frequency–space domain through a 2D discrete inverse Fourier transform.

The method briefly outlined below, was derived in [35, 36] and is further detailed in [45] and [42].

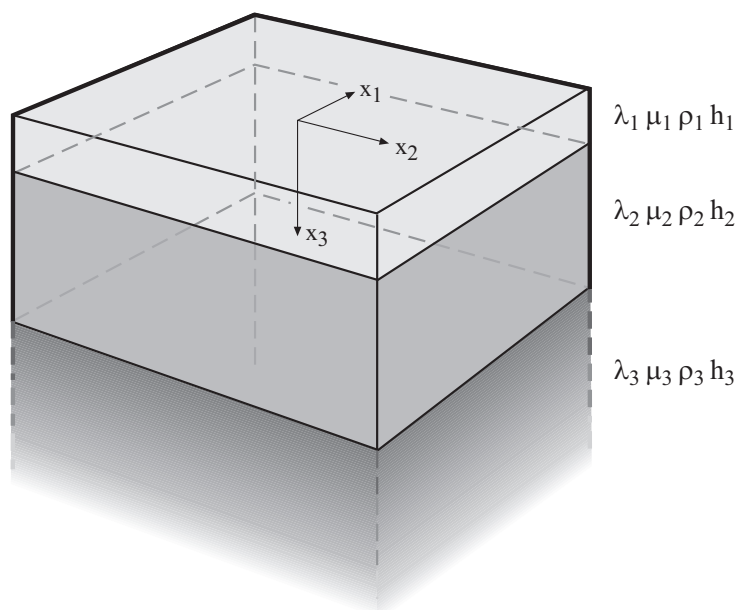

Figure 4.3: Horizontally layered half-space with visco-elastic properties.

4.2.2 Flexibility matrix of a horizontally layered half-space

First, a single soil layer with the Lame's parameters λ and μ and density ρ, is considered. Neglecting body forces, the equilibrium of the soil layer is governed by Navier equations

$$(\lambda+\mu)\frac{\partial^2 u_j}{\partial x_i \partial x_j}+\mu\frac{\partial^2 u_i}{\partial x_j \partial x_j}=\rho\frac{\partial^2 u_i}{\partial t^2}, \tag{4.44}$$

and some boundary conditions on the top and bottom of the layer. Here, $u_i = u_i(x_1, x_2, x_3, t)$ is the displacement in direction *i*.

Fourier transforming the Navier equations with respect to the horizontal coordinates and time, (x_1, x_2, t), i.e.

$$U_i(k_1,k_2,x_3,\omega)=\int_{-\infty}^{\infty}\int_{-\infty}^{\infty}\int_{-\infty}^{\infty} u_i e^{-\mathrm{i}(k_1x_1+k_2x_2+\omega t)}\mathrm{d}x_1\mathrm{d}x_2\mathrm{d}t, \tag{4.45}$$

yields the Navier equations in frequency–wavenumber domain as

$$(\lambda+\mu)\check{\Delta}\mathrm{i}k_1+\mu(\frac{\mathrm{d}^2}{\mathrm{d}x_3^2}-k_1^2-k_2^2)U_1=-\rho\omega^2U_1, \tag{4.46a}$$

$$(\lambda+\mu)\check{\Delta}\mathrm{i}k_2+\mu(\frac{\mathrm{d}^2}{\mathrm{d}x_3^2}-k_1^2-k_2^2)U_2=-\rho\omega^2U_2, \tag{4.46b}$$

$$(\lambda+\mu)\frac{\mathrm{d}\check{\Delta}}{\mathrm{d}x_3}+\mu(\frac{\mathrm{d}^2}{\mathrm{d}x_3^2}-k_1^2-k_2^2)U_3=-\rho\omega^2U_3, \tag{4.46c}$$

where k_1 and k_2 are the wavenumbers in the direction of x_1 and x_2, respectively, and ω is the frequency of vibration. Further, $\check{\Delta}=\check{\Delta}(k_1,k_2,x_3,\omega)$ is the Fourier transform, with respect to the horizontal coordinates and time, of the dilation $\Delta(x_1,x_2,x_3,t)$ defined in Eq. (3.6), i.e.

$$\check{\Delta}(k_1,k_2,x_3,\omega)=\int_{-\infty}^{\infty}\int_{-\infty}^{\infty}\int_{-\infty}^{\infty}\Delta e^{-\mathrm{i}(k_1x_1+k_2x_2+\omega t)}\mathrm{d}x_1\mathrm{d}x_2\mathrm{d}t=\mathrm{i}k_1U_1+\mathrm{i}k_2U_2+\frac{\mathrm{d}U_3}{\mathrm{d}x_3}. \tag{4.47}$$

Equation (4.46a) and Eq. (4.46b) are now multiplied by $\mathrm{i}k_1$ and $\mathrm{i}k_2$ respectively, and Eq (4.46c) is differentiated with respect to x_3. The sum of the three equations lead to the ordinary homogeneous differential equation for the dilation

$$(\frac{\mathrm{d}^2}{\mathrm{d}x_3^2}-k_1^2-k_2^2+\frac{\omega^2}{c_p^2})\check{\Delta}=(\frac{\mathrm{d}^2}{\mathrm{d}x_3^2}-k_1^2-k_2^2+k_p^2)\check{\Delta}=(\frac{\mathrm{d}^2}{\mathrm{d}x_3^2}-\alpha_p^2)\check{\Delta}=0, \tag{4.48}$$

where c_p and k_p is the phase speed and wavenumber, respectively, of the P-wave and the following definitions have been made

$$\alpha_p^2=k_1^2+k_2^2-k_p^2, \tag{4.49a}$$

$$\alpha_s^2=k_1^2+k_2^2-k_s^2. \tag{4.49b}$$

Equation (4.48) has the solution

$$\check{\Delta}(k_1, k_2, x_3, \omega) = a_1 e^{\alpha_p x_3} + a_2 e^{-\alpha_p x_3}, \tag{4.50}$$

where a_1 and a_2 are integration constants. The solution for the dilation is inserted into Eqs. (4.46a-c), leading to three equations for the displacement amplitudes,

$$\frac{\mathrm{d}^2 U_1}{\mathrm{d}x_3^2} - \alpha_s^2 U_1 = -(\frac{\lambda}{\mu} + 1)\mathrm{i}k_1(a_1 e^{\alpha_p x_3} + a_2 e^{-\alpha_p x_3}), \tag{4.51a}$$

$$\frac{\mathrm{d}^2 U_2}{\mathrm{d}x_3^2} - \alpha_s^2 U_2 = -(\frac{\lambda}{\mu} + 1)\mathrm{i}k_2(a_1 e^{\alpha_p x_3} + a_2 e^{-\alpha_p x_3}), \tag{4.51b}$$

$$\frac{\mathrm{d}^2 U_3}{\mathrm{d}x_3^2} - \alpha_s^2 U_3 = -(\frac{\lambda}{\mu} + 1)\alpha_p(a_1 e^{\alpha_p x_3} - a_2 e^{-\alpha_p x_3}). \tag{4.51c}$$

The solutions to Eqs.(4.51) can be written as

$$U_1 = b_1 e^{\alpha_s x_3} + b_2 e^{-\alpha_s x_3} + b_3 e^{\alpha_p x_3} + b_4 e^{-\alpha_p x_3}, \tag{4.52a}$$

$$U_2 = c_1 e^{\alpha_s x_3} + c_2 e^{-\alpha_s x_3} + c_3 e^{\alpha_p x_3} + c_4 e^{-\alpha_p x_3}, \tag{4.52b}$$

$$U_3 = d_1 e^{\alpha_s x_3} + d_2 e^{-\alpha_s x_3} + d_3 e^{\alpha_p x_3} + d_4 e^{-\alpha_p x_3}. \tag{4.52c}$$

It can be shown that only six of the integration constants $(a_1, a_2, b_1, b_2, c_1, c_2)$ are independent [42], and that the remaining constants are

$$\begin{aligned} b_3 &= -\tfrac{\mathrm{i}k_1}{k_p^2}a_1, & b_4 &= -\tfrac{\mathrm{i}k_1}{k_p^2}a_2, & c_3 &= -\tfrac{\mathrm{i}k_2}{k_p^2}a_1, & c_4 &= -\tfrac{\mathrm{i}k_2}{k_p^2}a_2, \\ d_1 &= -\Big(\tfrac{\mathrm{i}k_1}{\alpha_s}b_1 + \tfrac{\mathrm{i}k_2}{\alpha_s}c_1\Big), & d_2 &= \tfrac{\mathrm{i}k_1}{\alpha_s}b_2 + \tfrac{\mathrm{i}k_2}{\alpha_s}c_2, & d_3 &= -\tfrac{\alpha_p}{k_p^2}a_1, & d_4 &= \tfrac{\alpha_p}{k_p^2}a_2. \end{aligned} \tag{4.53}$$

Fourier transforming the stress tensor, $\sigma_{jk}(x_1, x_2, x_3, t)$ defined in Eq. (3.4), with respect to the horizontal coordinates and time yields

$$\check{\sigma}_{jk}(k_1, k_2, x_3, \omega) = \int_{-\infty}^{\infty}\int_{-\infty}^{\infty}\int_{-\infty}^{\infty} \sigma_{jk} e^{-\mathrm{i}(k_1 x_1 + k_2 x_2 + \omega t)} \mathrm{d}x_1 \mathrm{d}x_2 \mathrm{d}t. \tag{4.54}$$

For a known displacement field (U_1, U_2, U_3), the corresponding traction stresses $(\check{\sigma}_{13}, \check{\sigma}_{23}, \check{\sigma}_{33})$ are calculated as

$$\check{\sigma}_{13} = \mu(\frac{\mathrm{d}U_1}{\mathrm{d}x_3} + \mathrm{i}k_1 U_3), \tag{4.55a}$$

$$\check{\sigma}_{23} = \mu(\frac{\mathrm{d}U_2}{\mathrm{d}x_3} + \mathrm{i}k_2 U_3), \tag{4.55b}$$

$$\check{\sigma}_{33} = \lambda(\mathrm{i}k_1 U_1 + \mathrm{i}k_2 U_2 + \frac{\mathrm{d}U_3}{\mathrm{d}x_3}) + 2\mu\frac{\mathrm{d}U_3}{\mathrm{d}x_3}. \tag{4.55c}$$

The displacements and the traction stresses are collected in a vector $\mathbf{S}$

$$\mathbf{S}(k_1, k_2, x_3, \omega) = \begin{bmatrix}\mathbf{U} & \mathbf{P}\end{bmatrix}^{\mathrm{T}} = \begin{bmatrix}U_1 & U_2 & U_3 & \check{\sigma}_{13} & \check{\sigma}_{23} & \check{\sigma}_{33}\end{bmatrix}^{\mathrm{T}}. \tag{4.56}$$

For any layer j, the vector $\mathbf{S}^j$ can be written as

$$\mathbf{S}^j(k_1, k_2, x_3, \omega) = \mathbf{A}^j(k_1, k_2, \omega)\, \mathbf{E}^j(k_1, k_2, x_3, \omega)\, \mathbf{b}^j. \tag{4.57}$$

The vector $\mathbf{b}^j$ contains the integration constants governed by the boundary conditions at the top and the bottom of the layer,

$$\mathbf{b}^j = \begin{bmatrix} a_1 & b_1 & c_1 & a_2 & b_2 & c_2 \end{bmatrix}^{\mathrm{T}}. \tag{4.58}$$

The matrix $\mathbf{E}^j$ is defined as

$$\mathbf{E}^j(k_1, k_2, x_3, \omega) = \begin{bmatrix} e^{\alpha_p x_3} & 0 & 0 & 0 & 0 & 0 \\ 0 & e^{\alpha_s x_3} & 0 & 0 & 0 & 0 \\ 0 & 0 & e^{\alpha_s x_3} & 0 & 0 & 0 \\ 0 & 0 & 0 & e^{-\alpha_p x_3} & 0 & 0 \\ 0 & 0 & 0 & 0 & e^{-\alpha_s x_3} & 0 \\ 0 & 0 & 0 & 0 & 0 & e^{-\alpha_s x_3} \end{bmatrix}. \tag{4.59}$$

$\mathbf{A}^j(k_1, k_2, \omega)$ is a (6×6) matrix, where the entries follow from Eqs. (4.52–4.53) and Eq. (4.55). At the top of the j:th layer $\mathbf{E}^j$ is the identity matrix. Now, using the superscript ^{0} and ^{1} to refer to the top ($x_3 = 0$) or bottom ($x_3 = h$) of the layer, the vector $\mathbf{S}^j$ is, respectively

$$\mathbf{S}^{j0} = \mathbf{A}^j\, \mathbf{E}^{j0}\, \mathbf{b}^j = \mathbf{A}^j\, \mathbf{b}^j, \tag{4.60a}$$

$$\mathbf{S}^{j1} = \mathbf{A}^j\, \mathbf{E}^{j1}\, \mathbf{b}^j. \tag{4.60b}$$

The vector $\mathbf{b}^j$ of integration constants can be eliminated by expressing the vector $\mathbf{S}^j$ on either side of the layer in terms of the vector $\mathbf{S}^j$ on the other side, e.g.

$$\mathbf{S}^{j1} = \mathbf{A}^j\, \mathbf{E}^{j1}\, \mathbf{b}^j = \mathbf{A}^j\, \mathbf{E}^{j1}\, (\mathbf{A}^j)^{-1}\, \mathbf{S}^{j0}. \tag{4.61}$$

Due to continuity of displacements and tractions over interfaces between layers, several layers can be assembled in the same manner, forming a relationship between the displacement and stresses at the top of the stratum and at the bottom of the stratum. This is the layer transfer matrix approach by Thomson and Haskell [46,47]. For certain frequencies and stratifications, this method suffers from loss-of-precision. To circumvent these problems, in the current work, the different soil layers are assembled in an orthonormalization procedure [48]. The details are left out, and the interested reader is instead referred to [48]. With known boundary conditions at the lowest interface, a relationship between the traction and the displacement at the surface can be obtained,

$$\mathbf{U}^0(k_1, k_2, \omega) = \mathbf{G}(k_1, k_2, \omega)\, \mathbf{P}^0(k_1, k_2, \omega), \tag{4.62}$$

where

$$\mathbf{G} = \mathbf{G}(k_1, k_2, \omega) = \begin{bmatrix} G_{11} & G_{12} & G_{13} \\ G_{21} & G_{22} & G_{23} \\ G_{31} & G_{32} & G_{33} \end{bmatrix}, \tag{4.63}$$

is the Green's function for the layered half-space. The Green's function $\mathbf{G}(k_1, k_2, \omega)$, when multiplied by a traction vector for the surface $\mathbf{P}^0(k_1, k_2, \omega)$, gives the displacement vector

$\mathbf{U}^0(k_1, k_2, \omega)$ on the surface. The displacement vector is obtained in Cartesian space through a double inverse Fourier transform

$$u_i(x_1, x_2, x_3 = 0, \omega) = \frac{1}{4\pi^2} \int_{-\infty}^{\infty} \int_{-\infty}^{\infty} U_i e^{\mathrm{i}(k_1 x_1 + k_2 x_2)} \mathrm{d}k_1 \mathrm{d}k_2. \tag{4.64}$$

In practice, Eq. (4.62) is evaluated for a set of discrete values of k_1 and k_2, and Eq. (4.64) is evaluated using an inverse Fast Fourier Transform (iFFT) algorithm. The Green's function is calculated for $N \times N$ uniformly spaced wavenumbers (k_1, k_2) ranging from $k_i = -(\frac{N}{2} - 1)\Delta k$ to $k_i = (\frac{N}{2})\Delta k$, The displacements are then obtained in $N \times N$ uniformly spaced points in Cartesian space (x_1, x_2), spanning the area $\frac{2\pi}{\Delta k} \times \frac{2\pi}{\Delta k}$. Hence, the spacing between the points where the results are obtained is governed by the wavenumber increment and the number of points used to calculate the Green's function. To obtain accurate results, max(k) must be high enough to ensure that either $\mathbf{G} \approx 0$ or $\mathbf{P} \approx 0$ for $k >$ max(k), whereas Δk must be small enough to ensure that high gradients in either $\mathbf{G}$ or $\mathbf{P}$ are resolved.

4.2.3 Formulation in a moving frame of reference

In the same manner as for the FE formulation in a moving frame of reference, the coordinate transformation

$$(\tilde{x}_1, \tilde{x}_2, \tilde{x}_3) = (x_1 - vt, x_2, x_3), \tag{4.65}$$

is introduced, where v is the vehicle speed. Applying the transformation to the Navier equations Eq. (4.44) yields

$$(\lambda + \mu)\frac{\partial^2 \tilde{u}_j}{\partial \tilde{x}_i \partial \tilde{x}_j} + \mu \frac{\partial^2 \tilde{u}_i}{\partial \tilde{x}_j \partial \tilde{x}_j} = \rho\left(\frac{\partial^2 \tilde{u}_i}{\partial t^2} - 2v\frac{\partial^2 \tilde{u}_i}{\partial t \partial \tilde{x}_1} + v^2 \frac{\partial^2 \tilde{u}_i}{\partial^2 \tilde{x}_1}\right), \tag{4.66}$$

where $\tilde{u}_i = \tilde{u}_i(\tilde{x}_1, \tilde{x}_2, \tilde{x}_3, t)$ is the displacement in the moving frame of reference. Fourier transforming these equations with respect to the horizontal coordinates and time, $(\tilde{x}_1, \tilde{x}_2, t)$, yields the Navier equations in frequency–wavenumber domain as [42]

$$(\lambda + \mu)\tilde{\Delta}\mathrm{i}\tilde{k}_1 + \mu\left(\frac{\partial^2}{\partial \tilde{x}_3^2} - \tilde{k}_1^2 - \tilde{k}_2^2\right)\tilde{U}_1 = \rho(-\omega^2 + 2v\omega\tilde{k}_1 - v^2\tilde{k}_1^2)\tilde{U}_1, \tag{4.67a}$$

$$(\lambda + \mu)\tilde{\Delta}\mathrm{i}\tilde{k}_2 + \mu\left(\frac{\partial^2}{\partial \tilde{x}_3^2} - \tilde{k}_1^2 - \tilde{k}_2^2\right)\tilde{U}_2 = \rho(-\omega^2 + 2v\omega\tilde{k}_1 - v^2\tilde{k}_1^2)\tilde{U}_2, \tag{4.67b}$$

$$(\lambda + \mu)\frac{\partial \tilde{\Delta}}{\partial \tilde{x}_3} + \mu\left(\frac{\partial^2}{\partial \tilde{x}_3^2} - \tilde{k}_1^2 - \tilde{k}_2^2\right)\tilde{U}_3 = \rho(-\omega^2 + 2v\omega\tilde{k}_1 - v^2\tilde{k}_1^2)\tilde{U}_3. \tag{4.67c}$$

Here, a tilde is used to emphasize that a variable is expressed in terms of the moving $(\tilde{x}_1, \tilde{x}_2, \tilde{x}_3)$ coordinate system, i.e.

$$\tilde{U}_i(\tilde{k}_1, \tilde{k}_2, \tilde{x}_3, \omega) = \int_{-\infty}^{\infty} \int_{-\infty}^{\infty} \int_{-\infty}^{\infty} \tilde{u}_i e^{-\mathrm{i}(\tilde{k}_1 \tilde{x}_1 + \tilde{k}_2 \tilde{x}_2 + \omega t)} \mathrm{d}\tilde{x}_1 \mathrm{d}\tilde{x}_2 \mathrm{d}t, \tag{4.68}$$

where $\tilde{k}_1$ and $\tilde{k}_2$ are the wavenumbers in the direction of $\tilde{x}_1$ and $\tilde{x}_1$, respectively. Now, with

$$\tilde{\omega} = \omega - \tilde{k}_1 v, \tag{4.69}$$

Eq. (4.67) is written as

$$(\lambda+\mu)\tilde{\Delta}\mathrm{i}\tilde{k}_1 + \mu(\frac{\mathrm{d}^2}{\mathrm{d}\tilde{x}_3^2} - \tilde{k}_1^2 - \tilde{k}_2^2)\tilde{U}_1 = -\rho\tilde{\omega}^2\tilde{U}_1, \tag{4.70a}$$

$$(\lambda+\mu)\tilde{\Delta}\mathrm{i}\tilde{k}_2 + \mu(\frac{\mathrm{d}^2}{\mathrm{d}\tilde{x}_3^2} - \tilde{k}_1^2 - \tilde{k}_2^2)\tilde{U}_2 = -\rho\tilde{\omega}^2\tilde{U}_2, \tag{4.70b}$$

$$(\lambda+\mu)\frac{\mathrm{d}\tilde{\Delta}}{\mathrm{d}\tilde{x}_3} + \mu(\frac{\mathrm{d}^2}{\mathrm{d}\tilde{x}_3^2} - \tilde{k}_1^2 - \tilde{k}_2^2)\tilde{U}_3 = -\rho\tilde{\omega}^2\tilde{U}_3. \tag{4.70c}$$

These are the same equations as in Eq. (4.46). Hence, the solution procedure outlined in the previous subsection is applicable also in the moving frame of reference, with the difference being that the frequency is wavenumber dependent as given by Eq. (4.69). The frequency $\tilde{\omega}$ is the frequency of vibration of a material point.

5 Numerical Implementations

5.1 GENERAL REMARKS

As discussed in Section 2.5.2, several numerical techniques can be employed to predict the ground vibrations next to a railway track. In the appended papers a 3D model that combines the FE method and the LTM method, in a moving frame of reference following the vehicle, is utilized. Further, a model employing 2.5D FE for the railway track and the LTM method for the soil has recently been developed in the current research project and is presented here. The computational code for these models were implemented in FORTRAN by the author, utilizing Intel Math Kernel Library [49] for some of the mathematical operations. The response obtained for a particular case is compared to that obtained with a 2.5D FE–PML model employing FE also for the soil domain. The code for the latter model was implemented in MATLAB by the author.

A slab track consisting of a concrete slab, rails and rail pads, is considered. The slab width and thickness is $w = 3.0$ m and $t = 0.2$ m, respectively. The track is assumed to rest on a 14 m deep stiff clay till layer overlaying a half-space. The soil conditions corresponds to a site near the research facility MAX IV Laboratory in Lund, Sweden. The track, however, is hypothetical. All models are established in the moving reference frame following the load, implying that the track and soil are assumed invariant in the running direction. Hence, the discrete rail supports are considered as distributed. The track and soil properties are given in Tables 5.1 and 5.2, respectively.

Here, the rail displacements and the ground surface response 10 m from the track center line is studied, as a harmonic point load runs on the track with a velocity of $v = 30$ m/s ($= 108$ km/h). Two frequencies of excitation are considered, $f = 40$ Hz and $f = 80$ Hz.

The 3D model used in the appended papers is briefly recapitulated in Section 5.2. The coupled 2.5D model is described in Section 5.3. The 2.5D FE–PML model is described in Section 5.4. Finally, the response obtained with the three different models for the particular case studied here is presented and discussed in Section 5.5.

Table 5.1: Track properties.

	Parameter	Value
Rail	Mass (kg/m)	60
	Young's modulus (GPa)	210
	Second moment of inertia (m^4)	3.217×10^{-5}
	Loss factor (-)	0.01
	Track gauge (m)	1.435
Rail pads	Stiffness (MN/m^2)	250
	Damping (kNs/m^2)	22.5
Slab	Density (kg/m^3)	2500
	Young's modulus (GPa)	30
	Poisson's ratio	0.2
	Width (m)	3.0
	Thickness (m)	0.2
	Loss factor (-)	0.04

Table 5.2: Ground properties.

Layer	Parameter	Value
Soil	Depth (m)	14
	Young's modulus (MPa)	475
	Poisson's ratio	0.48
	Density (kg/m^3)	2125
	Loss factor (-)	0.14
Bedrock (half-space)	Depth (m)	∞
	Young's modulus (MPa)	8800
	Poisson's ratio	0.40
	Density (kg/m^3)	2600
	Loss factor (-)	0.04

5.2 A COUPLED 3D TRACK–SOIL MODEL

In this specific example, the track slab is modeled using 3D solid elements, following the formulation in the moving frame of reference as described in Section 4.1.3. The soil is described by a dynamic stiffness matrix for a set of nodes where the slab interacts with the ground. These nodes are referred to as soil-structure interaction (SSI) nodes.

The soil dynamic stiffness matrix is derived from the Green's function of the layered soil in the moving reference frame, as described in Section 4.2.3, and can be interpreted as a super-element to which the track structure is coupled. The total system of equations is then solved and the forces in the slab–soil interface, i.e. the SSI nodes, are obtained. Finally, the Green's function is used for establishing the total displacement response in the free-field as a summation of contributions from each individual SSI node.

5.2.1 FE model of track

The track slab is modeled using 3D solid continuum elements, for which the formulation in a moving frame of reference was given in Section 4.1.3. Fully integrated linear brick elements with 8 nodes and 3 translational DoFs per node are used. Six elements are used in the thickness direction of the slab, and an element length of 0.15×0.15 m in the (x_1, x_2)-plane is used. The rails are represented by Bernoulli–Euler beam elements with two nodes, each node having a rotational DoF and a vertical translational DoF. The beam elements are coupled to the solid elements through visco-elastic interface elements, composed of continuously distributed springs and dashpots, representing the rail pads. The formulation of these elements are presented in both Paper A and Paper C. Damping is introduced into the slab and the rails by the use of complex Young's moduli, $E^* = E(1+i\eta)$, where η is the loss factor, leading to a frequency independent damping as described in Section 3.2.3. Assuming a harmonic excitation with the

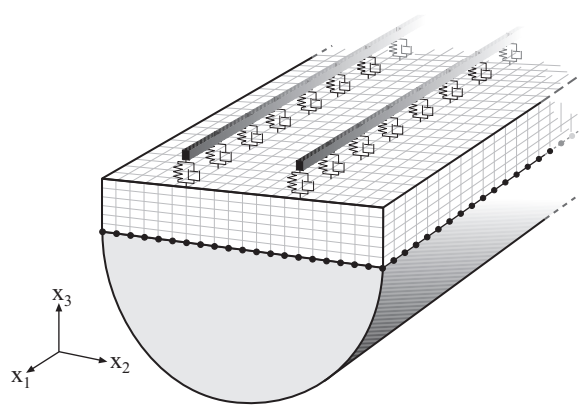

Figure 5.1: Illustration of 3D FE mesh of a railway track coupled to a horizontally layered half-space.

angular frequency $\omega = 2\pi f$, the governing equations for the track can be written as

$$(-\omega^2 \mathbf{M}_t + \mathrm{i}\omega \mathbf{C}_t + \mathbf{K}_t)\hat{\mathbf{u}}_t = \mathbf{D}_t(\omega)\hat{\mathbf{u}}_t = \hat{\mathbf{f}}_t, \tag{5.1}$$

where $\mathbf{M}_t$, $\mathbf{C}_t$ and $\mathbf{K}_t$ is the mass, damping and (complex) stiffness matrix, respectively, for the total track system (excluding the underlying soil). Further, $\mathbf{D}_t(\omega)$ is the corresponding dynamic stiffness matrix. The vector $\hat{\mathbf{u}}_t$ contains the displacements in the track DoFs, and the vector $\hat{\mathbf{f}}_t$ contains the externally applied loads.

5.2.2 Soil dynamic stiffness matrix

Assuming that the track structure contains m nodes on the soil interface, each with three translational DoFs, a $(3m \times 3m)$ dynamic stiffness matrix $\mathbf{D}_s(f)$ for the soil super-element, i.e. the m SSI nodes, is to be determined. Here, advantage is taken of the assumed invariability of the soil in the horizontal directions.

The first step involves calculating the soil response due to a unit harmonic load, with frequency f, moving along the x_1-axis on the soil surface with velocity v. The unit load is evenly distributed over a rectangular area, the size of which is chosen as equal to the element size of the connecting track. Hence, with reference to Sections 4.1.3 and 4.2.3, the traction is distributed over a rectangular area centered in the origin of the moving coordinate system $(\tilde{x}_1, \tilde{x}_2, \tilde{x}_3)$, as

$$p_j(\tilde{x}_1, \tilde{x}_2, \omega) = \begin{cases} 1/(4ab), & -a < \tilde{x}_1 < a,\ -b < \tilde{x}_2 < b \\ 0, & \text{otherwise} \end{cases}, \tag{5.2}$$

where $2a$ and $2b$ is the width in the $\tilde{x}_1$ and $\tilde{x}_2$ directions, respectively. In the current example, $2a = 2b = 0.15$. In wavenumber domain the traction becomes

$$\hat{p}_j(\tilde{k}_1, \tilde{k}_2, \omega) = \frac{\sin(\tilde{k}_1 a)}{\tilde{k}_1 a} \frac{\sin(\tilde{k}_2 b)}{\tilde{k}_2 b}. \tag{5.3}$$

The soil surface displacement response is calculated in frequency–wavenumber domain $(\tilde{k}_1, \tilde{k}_2, \omega)$, for $N \times N$ wavenumbers, using the LTM method in accordance with Section 4.2. After a discrete inverse Fourier transform the soil surface response, in terms of complex displacements $(\tilde{u}_1, \tilde{u}_2, \tilde{u}_3)$, is obtained in $N \times N$ points in the moving coordinate system $(\tilde{x}_1, \tilde{x}_2, \tilde{x}_3)$. In the moving frame of reference, the response in each point of the soil surface is harmonic with the frequency of the excitation. The area spanned by the response surface depend on the wavenumber increment, and the spacing between the response points depend on the number of points N, as described in Section 4.2.2. In the current example $N = 4096$ and $max(\tilde{k}_1) = max(\tilde{k}_2) = 2\pi/0.15$ rad/m, which has been found to be sufficient in the case studied here. Figure 5.2 shows a response surface of the vertical displacement due to a vertical unit harmonic load.

The soil surface displacements are calculated separately for a unit load in each of the three $(\tilde{x}_1, \tilde{x}_2, \tilde{x}_3)$ directions, i.e. nine response surfaces are obtained, here denoted $U(i, j, \tilde{x}_1, \tilde{x}_2)$

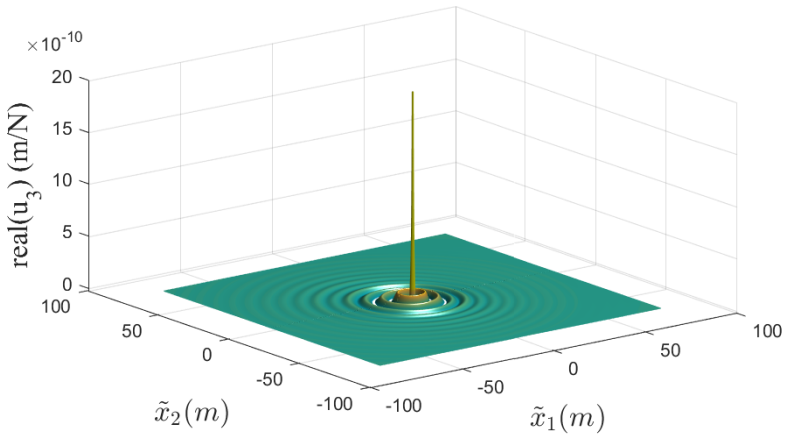

Figure 5.2: Response surface showing the real part of the vertical displacement due to a rectangular vertical unit load with $f = 40$ Hz and $v = 30$ m/s.

where $i(= 1, 2, 3)$ is the load direction and $j(= 1, 2, 3)$ is the displacement direction. A $(3m \times 3m)$ flexibility matrix for the m SSI nodes, $\mathbf{H}_{\mathrm{s}}(\omega)$, is established by interpolating from the nine response surfaces.

Let DoF q_j denote the displacement in direction j of node q. Similarly, let DoF r_i denote the displacement in direction i of node r. Element (q_j, r_i) of the flexibility matrix contains the complex displacements in DoF q_j due to a unit load in DoF r_i. Letting $\Delta\tilde{x}_1$ and $\Delta\tilde{x}_2$ denote the distance between nodes q and r in the $\tilde{x}_1$- and $\tilde{x}_2$-directions, then the flexibility matrix element (q_j, r_i) is obtained as

$$H_{q_j r_i} = U(i, j, \Delta\tilde{x}_1, \Delta\tilde{x}_2). \tag{5.4}$$

Finally, the dynamic stiffness matrix of the soil is obtained as the inverse of the flexibility matrix, i.e. $\mathbf{D}_{\mathrm{s}}(\omega) = \mathbf{H}_{\mathrm{s}}^{-1}(\omega)$, and the following equation applies for the soil super-element,

$$\mathbf{D}_{\mathrm{s}}(\omega)\hat{\mathbf{u}}_{\mathrm{s}} = \hat{\mathbf{f}}_{\mathrm{s}}, \tag{5.5}$$

where the vector $\hat{\mathbf{u}}_{\mathrm{s}}$ contains the displacements in the SSI DoFs, and the vector $\hat{\mathbf{f}}_{\mathrm{s}}$ contains the externally applied loads.

5.2.3 Solution of global equations

When the dynamic stiffness matrices of the track and the soil, $\mathbf{D}_{\mathrm{t}}$ and $\mathbf{D}_{\mathrm{s}}$, have been determined, they are assembled in a standard FE manner forming a total dynamic stiffness for the track and soil system, $\mathbf{D}_{\mathrm{g}}$.

The following equation applies to the coupled track and soil system,

$$\mathbf{D}_{\mathrm{g}}(\omega)\hat{\mathbf{u}}_{\mathrm{t}} = \hat{\mathbf{f}}_{\mathrm{t}}. \tag{5.6}$$

The load vector $\hat{\mathbf{f}}_{\mathrm{t}}$ is zero except for the rows corresponding to the rail loading points DoFs. The SSI DoFs $\hat{\mathbf{u}}_{\mathrm{s}}$ are a subset of the track DoFs $\hat{\mathbf{u}}_{\mathrm{t}}$. Hence, when Eq. (5.6) has been solved, the corresponding forces in the SSI DoFs are obtained as

$$\hat{\mathbf{f}}_{\mathrm{s}} = \mathbf{D}_{\mathrm{s}}(\omega)\hat{\mathbf{u}}_{\mathrm{s}}. \tag{5.7}$$

Now, a second flexibility matrix $\mathbf{H}_{\mathrm{s,f}}(\omega)$ is defined, again by using the response surfaces $U(i, j, \tilde{x}_1, \tilde{x}_2)$ in a procedure similar to the one described above, to express the displacements in a number of points in the free-field due to loading of the SSI DoFs. The free-field displacements are then obtained as $\mathbf{u}_{\mathrm{f}} = \mathbf{H}_{\mathrm{s,f}}(\omega)\mathbf{f}_{\mathrm{s}}$.

5.3 A COUPLED 2.5D TRACK–SOIL MODEL

By combining the 2.5D FE method with the semi-analytical soil representation a very time efficient model is obtained. Here, the track cross-section in the (x_2, x_3)-plane is represented by a 2D mesh comprising 2.5D elements. For each discrete wavenumber k_1 in the x_1-direction, a dynamic stiffness matrix for the track is calculated, which is coupled to a dynamic stiffness matrix representing the soil, calculated from the Green's function of the layered half-space using the LTM method.

5.3.1 FE model of track

The track slab cross-section is modeled using 2.5D solid elements in the (x_2, x_3)-plane. The governing FE equations for such elements were presented in Section 4.1.4. Here, fully integrated 4-node isoparametric quadrilateral elements with linear shape functions are used. Six elements are used in the thickness direction of the slab, and an element length of 0.15 m is

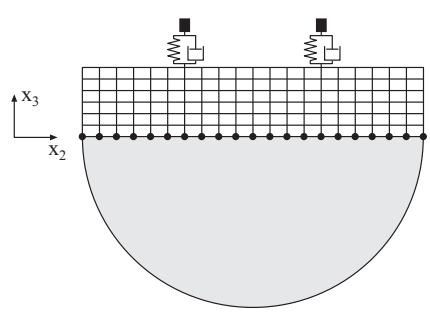

Figure 5.3: Illustration of a 2D FE mesh coupled to a horizontally layered half-space.

used in the x_2-direction. As described in Section 4.1.4, the calculations are performed in the moving frame of reference following the load at velocity v, by evaluating the stiffness matrices for the frequency $\tilde{\omega} = \omega - k_1 v$, where ω is the actual frequency of excitation by the moving harmonic load. A dynamic stiffness matrix for the track slab, $\mathbf{D}_p(\tilde{k}_1, \tilde{\omega})$, is established in accordance with Eq. (4.35). The rail and rail pads, for which the dynamic stiffness is derived below, is coupled to the slab.

Each rail is represented by a Bernoulli–Euler beam of infinite length, with bending stiffness $(EI)_r$ and mass m_r, continuously supported by distributed springs and dashpots representing the rail pads, with stiffness k_P and damping c_P. The rail is subjected to a harmonic load P_0 with circular frequency ω, moving in the positive x_1-direction with the velocity v. The governing equation for the rail can be written as

$$(EI)_r \frac{\partial^4 u_r}{\partial x^4} + m_r \frac{\partial^2 u_r}{\partial t^2} + k_P\Big(u_r - u_s\Big) + c_P\Big(\frac{\partial u_r}{\partial t} - \frac{\partial u_s}{\partial t}\Big) = \delta(x - vt) P_0 \mathrm{e}^{\mathrm{i}\omega t}. \quad (5.8)$$

Here, $u_r = u_r(x_1, t)$ is the vertical displacement of the rail and $u_s = u_s(x_1, t)$ is the vertical displacement of the slab directly under the rail. The equation is obtained in the frame of reference following the load by applying the coordinate transformation in Eq. (4.13),

$$\begin{aligned}(EI)_r \frac{\partial^4 \tilde{u}_r}{\partial \tilde{x}^4} + m_r\Big(\frac{\partial^2 \tilde{u}_r}{\partial t^2} - 2v\frac{\partial^2 \tilde{u}_r}{\partial \tilde{x}\partial t} + v^2\frac{\partial^2 \tilde{u}_r}{\partial \tilde{x}^2}\Big) + k_P\Big(\tilde{u}_r - \tilde{u}_s\Big) + \\ c_P\Big((\frac{\partial \tilde{u}_r}{\partial t} - v\frac{\partial \tilde{u}_r}{\partial \tilde{x}}) - (\frac{\partial \tilde{u}_s}{\partial t} - v\frac{\partial \tilde{u}_s}{\partial \tilde{x}})\Big) = \delta(\tilde{x}) P_0 \mathrm{e}^{\mathrm{i}\omega t},\end{aligned} \quad (5.9)$$

where, again, $\tilde{}$ denotes that a variable is expressed in the moving frame of reference. Fourier transforming Eq. (5.9) with respect to $\tilde{x}$ yields

$$\begin{aligned}(EI)_r \tilde{k}_1^4 \bar{u}_r + m_r\Big(\frac{\partial^2 \bar{u}_r}{\partial t^2} - 2\mathrm{i}v\tilde{k}_1\frac{\partial \bar{u}_r}{\partial t} - v^2\tilde{k}_1^2\bar{u}_r\Big) + k_P\Big(\bar{u}_r - \bar{u}_s\Big) + \\ c_P\Big((\frac{\partial \bar{u}_r}{\partial t} - \mathrm{i}v\bar{u}_r) - (\frac{\partial \bar{u}_s}{\partial t} - \mathrm{i}v\bar{u}_s)\Big) = P_0 \mathrm{e}^{\mathrm{i}\omega t},\end{aligned} \quad (5.10)$$

with $\bar{u} = \bar{u}(\tilde{k}_1, t) = \int_{-\infty}^{\infty} \tilde{u}(\tilde{x}, t)\mathrm{e}^{-\mathrm{i}\tilde{k}_1\tilde{x}}\mathrm{d}\tilde{x}$, and $\tilde{k}_1$ denotes the wavenumber in the direction of $\tilde{x}$.

Further, assuming steady-state vibration with circular frequency ω, i.e. $\bar{u}(\tilde{k}_1, t) = \breve{u}(\tilde{k}_1)\mathrm{e}^{\mathrm{i}\omega t}$ and setting $\tilde{\omega} = \omega - \tilde{k}_1 v$ yields

$$(EI)_r \tilde{k}_1^4 \breve{u}_r - \tilde{\omega}^2 m_r \breve{u}_r + k_P\Big(\breve{u}_r - \breve{u}_s\Big) + \mathrm{i}\omega c_P\Big(\breve{u}_r - \breve{u}_s\Big) = P_0. \quad (5.11)$$

Based on the above equation, a one-dimensional element similar to a simple Kelvin-Voight element can be formulated for the rail and rail pad in $\tilde{k}_1$-domain, governed by

$$\begin{bmatrix}(EI)_r\tilde{k}_1^4 - \tilde{\omega}^2 m_r + k_P + \mathrm{i}\tilde{\omega}c_P & -(k_P + \mathrm{i}\tilde{\omega}c_P) \\ -(k_P + \mathrm{i}\tilde{\omega}c_P) & k_P + \mathrm{i}\tilde{\omega}c_P\end{bmatrix}\begin{bmatrix}\breve{u}_r \\ \breve{u}_s\end{bmatrix} = \begin{bmatrix}P_0 \\ f_s\end{bmatrix}, \quad (5.12)$$

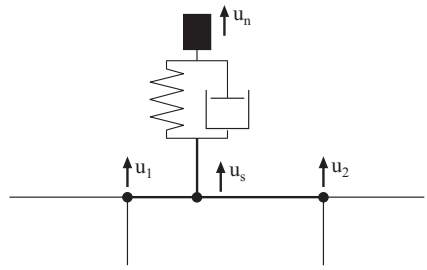

Figure 5.4: Coupling of rail and rail pad element to underlying slab element.

which can be written as $\mathbf{D}_\mathrm{r}\check{\mathbf{u}}_\mathrm{r} = \check{\mathbf{f}}_\mathrm{r}$.

In the general case, the rail element is not located directly over a node of the track slab mesh. Hence, the vertical displacement at the contact point between the rail and the slab, $\check{u}_\mathrm{s}$, is expressed in terms of the shape functions and vertical displacements of the two nodes spanning the edge of the connecting slab element, as

$$\check{u}_\mathrm{s} = N_1\check{u}_1 + N_2\check{u}_2, \tag{5.13}$$

where the shape functions N_1 and N_2 are evaluated at the coordinate of the slab–rail contact point. It can be shown that this leads to the following dynamic stiffness matrix for the rail element,

$$\mathbf{D}_\mathrm{r} = \begin{bmatrix} (EI)_r\tilde{k}_1^4 - \tilde{\omega}^2 m_r + k_P + \mathrm{i}\tilde{\omega}c_P & -N_1(k_P + \mathrm{i}\tilde{\omega}c_P) & -N_2(k_P + \mathrm{i}\tilde{\omega}c_P) \\ -N_1(k_P + \mathrm{i}\tilde{\omega}c_P) & N_1^2(k_P + \mathrm{i}\tilde{\omega}c_P) & N_1N_2(k_P + \mathrm{i}\tilde{\omega}c_P) \\ -N_2(k_P + \mathrm{i}\tilde{\omega}c_P) & N_1N_2(k_P + \mathrm{i}\tilde{\omega}c_P) & N_2^2(k_P + \mathrm{i}\tilde{\omega}c_P) \end{bmatrix}, \tag{5.14}$$

with the corresponding DoFs $(\check{u}_r, \check{u}_1, \check{u}_2)$. The dynamic stiffness matrices for slab and the two rails can now be assembled into one for the whole track structure, $\mathbf{D}_\mathrm{t}$, pertaining to the displacements of all the track DoFs $\check{\mathbf{u}}_\mathrm{t}$. Damping is introduced into the slab and the rails by the use of complex Young's moduli, $E^* = E(1 + \mathrm{i}\,\mathrm{sgn}(\tilde{\omega})\eta)$, where sgn is the sign function and η is the loss factor, leading to a frequency independent damping as described in Section 3.2.3.

5.3.2 Soil dynamic stiffness matrix

To derive the dynamic stiffness matrix of the soil, the slab–soil interface is discretized into n strips with a uniform width, where n is the number of elements in the slab. Hence, the width of a single strip is $\Delta = w/n$, where w is the slab width.

First, a single strip centered around the $\tilde{x}_2$-axis, with a unit harmonic force in direction j is considered. In this section, the argument $\tilde{\omega}$ has been dropped for brevity; it is understood that a harmonic response with the angular frequency $\tilde{\omega} = \omega - \tilde{k}_1 v$ is considered. The strip stress

is

$$p_j(\tilde{x_1}, \tilde{x_2}) = \begin{cases} \frac{1}{\Delta}, & -\Delta/2 < \tilde{x}_2 < \Delta/2 \\ 0, & \text{otherwise} \end{cases}. \tag{5.15}$$

In wavenumber domain the interface stress becomes

$$\hat{p}_j(\tilde{k}_1, \tilde{k}_2) = \frac{\sin(\tilde{k}_2\Delta/2)}{\tilde{k}_2\Delta/2}. \tag{5.16}$$

The soil surface displacement in direction i due to the soil surface stress in direction j is denoted $\hat{u}_{ij}$. From Eq. (4.62) this displacement is obtained as $\hat{u}_{ij}(\tilde{k}_1, \tilde{k}_2) = G_{ij}(\tilde{k}_1, \tilde{k}_2)\hat{p}_j(\tilde{k}_1, \tilde{k}_2)$ (no summation on repeated indices).

By performing an inverse Fourier transform with respect to wavenumber $\tilde{k}_2$, the soil displacement at an arbitrary $\tilde{x}_2$-coordinate is obtained as

$$\begin{aligned} \breve{\tilde{u}}_{ij}(\tilde{k}_1, \tilde{x}_2) &= \frac{1}{2\pi}\int_{-\infty}^{\infty} \hat{u}_{ij}(\tilde{k}_1, \tilde{k}_2)\mathrm{e}^{\mathrm{i}\tilde{k}_2\tilde{x}_2}\mathrm{d}\tilde{k}_2 = \frac{1}{2\pi}\int_{-\infty}^{\infty} G_{ij}(\tilde{k}_1, \tilde{k}_2)\hat{p}_j(\tilde{k}_1, \tilde{k}_2)\mathrm{e}^{\mathrm{i}\tilde{k}_2\tilde{x}_2}\mathrm{d}\tilde{k}_2 \\ &= \frac{1}{2\pi}\int_{-\infty}^{\infty} G_{ij}(\tilde{k}_1, \tilde{k}_2)\frac{\sin(\tilde{k}_2\Delta/2)}{\tilde{k}_2\Delta/2}\mathrm{e}^{\mathrm{i}\tilde{k}_2\tilde{x}_2}\mathrm{d}\tilde{k}_2 = \breve{H}_{ij}(\tilde{k}_1, \tilde{x}_2). \end{aligned} \tag{5.17}$$

$\breve{H}_{ij}(\tilde{k}_1, \tilde{x}_2)$ is a transfer function, expressing the displacements at $\tilde{x}_2$ due to a unit load at the strip centered around $\tilde{x}_2 = 0$. Due to the translational invariability of the soil, $\breve{H}_{ij}(\tilde{k}_1, \tilde{x}_2)$ can be used for calculating the soil displacement at any distance along the $\tilde{x}_2$-axis from any loaded strip, by replacing the coordinate $\tilde{x}_2$ with the distance between the mid-points of the "source strip" and the "receiver strip". Hence, for each wavenumber $\tilde{k}_1$, a flexibility matrix, linking the displacements and forces in all the n strips, is established as

$$\begin{bmatrix} \breve{H}_{11}(0) & \breve{H}_{12}(0) & ... & \breve{H}_{13}(-(n-1)\Delta) \\ \breve{H}_{21}(0) & \breve{H}_{22}(0) & ... & \breve{H}_{23}(-(n-1)\Delta) \\ \breve{H}_{31}(0) & \breve{H}_{32}(0) & ... & \breve{H}_{33}(-(n-1)\Delta) \\ \breve{H}_{11}(\Delta) & \breve{H}_{12}(\Delta) & ... & \breve{H}_{13}(-(n-2)\Delta) \\ \vdots & \vdots & ... & \vdots \\ \breve{H}_{31}((n-1)\Delta) & \breve{H}_{32}((n-1)\Delta) & ... & \breve{H}_{33}(0) \end{bmatrix} \begin{bmatrix} \breve{f}_{1x} \\ \breve{f}_{1y} \\ \vdots \\ \breve{f}_{nz} \end{bmatrix} = \begin{bmatrix} \breve{u}_{1x} \\ \breve{u}_{1y} \\ \vdots \\ \breve{u}_{nz} \end{bmatrix}, \tag{5.18}$$

where the argument $\tilde{k}_1$ has been dropped for brevity. Equation (5.18) can be written as $\breve{\mathbf{H}}_\mathrm{s}\breve{\mathbf{f}}_\mathrm{s} = \breve{\mathbf{u}}_\mathrm{s}$, where $\breve{\mathbf{u}}_\mathrm{s}$ and $\breve{\mathbf{f}}_\mathrm{s}$ are vectors containing displacements and forces respectively. Hence, the dynamic stiffness matrix is obtained as $\mathbf{D}_\mathrm{s} = \breve{\mathbf{H}}_\mathrm{s}^{-1}$. For the discretized soil interface, the following equation relates the total forces on each strip to the displacements in the mid-point of each strip,

$$\mathbf{D}_\mathrm{s}\breve{\mathbf{u}}_\mathrm{s} = \breve{\mathbf{f}}_\mathrm{s}. \tag{5.19}$$

It is emphasized that Eq. (5.19) applies for a given wavenumber $\tilde{k}_1$ and frequency $\tilde{\omega}$, i.e. $\mathbf{D}_\mathrm{s} = \mathbf{D}_\mathrm{s}(\tilde{k}_1, \tilde{\omega})$, $\breve{\mathbf{u}}_\mathrm{s} = \breve{\mathbf{u}}_\mathrm{s}(\tilde{k}_1, \tilde{\omega})$, and $\breve{\mathbf{f}}_\mathrm{s} = \breve{\mathbf{f}}_\mathrm{s}(\tilde{k}_1, \tilde{\omega})$. For each $\tilde{k}_1$, however, a loop over a set of wavenumbers $\tilde{k}_2$ in the $\tilde{x}_2$-direction is necessary for the evaluation of the Green's function and Eq. (5.17).

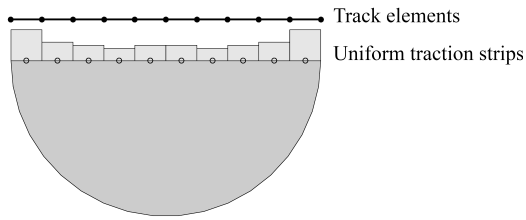

Figure 5.5: Strips of uniform traction on the soil. The nodes and edges of the connecting track elements are also shown.

5.3.3 Coupling of track and soil

The "interaction points" of the discretized soil interface are located at the mid-point of each strip, whereas the nodes of the track elements at the interface are located in the strip end-points. The two domains are initially uncoupled. To couple the two domains, a transformation matrix is used to enforce displacement compatibility between the mid-point of each soil strip and the corresponding point of the FE mesh. A similar procedure was followed in [32] to couple 2.5D boundary elements to a FE mesh. The displacements in the soil strip mid-points, $\check{\mathbf{u}}_{\mathrm{s}}$, are expressed in terms of the displacements of the track nodes at the interface, $\check{\mathbf{u}}_{\mathrm{st}}$ as

$$\check{\mathbf{u}}_{\mathrm{s}} = \mathbf{T}\check{\mathbf{u}}_{\mathrm{st}}, \tag{5.20}$$

where the transformation matrix $\mathbf{T}$ depends on the element shape functions in the track elements. Because linear elements are used for the track, and the soil strip mid-points are located in the center of each corresponding track element, Eq. (5.20) states that the displacements of each soil strip mid-point equal the average displacements in the two nodes spanning the edge of the connecting element. The same transformation matrix is used to relate the forces from the soil strips to the actual track nodes,

$$\check{\mathbf{f}}_{\mathrm{st}} = \mathbf{T}^{\mathrm{T}}\check{\mathbf{f}}_{\mathrm{s}}, \tag{5.21}$$

Hence, in terms of the track DoFs of the track–soil interface, the dynamic equilibrium for the soil can be written as

$$\mathbf{D}_{\mathrm{st}}\check{\mathbf{u}}_{\mathrm{st}} = \check{\mathbf{f}}_{\mathrm{st}}, \tag{5.22}$$

with $\mathbf{D}_{\mathrm{st}} = \mathbf{T}^{\mathrm{T}}\mathbf{D}_{\mathrm{s}}\mathbf{T}$.

5.3.4 Solution of global equations

The dynamic stiffness matrices for the soil, $\mathbf{D}_{\mathrm{st}}$, and the track, $\mathbf{D}_{\mathrm{t}}$ can now be assembled in a standard manner leading to a global dynamic stiffness matrix for the coupled soil and track system, $\mathbf{D}_{\mathrm{g}} = \mathbf{D}_{\mathrm{g}}(\tilde{k}_1)$. The displacements of the track DoFs, $\check{\mathbf{u}}_{\mathrm{t}} = \check{\mathbf{u}}_{\mathrm{t}}(\tilde{k}_1)$ are solved from

$$\mathbf{D}_{\mathrm{g}}\check{\mathbf{u}}_{\mathrm{t}} = \check{\mathbf{f}}_{\mathrm{t}}, \tag{5.23}$$

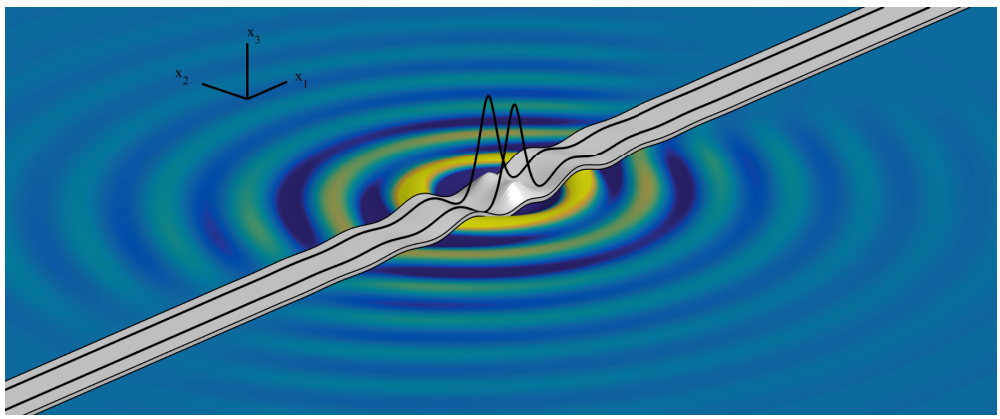

Figure 5.6: Contour plot showing the vertical displacement of the soil surface as obtained with the coupled 2.5D model for the excitation frequency $f = 80$ Hz.

where $\check{\mathbf{f}}_{\mathrm{t}} = \check{\mathbf{f}}_{\mathrm{t}}(\tilde{k}_1)$ is a force vector containing the external loads. The only external loads are the harmonic point loads P_0 on each rail, moving with velocity v in the positive x_1-direction, i.e. $f(x_1, t) = P_0\delta(x_1 - vt)e^{\mathrm{i}\omega t}$. In the moving coordinate system this becomes $\tilde{f}(\tilde{x}_1, t) = P_0\delta(\tilde{x}_1)e^{\mathrm{i}\omega t}$, and after a Fourier transform with respect to $\tilde{x}_1$ and t the load is described by $\check{f}(\tilde{k}_1, \omega) = P_0$. This means that the same load, P_0, is applied to the rail DoF for each wavenumber k_1. The displacements $\check{\mathbf{u}}_{\mathrm{s}}(\tilde{k}_1)$ in the mid-points of the element edges, corresponding to the mid-points of the soil strips, are then obtained from Eq. (5.20), from which the soil strip forces, $\check{\mathbf{f}}_{\mathrm{s}}(\tilde{k}_1)$, can be obtained from Eq. (5.19). When the magnitude of the strip forces are known the total traction on the soil surface for the current wavenumber, $\tilde{k}_1$, is obtained by superposition of the contributions from each individual strip. The traction in $(\tilde{k}_1, \tilde{k}_2)$-domain due to a single strip centered around the $\tilde{x}_2$-axis was given in Eq. (5.16). The traction due to a strip centered around the coordinate $\tilde{x}_2 = d$ is then given by the translation operation, i.e.

$$\hat{p}_j(\tilde{k}_1, \tilde{k}_2) = \frac{\sin(\tilde{k}_2\Delta/2)}{\tilde{k}_2\Delta/2}\mathrm{e}^{\mathrm{i}d\tilde{k}_2}. \tag{5.24}$$

Each such (unit force) strip traction is scaled by the corresponding strip force in the vector $\check{\mathbf{f}}_{\mathrm{s}}(\tilde{k}_1)$.

The calculations described here are carried out for N discrete wavenumbers $\tilde{k}_1$ corresponding to the $\tilde{x}_1$-direction. That is, for each wavenumber $\tilde{k}_1$, the dynamic stiffness matrix of the 2D FE mesh is established, and coupled to a dynamic stiffness matrix for the soil. The establishment of the Green's function and the soil dynamic stiffness matrix, for each wavenumber $\tilde{k}_1$, requires a loop over M discrete wavenumbers $\tilde{k}_2$ corresponding to the $\tilde{x}_2$-direction. In the current example, $N = M = 4096$ was chosen, with $max(\tilde{k}_1) = max(\tilde{k}_2) = 2\pi/0.15$ rad/m, i.e. the same wavenumber discretization that was used in the 3D model.

The global displacements of the soil surface are calculated in $(\tilde{k}_1, \tilde{k}_2)$-domain using Eq. (4.62). These displacements are obtained in $(\tilde{x}_1, \tilde{x}_2)$-space by a double inverse Fourier transform. The

complex nodal displacements of the track structure, $\hat{\mathbf{u}}_t(\tilde{x}_1)$, are obtained in N points along the $(\tilde{x}_1)$-axis after an inverse Fourier transform of $\check{\mathbf{u}}_t(\tilde{k}_1)$, see Figure 5.6.

5.4 A 2.5D FE–PML MODEL

In this model, both the track slab and the soil is represented by 2.5D solid elements in the (x_2, x_3)-plane. The governing FE equations for such elements were presented in Section 4.1.4. Here, fully integrated isoparametric 8-node elements with quadratic shape functions are used. The modeling of the rails and rail pads is identical to the description in Section 5.3, i.e. by a one-dimensional element the rail and rail pad in k_1-domain governed by Eq. (5.12). The only difference is that the coupling of the rail to the slab now accounts for the fact that the slab is described by quadratic elements.

5.4.1 FE model of track and soil

Six elements are used in the thickness direction of the slab, and an element length of 0.3 m is used in the x_2-direction. For the soil, the element length is approximately 0.3 m in both directions. Only half of the track and the surrounding soil is modeled, with symmetry conditions applied to the boundary in $x_2 = 0$. PMLs, as described in Section 4.1.5, are used to artificially attenuate the waves at the truncated sides of the model. The attenuation function for evanescent waves, $f_j^e(x_j)$ is set to zero. A linear attenuation function for propagating waves is used, as $f_j^p(x_j) = 20(x_j - x_{j0})/L_{PML}$ [44] where x_{j0} is the x_j-coordinate at the

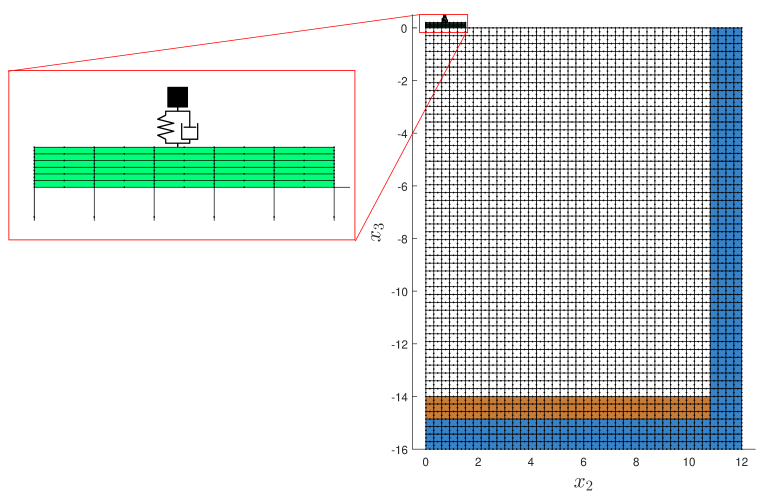

Figure 5.7: Mesh used in 2.5D FE–PML model. Blue colored elements are PML elements. Brown colored elements belong to the half-space material. A magnification of the slab (green colored elements) is shown inside the red box.

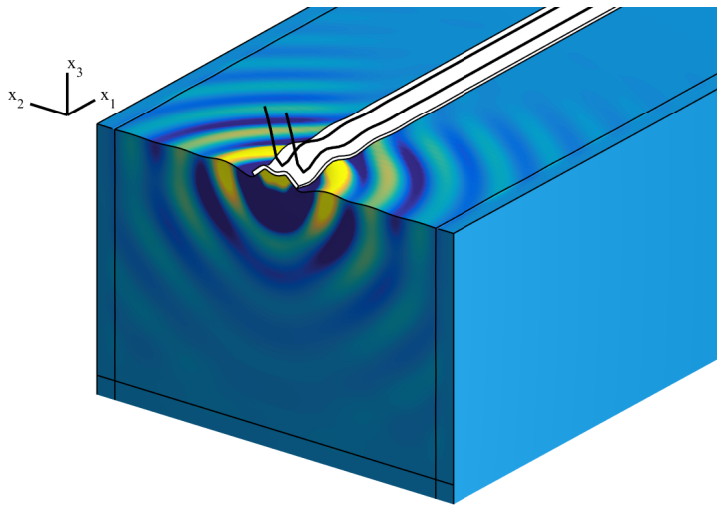

Figure 5.8: Contour plot showing the vertical displacement of the soil for the excitation frequency $f = 80$ Hz. The waves are effectively attenuated inside the PML.

interface between the regular and the PML domain. Material damping is introduced into the whole model by the use of complex Young's moduli, $E^* = E(1 + \mathrm{i}\,\mathrm{sgn}(\tilde{\omega})\eta)$, where η is the loss factor and sgn is the sign function. The FE mesh is shown in Figure 5.7.

5.4.2 Solution of global equations

As described in Section 4.1.4, the calculations are performed in the moving frame of reference following the load at velocity v, by evaluating the stiffness matrices for the frequency $\tilde{\omega} = \omega - \tilde{k}_1 v$, where ω is the actual frequency of excitation by the moving harmonic load. A global dynamic stiffness matrix for the entire computational domain, $\mathbf{D}_\mathrm{g}(\tilde{k}_1)$, is established for each of the N discrete wavenumbers $\tilde{k}_1$ in the $\tilde{x}_1$-direction. The nodal displacement vector $\check{\mathbf{u}}(\tilde{k}_1)$ is solved from $\mathbf{D}_\mathrm{g}\check{\mathbf{u}} = \check{\mathbf{f}}$. The only external load is the point load (P_0) on the rail, which are constant for all wavenumbers as discussed in Section 5.3.4. In the current example $N = 4096$ with $max(\tilde{k}_1) = 5$ rad/m. The complex nodal displacements $\hat{\mathbf{u}}(\tilde{x}_1)$ are obtained in N points along the $(\tilde{x}_1)$-axis after an inverse Fourier transform of $\check{\mathbf{u}}(\tilde{k}_1)$, see Figure 5.8.

5.5 DISCUSSION

All three models described above are formulated in a moving frame of reference, following the load at the velocity $v = 30$ m/s. The results are therefore obtained in this moving reference frame. Since the loading is harmonic with frequency ω, the response is also harmonic with the same frequency. To compare the response from the three models, the absolute value of the vertical displacement is extracted along a line located 10 m from the track center line, see

Figure 5.9, as well as along the rail, see Figure 5.10. The displacements are plotted against the track direction coordinate $\tilde{x}_1$, where $\tilde{x}_1 = 0$ corresponds to a point perpendicular to the moving load, and positive values of $\tilde{x}_1$ correspond to points in front of the load.

All three models yield very similar response, both regarding the rail displacements and the free-field displacements. The maximum difference of the peak values is obtained for the higher frequency, where it is still less than 3%. The small differences that do exist are believed to be caused mainly by the different track–soil interface stress conditions. The traction on the soil surface from the two models employing a soil dynamic stiffness based on the semi-analytic approach, is composed of patches or strips of uniform stress. In the 3D model, these patches are applied centered around each SSI node, whereas in the 2.5D case the strips of uniform stress are applied centered around the element edge mid-point. In the 3D model, the contact pressure therefore extends slightly (by half an element width) outside the slab width. However, as seen from the response, these effects are negligible for the free-field response in the case studied here.

In terms of computational cost, it is difficult to make a completely fair comparison. For the two models using the LTM method to establish the soil impedance and response, the Green's function evaluation requires a loop over $N \times M$ wavenumbers in (k_1, k_2)-domain. In the 3D model, a large system of equations is established that is solved once for each excitation frequency. The dynamic stiffness matrix of the soil becomes fully populated. In the coupled 2.5D model a very small system of equations (corresponding to the DoFs of the 2D mesh) is solved, but on the other hand it is solved N times (once for every wavenumber k_1 in the x_1-direction). In the 2.5D FE–PML model, the system of equations is also solved N times, once for every wavenumber k_1. Here, the system of equations is considerably larger due to the discretization of the soil, and the computational time depends heavily on the size of the computational domain. To evaluate the response at large distances becomes costly because of the large soil domain requiring discretization. In all models, large savings in computational time can be gained by utilizing that the calculations are independent for each wavenumber k_1,

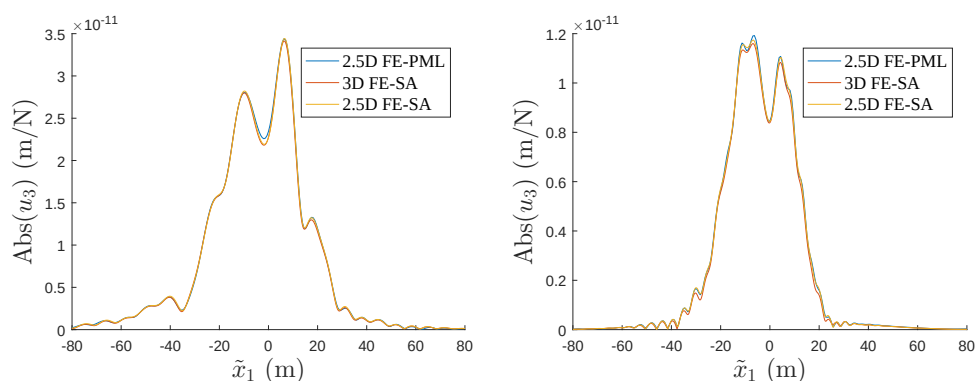

Figure 5.9: Maximum vertical displacement along a line 10 m from the track for the excitation frequencies $f = 40$ Hz (left) and $f = 80$ Hz (right).

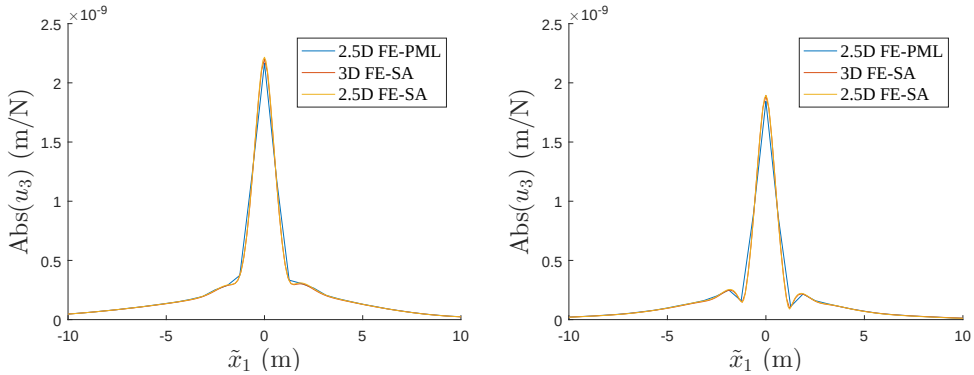

Figure 5.10: Maximum vertical displacement along the rail for a unit harmonic load with the excitation frequencies $f = 40$ Hz (left) and $f = 80$ Hz (right).

i.e. parallelization can be employed.

It can be argued that the 3D model does not have any advantages over the other two models in the case studied here, i.e. when considering a moving load. However, the model can of course also be used in a fixed frame of reference by setting the velocity $v = 0$. Then it is possible to introduce additional structures (e.g. a building with a surface footing) next to the track, e.g. to numerically predict transfer functions from the track to the building. This would not be possible in the two other models utilizing the 2.5D approach, where only long-stretched invariant structures could be included. In a 2.5D FE–PML model, as opposed to the other two models, it is straightforward to model e.g a long-stretched trench parallel with the track, or other discontinuities of the soil.

In the present example, the analysis of a unit harmonic load on the track was described. However, the results from such analyses can be utilized for studying the effect of a vehicle running over an uneven rail. For a given unevenness wavelength λ, the frequency of excitation by a wheel running at v is $f = v/\lambda$. The rail receptance (displacement per unit force) for a given frequency f and velocity v, can be used for establishing a sub-model where the vehicle response and the wheel–rail contact forces are calculated. The free-field response due to these contact forces are then obtained by scaling, phase-shifting and translating the free-field response calculated for the unit harmonic load. This is further detailed in Paper C. The total response from the dynamic excitation by a vehicle running over an uneven rail is obtained as the sum of contributions from discrete unevenness wavelengths. If measurements of the rail unevenness for a certain stretch are not available, rail unevenness defined in a statistical sense by a power spectral density (PSD) function can be used. Such a PSD function was used in Paper B for calculating the free-field response due to a 10 DoF train cart (see Figure 2.11) running on an uneven rail.

6 Summary of appended papers

6.1 PAPER A

Modeling train-induced ground-borne vibrations using FEM in a moving frame of reference.

J. Malmborg, K. Persson, P. Persson.

In proceedings of COMPDYN 2019, 7th International Conference on Computational Methods in Structural Dynamics and Earthquake Engineering, Crete, Greece, June 2019.

Summary

A numerical model for calculating the free-field ground vibrations from surface trains is presented in the paper. A finite element formulation in a frame of reference following the moving load at a fixed velocity, was used for modeling a railway slab track. The underlying soil was represented through a dynamic stiffness matrix, obtained from the Green's function for a horizontally layered visco-elastic half-space, in a moving frame of reference. Three different track models were established and compared. In two of the track models, the slab was represented by beam elements with different assumptions regarding the pressure distribution of the slab–soil interface. The third track model utilized plate elements for representing the slab, accounting for the cross-section flexibility and hence a more general slab–soil pressure distribution. The three track models were used for evaluating the free-field response due to a harmonic load in the frequency range 0–80 Hz moving along the track. One of the beam models, assuming a constant vertical displacement of the soil under the slab cross-section, showed good agreement with the plate model. The response obtained with the simplest beam model, assuming a constant contact pressure under the slab cross-section, was significantly underestimated.

6.2 PAPER B

Evaluating the effect of vibration isolation mats on train-induced ground vibrations.

J. Malmborg, K. Persson, P. Persson.

In proceedings of SEMC 2019, 7th International Conference on Structural Engineering, Mechanics and Computation, Cape Town, South Africa, September 2019.

Summary

The numerical modeling technique established in Paper B was applied to evaluate the effect of a vibration isolation mat, placed under a railway slab track, on the free-field ground vibrations. The slab and the underlying supporting plate were modeled using Kirchhoff plate elements, and the vibration isolation mat was modeled as a continuous visco-elastic layer between the two plates. First, the free-field response and the insertion loss obtained with the vibration isolation mat was calculated for a harmonic point load moving along the track. Secondly, band-averaged vibration levels and the insertion loss for a fixed point next to the track were calculated for a train cart, represented by a 10-DoF multi-body system, running at different speeds on an uneven track. The rail unevenness was described by a PSD function. It was found that the isolation mat changes the vibration response significantly in two ways. The introduction of a resilient element changes the transmissibility of the system, hence changing the vibration response due to a specific load acting on the track. Further, the resilient element modifies the track receptance, implying different dynamic wheel–rail interaction forces as the vehicle runs over the uneven rail. Negative insertion loss, i.e. a higher vibration response, were obtained for frequencies near the resonance frequency of the isolated slab, whereas a significant reduction of the response was obtained for higher frequencies.

6.3 PAPER C

Effects of modeling strategies for a slab track on predicted ground vibrations.

J. Malmborg, P. Persson, K. Persson.

Submitted for publication in international journal.

Summary

In the paper, the effect of modeling strategies regarding the dynamic behavior of a railway slab track on a layered half-space is studied. If the track is modeled as a layered beam, the free-field vibration response due to a moving harmonic load on the track can be evaluated efficiently using a semi-analytical procedure in frequency–wavenumber domain. However, such a beam representation of the track does not account for the cross-section flexibility, and some assumptions regarding the displacements or the stress-distribution in the track–soil interface have to be made. In the paper, a constant displacement and a constant stress-distribution, respectively, were tested. The free-field response obtained with the beam models were compared to that obtained using a solid finite element and a shell finite element representation of the slab, using the technique established in Paper A. First, only the vertical displacements of the slab–soil interface were coupled. Secondly, the effect of coupling the in-plane displacements on the free-field vibrations were studied. Furthermore, a sub-structuring technique was employed to calculate and compare the wheel–rail interaction forces with the different models, for a single-axle vehicle. It was found that for a thin slab, the vertical pressure distribution under the slab is highly influenced by the cross-section flexibility, which in turn significantly affects the predicted free-field vibrations. The two beam models yielded an underestimated response for the studied cases. For a thick slab, however, the beam model with a constant displacement under the slab yielded accurate free-field response, compared to the solid and shell models. It was also found that when the in-plane shear forces of the slab–soil interface was accounted for, increased vibration response levels in the free-field were generally obtained. A beam model, enforcing zero in-plane displacements in the lateral direction of the slab–soil interface, provided good accuracy for a thick slab. All models provided similar rail receptances and subsequently wheel–rail interaction forces.

7 Concluding remarks

7.1 CONCLUSIONS

In this thesis, numerical modeling strategies for predicting ground-borne vibrations from a surface railway track have been studied. Focus have been on the vibration transmission from the track to the free-field, and to a smaller extent on the actual load generation. An efficient semi-analytical approach for modeling the soil behavior, based on the Green's function for a horizontally layered half-space, has been combined with finite element modeling of the railway track, both in 3D and so called 2.5D. All computational code was written in FORTRAN by the author. The main contributions of the work presented in the thesis and the appended papers include

- A novel combination of the Green's function for a layered visco-elastic half-space with a 3D FE representation of a railway track, in the moving frame of reference (Paper A–C).
- A study of insertion loss by the introduction of a resilient mat under the track slab, obtained in a fixed point next to the track due to a passing train on an uneven track (Paper B).
- A study of the importance of the track modeling strategy, regarding the cross-section flexibility and the track–soil in-plane shear forces, on the free-field vibrations (Paper C).
- An efficient combination of a 2.5D FE representation of a railway track combined with a semi-analytical soil impedance for predicting the free-field ground vibrations, described in Chapter 5.

Furthermore, the response obtained with the combined FE and semi-analytical models have for a specific case been compared to a model where also the soil is modeled using finite elements. The models showed very good agreement.

7.2 FUTURE WORK

In the present work, focus has been on computational models for calculating the free-field response next to a surface railway track. A natural continuation is to study and develop strategies and models enabling the numerical prediction of vibrations inside buildings. Such strategies are highly relevant in a practical civil engineering context to enable accurate predictions and informed design decisions. Mapping the incident wave field, generated by a moving train, on to a building to predict the response inside the building is not a straightforward task.

Apart from developing numerical models for tracing the vibrations from the source to the final receiver in a deterministic manner, an important subject of research is the quantification of the uncertainties that are afflicting such predictions due to limited knowledge or modeling capacity regarding the governing parameters. This becomes increasingly important when predicting the response inside a building, because the number of uncertain parameters increases drastically. It would therefore be very useful if the uncertainties regarding some parameters could be maintained and propagated through the prediction model, to establish predictions in a statistical sense, e.g. by means of confidence intervals.

References

[1] Central Intelligence Agency (2020), *The World Factbook 2020*, `https://www.cia.gov/library/publications/resources/the-world-factbook/index.html`, [Online; accessed 13-February-2020].

[2] Hanson, C., Towers, D., Meister, L. (2006), *Transit Noise and Vibration Impact Assesment*, Tech. Rep. FTA-VA-90-1003-06, U.S. Department of Transportation, Federal Transit Admininistration, Office of Planning and Environment.

[3] Thompson, D., Kouroussis, G., Ntotsios, E. (2019), *Modelling, simulation and evaluation of ground vibration caused by rail vehicles*, Vehicle System Dynamics **57**(7), 936–983.

[4] Münzel, T., Schmidt, F., Steven, S., Herzog, J., Daiber, A., Sørensen, M. (2018), *Environmental noise and the cardiovascular system*, Journal of the American College of Cardiology **71**(6), 688–697.

[5] International Organization for Standardization, *Mechanical vibration and shock - Evaluation of human exposure to whole-body vibration - Part 1: General requirements*, Tech. Rep. ISO 2631-1:1997.

[6] Richart Jr, F., Hall Jr, J., Woods, R. (1970), *Vibrations of Soils and Foundations*, Prentice Hall, Englewood Cliffs, N.J.

[7] Kungl. Ingenjörsvetenskapsakademien (1979), *Jord- och bergmekanik. Information från IVA:s kommitte för vibrationsfrågor*, Tech. Rep. Meddelande 225.

[8] Kaynia, A., Madshus, P., Zackrisson, P. (2000), *Ground vibration from high-speed trains: prediction and countermeasure*, Journal of Geotechnical and Geoenvironmental Engineering **126**(6), 531–537.

[9] Chopra, A. (1995), *Dynamics of structures*, Prentice Hall, Upper Saddle River.

[10] Lombaert, G., Degrande, G., François, S., Thompson, D. (2013), *Ground-borne vibration due to railway traffic: a review of excitation mechanisms, prediction methods and mitigation measures*, in: *Proceedings of the 11th International Workshop on Railway Noise, Uddevalla, Sweden*.

[11] Nielsen, J., Igeland, A. (1995), *Vertical dynamic interaction between train and track - influence of wheel and track imperfections*, Journal of Sound and Vibration **187**(5), 825–839.

[12] Lei, X., Noda, N. (2002), *Analyses of dynamic response of vehicle and track coupling system with random irregularity of track vertical profile*, Journal of Sound and Vibration **258**(1), 147–165.

[13] Cantero, D., Arvidsson, T., OBrien, E., Karoumi, R. (2016), *Train–track–bridge modelling and review of parameters*, Structure and Infrastructure Engineering **12**(9), 1051–1064.

[14] Triepaischajonsak, N., Thompson, D. (2015), *A hybrid modelling approach for predicting ground vibration from trains*, Journal of Sound and Vibration **335**, 147–173.

[15] Lei, X., Wang, J. (2014), *Dynamic analysis of the train and slab track coupling system with finite elements in a moving frame of reference*, Journal of Vibration and Control **20**(9), 1301–1317.

[16] Aggestam, E., Nielsen, J., Bolmsvik, R. (2018), *Simulation of vertical dynamic vehicle-track interaction using a two-dimensional slab track model*, Vehicle System Dynamics **56**(11), 1633–1657.

[17] Aggestam, E., Nielsen, J. (2019), *Multi-objective optimisation of transition zones between slab track and ballasted track using a genetic algorithm*, Journal of Sound and Vibration **446**, 91–112.

[18] Nielsen, J., Lombaert, G., François, S. (2015), *A hybrid model for prediction of ground-borne vibration due to discrete wheel/rail irregularities*, Journal of Sound and Vibration **345**, 103–120.

[19] Koroma, S., Thompson, D., Hussein, M., Ntotsios, E. (2017), *A mixed space-time and wavenumber-frequency domain procedure for modelling ground vibration from surface railway tracks*, Journal of Sound and Vibration **400**, 508–532.

[20] Andersen, L., Nielsen, S., Kirkegaard, P. (2001), *Finite element modelling of infinite Euler beams on Kelvin foundations exposed to moving loads in convected co-ordinates*, Journal of Sound and Vibration **241**(4), 587–604.

[21] Andersen, L., Nielsen, S. (2003), *Vibrations of track caused by variation of the foundation stiffness*, Probabilistic Engineering Mechanics **18**(2), 171–184.

[22] Koh, C., Ong, J., Chua, D., Feng, J. (2003), *Moving element method for train-track dynamics*, Numerical Methods in Engineering **56**(11), 1549–1567.

[23] Germonpré, M., Nielsen, J., Degrande, G., Lombaert, G. (2018), *Contributions of longitudinal track unevenness and track stiffness variation to railway induced vibration*, Journal of Sound and Vibration **437**, 292–307.

[24] Lysmer, J., Kuhlemeyer, R. (1969), *Finite dynamic model for infinite media*, Journal of Engineering Mechanics (ASCE) 859–877.

[25] Basu, U., Chopra, A. (2003), *Perfectly matched layers for time-harmonic elastodynamics of unbounded domains: theory and finite-element implementation*, Computer Methods in Applied Mechanics and Engineering **192**(11-12), 1337–1375.

[26] Connolly, D., Giannopoulos, A., Forde, M. (2013), *Numerical modelling of ground borne vibrations from high speed rail lines on embankments*, Soil Dynamics and Earthquake Engineering **46**, 13–19.

[27] Kouroussis, G., Connolly, D., Alexandrou, G., Vogiatzis, K. (2015), *The effect of railway local irregularities on ground vibration*, Transportation Research Part D: Transport and Environment **39**, 17–30.

[28] Andersen, L., Nielsen, S. (2005), *Reduction of ground vibration by means of barriers or soil improvement along a railway track*, Soil Dynamics and Earthquake Engineering **25**, 701–716.

[29] Galvín, P., Romero, A., Domínguez, J. (2010), *Fully three-dimensional analysis of high-speed train-track-soil-structure dynamic interaction*, Journal of Sound and Vibration **329**(24), 5147–5163.

[30] Yang, Y., Hung, H. (2001), *A 2.5D finite-infinite element approach for modelling visco-elastic bodies subjected to moving loads*, International Journal for Numerical Methods in Engineering **51**, 1317–1336.

[31] Sheng, X., Jones, C., Thompson, D. (2006), *Prediction of ground vibration from trains using the wavenumber finite and boundary element methods*, Journal of Sound and Vibration **293**, 575–586.

[32] Alves Costa, P., Calçada, R., Silva Cardoso, A. (2012), *Track-ground vibrations induced by railway traffic: In-situ measurements and validation of a 2.5D FEM-BEM model*, Soil Dynamics and Earthquake Engineering **32**(1), 111–128.

[33] Galvín, P., François, S., Schevenels, M., Bongini, E., Degrande, G., Lombaert, G. (2010), *A 2.5D coupled FE-BE model for the prediction of railway induced vibrations*, Soil Dynamics and Earthquake Engineering **30**, 1500–1512.

[34] François, S., Schevenels, M., Galvín, P., Lombaert, G., Degrande, G. (2010), *A 2.5D coupled FE-BE methodology for the dynamic interaction between longitudinally invariant structures and a layered halfspace*, Computer Methods in Applied Mechanics and Engineering **199**(23-24), 1536–1548.

[35] Sheng, X., Jones, C., Petyt, M. (1999), *Ground vibration generated by a harmonic load acting on a railway track*, Journal of Sound and Vibration **225**(1), 3–28.

[36] Sheng, X., Jones, C., Petyt, M. (1999), *Ground vibration generated by a load moving along a railway track*, Journal of Sound and Vibration **228**(1), 129–156.

[37] Sheng, X., Jones, C., Thompson, D. (2004), *A theoretical model for ground vibration from trains generated by vertical track irregularities*, Journal of Sound and Vibration **272**, 937–965.

[38] Chahour, K., Lefeuve-Mesgouez, G., Mesgouez, A. (2014), *Spectral analysis of a railway track in contact with a multilayered poroviscoelastic soil subjected to a harmonic moving load*, Soil Dynamics and Earthquake Engineering **64**, 24–37.

[39] Clough, R., Penzien, J. (1993), *Dynamics of Structures*, McGraw-Hill College.

[40] Kramer, S. (1996), *Geotechnical Earthquake Engineering*, Prentice Hall.

[41] Sparr, G., Sparr, A. (1999), *Kontinuerliga system*, Studentlitteratur.

[42] Andersen, L. (2006), *Linear Elastodynamic Analysis*, Department of Civil Engineering, Aalborg University.

[43] Ottosen, N., Petersson, H. (1992), *Introduction to the finite element method*, Prentice Hall.

[44] François, S., Schevenels, M., Lombaert, G., Degrande, G. (2012), *A two-and-a-half dimensional displacement-based PML for elastodynamic wave propagation*, International Journal for Numerical Methods in Engineering **90**, 819–837.

[45] Andersen, L., Clausen, J. (2008), *Impedance of surface footings on layered ground*, Computers and Structures **86**, 72–87.

[46] Thomson, W. (1950), *Transmission of elastic waves through a stratified solid medium*, Journal of Applied Physics **21**, 89–93.

[47] Haskell, N. (1953), *The dispersion of surface waves on multilayered medium*, Bulletin of the Seismological Society of America **73**, 17–43.

[48] Wang, R. (1999), *A simple orthonormalization method for stable and efficient computation of Green's functions*, Bulletin of the Seismological Society of America **89**(3), 733–741.

[49] Intel (2016), *Intel Math Kernel Library 11.3, Reference Manual*.

Part II

Appended Publications

Paper A

COMPDYN 2019
7th ECCOMAS Thematic Conference on
Computational Methods in Structural Dynamics and Earthquake Engineering
M. Papadrakakis, M. Fragiadakis (eds.)
Crete, Greece, 24-26 June 2019

MODELING TRAIN-INDUCED GROUND-BORNE VIBRATIONS USING FEM IN A MOVING FRAME OF REFERENCE

J. Malmborg[1], **K. Persson**[1] **and P. Persson**[1]

[1]Lund University, Department of Construction Sciences
P.O. Box 118 SE-221 00 Lund, Sweden
e-mail: {jens.malmborg,kent.persson,peter.persson}@construction.lth.se

Keywords: Train-induced ground-vibration, moving frame of reference, Kirchhoff plate slab track.

Abstract. *To predict ground-borne vibration levels caused by railway traffic, models for estimating the load from the vibration source, as well as the vibration transmission through the ground, are needed. In the present paper, a finite element formulation in a frame of reference following the moving load, is used for modeling a railway slab track. The response of the underlying soil is represented through a dynamic stiffness matrix, obtained via the Green's function for a horizontally layered visco-elastic half-space in a moving frame of reference in the frequency–wavenumber domain. The track can be modeled as continuously connected beams, but the use of plate elements allows for more general stress and displacement distributions in the transverse direction of the slab to be resolved. Here, the free-field response due to a harmonic load moving along a slab track, is evaluated and compared using different modeling strategies for the slab.*

1 INTRODUCTION

To predict the level of ground-borne vibration caused by railway traffic, models are needed to estimate the load from the vibration source as well as the vibration transmission through the ground. A number of techniques have been developed in the past decades to study ground vibrations caused by a passing train, ranging from empirical methods to analytical and numerical schemes.

Numerical schemes are often based on either the finite element (FE) or the boundary element (BE) method or a combination thereof. The strength of these methods lies in their ability to model arbitrary geometries and discontinuities. The downside is the high computational cost. The computational cost can be reduced if the soil and track system is assumed to be invariant in the track direction, leading to so called 2.5D models [1, 2, 3, 4]. Further, if the soil stratification is assumed to consist of horizontally layered visco-elastic layers, a fundamental solution (Green's function) for the soil response can be found efficiently in frequency–wavenumber domain. Sheng et al [5, 6] proposed a semi-analytical model, with the track represented by an infinite layered beam resting on a layered ground, where both the ground and the beam is described in the frequency–wavenumber domain. Kaynia et al [7] coupled a series of FE beams, representing the railway track, to a dynamic stiffness matrix of the ground calculated from the Green's function of a layered half-space.

Modeling the track as a beam on a layered half-space is a common approach in the field of ground-borne vibrations due to railway traffic. This approach, however, constricts the track–soil interface stress distribution. Steenbergen et al [8] studied the influence of different interface conditions between a beam on a half-space, subjected to a dynamic moving load, on the free-field response, using a semi-analytical model in the frequency–wavenumber domain. Galvin et al [4] compared the free-field response of a high-speed train passage on a ballasted track on an embankment, calculated using a 2.5D continuum model, to a model with a beam representation of the track, finding large differences attributed to the rigid cross-section of the embankment in the beam model.

In the present paper, a FE model is used for representing a railway slab track. The response of the underlying soil is represented by a dynamic stiffness matrix obtained via the Green's function for a horizontally layered visco-elastic half-space. The model is formulated in a frame of reference following the moving load. The slab and rails can either be modeled as continuously connected beams or by using Kirchhoff plate elements for representing the track slab. Plate elements allow for more general stress and displacement distributions in the track transveral direction to be resolved. Here, the free-field response due to a harmonic load moving along the track at constant velocity, is calculated and compared using different modeling strategies for the track.

In Section 2 an overview of the model is given and the studied case is presented in Section 3. Finally, conclusions are given in Section 4.

2 CALCULATION MODEL

2.1 Overview

The slab track is shown principally in Figure 1. It consists of a supporting layer, a concrete slab, rails and rail pads. Full interaction is assumed between the slab and the supporting layer, so that a homogeneous section with equivalent mass and bending stiffness may be utilized in the calculations. This homogeneous section is simply referred to as the slab in the following.

Three models, model a)–c), with different assumptions regarding the slab and the slab–soil

interface conditions, are established:

a) The slab is modeled with Bernoulli-Euler beam elements. Displacement continuity of the beam and the soil is enforced only along the beam center line. A uniform stress distribution between the beam and the soil is assumed in the transverse direction of the slab.

b) The slab is modeled with Bernoulli-Euler beam elements. The slab–soil interface is assumed rigid in the transverse direction. This is enforced by coupling the beam kinematically to a number of soil DoFs in the transverse direction over the width of the slab.

c) The slab is modeled with Kirchhoff plate elements, allowing for a more general slab–soil interface stress and displacement distribution in the transverse direction of the slab than by the two other models.

In all three models, the rails are modeled as Bernoulli-Euler beams, connected to the slab via a continuous visco-elastic interface layer representing the rail pads. The loading is assumed identical on both rails, hence in model a) and b) the two rails are modeled as one. In model c) symmetry around the track center line is utilized so that only half the track is modeled. The track is coupled to a ground model, represented by a dynamic stiffness matrix. The dynamic stiffness matrix of the ground is derived from the Green's function for a horizontally layered visco-elastic half-space. Both the ground model and the FE model are expressed in a moving frame of reference, following the vehicle at a given speed v. The models a)–c) are shown schematically in Figure 2.

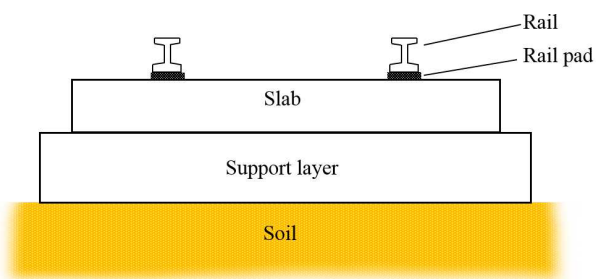

Figure 1: Section of slab track.

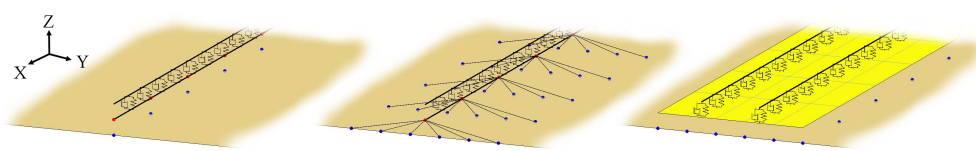

Figure 2: Finite element models of the slab track. From the left: Models a), b) and c). Blue points represent soil nodes at the slab–soil interface.

The soil model is described in Section 2.2. In Section 2.3 the governing equations for the beam, plate and interface finite elements are derived. The coupling between the finite elements and the soil is described in Section 2.4.

2.2 Soil model

The ground is assumed to be composed of horizontal visco-elastic layers. Neglecting body forces, the Navier equations for a single soil layer can be written as

$$(\lambda+\mu)\frac{\partial^2 u_j}{\partial x_i \partial x_j}+\mu\frac{\partial^2 u_i}{\partial x_j \partial x_j}=\rho\frac{\partial^2 u_i}{\partial t^2} \tag{1}$$

where $u_i = u_i(x_1, x_2, x_3, t)$ is the displacement in direction *i*. λ and μ are the Lame' parameters. Introducing a coordinate transformation as

$$(\tilde{x}_1, \tilde{x}_2, \tilde{x}_3) = (x_1 - vt, x_2, x_3), \tag{2}$$

where $\tilde{x}_1, \tilde{x}_2, \tilde{x}_3$ denotes the coordinates in the moving frame of reference, and v is the vehicle speed, transforms the Navier equations to

$$(\lambda+\mu)\frac{\partial^2 \tilde{u}_j}{\partial \tilde{x}_i \partial \tilde{x}_j}+\mu\frac{\partial^2 \tilde{u}_i}{\partial \tilde{x}_j \partial \tilde{x}_j}=\rho\Big(\frac{\partial^2 \tilde{u}_i}{\partial t^2}-2v\frac{\partial^2 \tilde{u}_i}{\partial t \partial \tilde{x}_1}+v^2\frac{\partial^2 \tilde{u}_i}{\partial^2 \tilde{x}_1}\Big), \tag{3}$$

where $\tilde{u}_i = \tilde{u}_i(\tilde{x}, \tilde{y}, \tilde{z}, t)$ is the displacement in the moving frame of reference [9].

Fourier transforming the Navier equations with respect to the horizontal coordinates and time, $(\tilde{x}_1, \tilde{x}_2, t)$, yields the Navier equations in frequency–wavenumber domain as

$$(\lambda+\mu)\tilde{\Delta} i\tilde{k}_1+\mu\Big(\frac{d^2}{d\tilde{x}_3^2}-\tilde{k}_1^2-\tilde{k}_2^2\Big)\tilde{U}_1=-\rho\tilde{\omega}^2\tilde{U}_1 \tag{4a}$$

$$(\lambda+\mu)\tilde{\Delta} i\tilde{k}_2+\mu\Big(\frac{d^2}{d\tilde{x}_3^2}-\tilde{k}_1^2-\tilde{k}_2^2\Big)\tilde{U}_2=-\rho\tilde{\omega}^2\tilde{U}_2 \tag{4b}$$

$$(\lambda+\mu)\frac{d\tilde{\Delta}}{d\tilde{x}_3}+\mu\Big(\frac{d^2}{d\tilde{x}_3^2}-\tilde{k}_1^2-\tilde{k}_2^2\Big)\tilde{U}_3=-\rho\tilde{\omega}^2\tilde{U}_3 \tag{4c}$$

where $\tilde{\Delta} = \tilde{\Delta}(\tilde{k}_1, \tilde{k}_2, \tilde{x}_3, \omega)$ is the Fourier transform, with respect to the horizontal coordinates and time, of the dilation $\Delta(\tilde{x}_1, \tilde{x}_2, \tilde{x}_3, t)$. The vibration frequency of a material point is $\tilde{\omega} = \omega - \tilde{k}_1 v$ and ω is the frequency of the moving load. The horizontal wavenumbers in the direction of $\tilde{x}_1$ and $\tilde{x}_2$ are $\tilde{k}_1$ and $\tilde{k}_2$, respecitvely.

As showed by Sheng [5, 6], the solution to Eq. 4 for an individual layer can be found analytically, and due to continuity of displacements and tractions over interfaces between layers, several layers can be assembled using the Thomson [10] and Haskell [11] layer transfer matrix approach, forming a relationship between the displacement and stresses at the top of the stratum and at the bottom of the stratum. With known boundary conditions at the lowest interface, a relationship between the traction and the displacement at the surface can be obtained as

$$\hat{\mathbf{u}} = \hat{\mathbf{G}}\,\hat{\mathbf{p}}, \tag{5}$$

where $\hat{\mathbf{u}} = \hat{\mathbf{u}}(\tilde{k}_1, \tilde{k}_2, \omega)$ and $\hat{\mathbf{p}} = \hat{\mathbf{p}}(\tilde{k}_1, \tilde{k}_2, \omega)$ are vectors containing the displacements and tractions respectively on the soil surface, $\hat{\mathbf{G}} = \hat{\mathbf{G}}(\tilde{k}_1, \tilde{k}_2, \omega)$ is the Green's function tensor, $\tilde{k}_1$ and $\tilde{k}_2$ are the horizontal wavenumbers. For certain frequencies and stratifications, the original Thomson and Haskell method suffers from loss-of-precision. To avoid these problems in the present work, the different soil layers are assembled in an orthonormalization procedure as proposed by Wang [12].

Equation 5 is evaluated for a set of discrete values of $\tilde{k}_1$ and $\tilde{k}_2$, and the displacement vector $\tilde{\mathbf{u}}(\tilde{x}_1, \tilde{x}_2, \omega)$ is obtained in Cartesian space through a double inverse Fourier transform of $\hat{\mathbf{u}}(\tilde{k}_1, \tilde{k}_2, \omega)$.

The procedure described above is used for calculating the response on the soil surface, due to a unit load with a rectangular spatial distribution, the size of which is determined by the element size in the connecting superstructure. From this single load case, a dynamic flexibility matrix $\mathbf{F}_g(\omega, v)$ is established for a set of DoFs where the superstructure interacts with the soil surface. These DoFs will be referred to as soil–structure interaction (SSI) DoFs. $\mathbf{F}_g$ is formed, column by column, by interpolating from $\tilde{\mathbf{u}}$. The flexibility matrix is then inverted to form the dynamic stiffness matrix of the soil, $\mathbf{D}_g(\omega, v) = \mathbf{F}_g^{-1}(\omega, v)$, which gives a relation between the steady-state displacements $\tilde{\mathbf{u}}_g$ and forces $\tilde{\mathbf{f}}_g$ for the SSI DoFs, at a certain load circular frequency ω and velocity v, as

$$\mathbf{D}_g \, \tilde{\mathbf{u}}_g = \tilde{\mathbf{f}}_g. \tag{6}$$

2.3 Finite element model of railway structure

The coordinate transformation used for expressing the governing FE equations in a moving frame of reference introduces convective terms in the damping and stiffness matrices. In Sections 2.3.1–2.3.3 below, the FE equations are derived for the beams, plates and visco-elastic interface elements, respectively.

2.3.1 Beam elements

The equilibrium equation for a Bernoulli-Euler beam reads

$$\frac{\partial^2 M}{\partial x^2} + q - m_b \frac{\partial^2 w}{\partial t^2} = 0, \tag{7}$$

where $M = M(x,t)$ is the bending moment. $q(x,t)$ is a loading force per unit length. m_b is the mass per unit length of the beam. $w = w(x,t)$ is the deflection. With the coordinate transformation described by Eq. 2, Eq. 7 can be written as

$$\frac{\partial^2 \tilde{M}}{\partial \tilde{x}^2} + \tilde{q} - m_b\left(\frac{\partial^2 \tilde{w}}{\partial t^2} - 2v\frac{\partial^2 \tilde{w}}{\partial \tilde{x} \partial t} + v^2 \frac{\partial^2 \tilde{w}}{\partial \tilde{x}^2}\right) = 0, \tag{8}$$

where $\tilde{\cdot}$ denotes that a variable is expressed in the moving frame of reference. The weak form is obtained by multiplying Eq. 8 by an arbitrary weight function $g = g(\tilde{x})$ and integrating it over the region. It can be shown that the resulting weak form for the Bernoulli-Euler beam in a moving frame of reference is

$$\int_a^b \tfrac{\partial^2 g}{\partial \tilde{x}^2} \tilde{M} \, dx - [\tfrac{\partial g}{\partial \tilde{x}} \tilde{M}]_a^b + [g\tilde{V}]_a^b + \int_a^b g\tilde{q} \, dx - m_b \int_a^b g(\tfrac{\partial^2 \tilde{w}}{\partial t^2} - 2v\tfrac{\partial^2 \tilde{w}}{\partial \tilde{x} \partial t} + v^2 \tfrac{\partial^2 \tilde{w}}{\partial \tilde{x}^2}) \, dx = 0. \tag{9}$$

With the kinematic and constitutive assumptions for a Bernoulli-Euler beam, $\tilde{M}$ can be written as

$$\tilde{M} = -EI \frac{\partial^2 \tilde{w}}{\partial \tilde{x}^2}, \tag{10}$$

where EI is the bending stiffness. To obtain the FE formulation, the deflection $\tilde{w}(\tilde{x}, t)$ is approximated using the element nodal values $\mathbf{a}(t)$ and the shape functions $\mathbf{N}(\tilde{x})$, as $\tilde{w} = \mathbf{N}\mathbf{a}$.

Adopting the Galerking method, the mass, damping and stiffness matrices, as well as the load and boundary vectors, are identified as

$$\mathbf{K} = EI \int_a^b \Big(\frac{d^2\mathbf{N}(\tilde{x})}{d\tilde{x}^2}\Big)^T \frac{d^2\mathbf{N}(\tilde{x})}{d\tilde{x}^2}\, dx + m_b\, v^2 \int_a^b \mathbf{N}^T \frac{d^2\mathbf{N}}{d\tilde{x}^2}\, dx, \tag{11}$$

$$\mathbf{C} = -2m_b v \int_a^b \mathbf{N}^T \frac{d\mathbf{N}}{d\tilde{x}}\, dx, \tag{12}$$

$$\mathbf{M} = m_b \int_a^b \mathbf{N}^T\mathbf{N}\, dx, \tag{13}$$

$$\mathbf{f}_l = \int_a^b \mathbf{N}^T \tilde{q}\, dx, \tag{14}$$

$$\mathbf{f}_b = [\mathbf{N}^T\tilde{V}]_a^b - [\frac{\partial \mathbf{N}^T}{\partial \tilde{x}}\tilde{M}]_a^b. \tag{15}$$

A 2-node beam element with two DoFs per node (vertical displacement and one rotation), based on the above formulation, is implemented and used in the present work. Similar derivations for the convective Bernoulli-Euler beams can be found in e.g. [13, 14].

2.3.2 Plate elements

The equilibrium equation for a Kirchhoff plate reads, see e.g. [15],

$$\frac{\partial^2 M_{xx}}{\partial x^2} + 2\frac{\partial^2 M_{xy}}{\partial x \partial y} + \frac{\partial^2 M_{yy}}{\partial y^2} + q - \rho h \frac{\partial^2 w}{\partial t^2} = 0, \tag{16}$$

where $M_{xx} = M_{xx}(x,y,t)$, $M_{yy} = M_{yy}(x,y,t)$ and $M_{xy} = M_{xy}(x,y,t)$ are the bending moments in the x- and y-directions. $q(x,y,t)$ is a loading force per unit area. h and ρ is the plate thickness and the mass density respectively. $w = w(x,y,t)$ is the deflection of the mid-section. With the coordinate transformation described by Eq. 2, Eq. 16 can be written as

$$\frac{\partial^2 \tilde{M}_{xx}}{\partial \tilde{x}^2} + 2\frac{\partial^2 \tilde{M}_{xy}}{\partial \tilde{x}\partial \tilde{y}} + \frac{\partial^2 \tilde{M}_{yy}}{\partial \tilde{y}^2} + \tilde{q} - \rho h(\frac{\partial^2 \tilde{w}}{\partial t^2} - 2v\frac{\partial^2 \tilde{w}}{\partial \tilde{x}\partial t} + v^2\frac{\partial^2 \tilde{w}}{\partial \tilde{x}^2}) = 0. \tag{17}$$

The weak form is obtained by multiplying Eq. 17 by an arbitrary weight function $g = g(\tilde{x},\tilde{y})$ and integrating it over the region. It can be shown that the resulting weak form for the Kirchhoff plate in a moving frame of reference is

$$\begin{array}{l} \int_A (\tilde{\nabla} g)^T \tilde{\mathbf{M}}\, dA - \oint_{\mathscr{L}} \frac{dg}{dn}\tilde{M}_{nn}\, d\mathscr{L} + \oint_{\mathscr{L}} g(\tilde{V}_{nz} + \frac{d\tilde{M}_{nm}}{dm})\, d\mathscr{L} + \int_A g\tilde{q}\, dA \\ -\rho h \int_A (g\frac{\partial^2 \tilde{w}}{\partial t^2} - 2vg\frac{\partial^2 \tilde{w}}{\partial \tilde{x}\partial t} + v^2 g\frac{\partial^2 \tilde{w}}{\partial \tilde{x}^2})\, dA = 0, \end{array} \tag{18}$$

where the matrix differential operator $\tilde{\nabla}$ is defined as

$$\tilde{\nabla} = \begin{bmatrix} \frac{\partial^2}{d\tilde{x}^2} & \frac{\partial^2}{d\tilde{y}^2} & 2\frac{\partial^2}{d\tilde{x}d\tilde{y}} \end{bmatrix}^T, \tag{19}$$

and the moment vector $\tilde{\mathbf{M}}$ as

$$\tilde{\mathbf{M}} = \tilde{\mathbf{M}}(\tilde{x},\tilde{y},t) = \begin{bmatrix} \tilde{M}_{xx}(x,y,t) & \tilde{M}_{yy}(x,y,t) & \tilde{M}_{xy}(x,y,t) \end{bmatrix}^T. \tag{20}$$

The constitutive equation for the cross-section of a Kirchhoff plate can be written as $\tilde{\mathbf{M}} = -(h^3/12)\mathbf{D}\tilde{\nabla}\tilde{w}$ where $\mathbf{D}$ is the plane stress constitutive matrix for isotropic elasticity. To obtain the FE formulation, the deflection $\tilde{w}(\tilde{x},\tilde{y},t)$ is approximated using the element nodal values $\mathbf{a}(t)$ and the shape functions $\mathbf{N}(\tilde{x},\tilde{y})$, as $\tilde{w} = \mathbf{N}\mathbf{a}$.

Adopting the Galerking method, the mass, damping and stiffness matrices, as well as the load and boundary vectors, are identified as

$$\mathbf{K} = \frac{h^3}{12}\int_A (\tilde{\nabla}\mathbf{N})^T\mathbf{D}(\tilde{\nabla}\mathbf{N})\,dA \;+\rho h v^2\int_A \mathbf{N}^T\frac{\partial^2\mathbf{N}}{\partial\tilde{x}^2}\,dA\,, \tag{21}$$

$$\mathbf{C} = -2\rho h v\int_A \mathbf{N}^T\frac{\partial\mathbf{N}}{\partial\tilde{x}}\,dA, \tag{22}$$

$$\mathbf{M} = \rho h\int_A \mathbf{N}^T\mathbf{N}\,dA, \tag{23}$$

$$\mathbf{f}_l = \int_A \mathbf{N}^T\tilde{q}\,dA, \tag{24}$$

$$\mathbf{f}_b = \oint_{\mathscr{L}} \mathbf{N}^T(\tilde{V}_{nz} + \frac{d\tilde{M}_{nm}}{dm})\,d\mathscr{L} - \oint_{\mathscr{L}} (\nabla\mathbf{N})^T\mathbf{n}\tilde{M}_{nn}\,d\mathscr{L}. \tag{25}$$

A 4-node rectangular element with three DoFs per node (vertical displacement and two rotations), based on the above formulation, is implemented and used in the present work.

2.3.3 Visco-elastic interface elements

The rail pads are modeled by visco-elastic interface elements, representing continuous springs and dashpots. In the following derivation of the equations for the interface elements, an interface element is assumed to be located between two beam elements parallel with the x-axis. The loads on the upper and lower beams due to the visco-elastic interface are written

$$q_u(x,y,t) = -k(w_u - w_l) - c(\frac{\partial w_u}{\partial t} - \frac{\partial w_l}{\partial t}) = 0, \tag{26}$$

$$q_l(x,y,t) = -k(w_l - w_u) - c(\frac{\partial w_l}{\partial t} - \frac{\partial w_u}{\partial t}) = 0, \tag{27}$$

where $w_u = w_u(x,t)$ and $w_l = w_l(x,t)$ is the deflection in the upper and lower beam respectively, k is the spring stiffness and c is the damping coefficient. With the coordinate transformation described by Eq. 2,

$$\tilde{q}_u(\tilde{x},t) = -k(\tilde{w}_u - \tilde{w}_l) - c\Big\{(\frac{\partial\tilde{w}_u}{\partial t} - \frac{\partial\tilde{w}_l}{\partial t}) - v(\frac{\partial\tilde{w}_u}{\partial\tilde{x}} - \frac{\partial\tilde{w}_l}{\partial\tilde{x}})\Big\}, \tag{28}$$

$$\tilde{q}_l(\tilde{x},t) = -k(\tilde{w}_l - \tilde{w}_u) - c\Big\{(\frac{\partial\tilde{w}_l}{\partial t} - \frac{\partial\tilde{w}_u}{\partial t}) - v(\frac{\partial\tilde{w}_l}{\partial\tilde{x}} - \frac{\partial\tilde{w}_u}{\partial\tilde{x}})\Big\}. \tag{29}$$

The displacements of the upper and lower beam, w_u and w_l, are approximated using the shape functions $\mathbf{N}_u$ and $\mathbf{N}_l$ and element nodal displacements $\mathbf{a}_u(t)$ and $\mathbf{a}_l(t)$ for the upper and lower beams, respectively. With Eq. 14 the load vectors for the respective beams can be written

$$\begin{aligned}&\mathbf{f}_{l_u} = \textstyle\int_a^b \mathbf{N}_u^T\tilde{q}_u\,dx = -k\Big\{\int_a^b \mathbf{N}_u^T\mathbf{N}_u\,dx\,\mathbf{a}_u - \int_a^b \mathbf{N}_u^T\mathbf{N}_l\,dx\,\mathbf{a}_l\Big\} - \\ &c\Big\{\int_a^b \mathbf{N}_u^T\mathbf{N}_u\,dx\,\dot{\mathbf{a}}_u + \int_a^b \mathbf{N}_u^T\mathbf{N}_l\,dx\,\dot{\mathbf{a}}_l\Big\} + c\,v\,\Big\{\int_a^b \mathbf{N}_u^T\tfrac{\partial\mathbf{N}_u}{\partial\tilde{x}}\,dx\,\mathbf{a}_u - \int_a^b \mathbf{N}_u^T\tfrac{\partial\mathbf{N}_l}{\partial\tilde{x}}\,dx\,\mathbf{a}_l\Big\},\end{aligned} \tag{30}$$

$$\begin{aligned}&\mathbf{f}_{l_l} = \int_a^b \mathbf{N}_l^T \tilde{q}_l \, dx = -k\Big\{ \int_a^b \mathbf{N}_l^T \mathbf{N}_l \, dx \, \mathbf{a}_l - \int_a^b \mathbf{N}_l^T \mathbf{N}_u \, dx \, \mathbf{a}_u \Big\} - \\ &c\Big\{ \int_a^b \mathbf{N}_l^T \mathbf{N}_l \, dx \, \dot{\mathbf{a}}_l + \int_a^b \mathbf{N}_l^T \mathbf{N}_u \, dx \, \dot{\mathbf{a}}_u \Big\} + c\,v \Big\{ \int_a^b \mathbf{N}_l^T \tfrac{\partial \mathbf{N}_l}{\partial \tilde{x}} \, dx \, \mathbf{a}_l - \int_a^b \mathbf{N}_l^T \tfrac{\partial \mathbf{N}_u}{\partial \tilde{x}} \, dx \, \mathbf{a}_u \Big\}.\end{aligned} \tag{31}$$

With the shape function vectors $\tilde{\mathbf{N}}_u$ and $\tilde{\mathbf{N}}_l$ and the displacement vector $\mathbf{a}$ defined as

$$\begin{aligned}&\tilde{\mathbf{N}}_u(\tilde{x},\tilde{y}) = \begin{bmatrix}\mathbf{N}_u & 0\mathbf{N}_l\end{bmatrix}, \tilde{\mathbf{N}}_l(\tilde{x},\tilde{y}) = \begin{bmatrix}0\mathbf{N}_u & \mathbf{N}_l\end{bmatrix} \\ &\tilde{\mathbf{f}}_{l_u}(t) = \begin{bmatrix}\mathbf{f}_{l_u} & 0\mathbf{f}_{l_l}\end{bmatrix}, \tilde{\mathbf{f}}_{l_l}(t) = \begin{bmatrix}0\mathbf{f}_{l_u} & \mathbf{f}_{l_l}\end{bmatrix}, \mathbf{f}_L(t) = \begin{bmatrix}\mathbf{f}_{l_u} & \mathbf{f}_{l_l}\end{bmatrix}^T \\ &\tilde{\mathbf{a}}_u(t) = \begin{bmatrix}\mathbf{a}_u & 0\mathbf{a}_l\end{bmatrix}, \tilde{\mathbf{a}}_l(t) = \begin{bmatrix}0\mathbf{a}_u & \mathbf{a}_l\end{bmatrix}, \mathbf{a}(t) = \begin{bmatrix}\mathbf{a}_u & \mathbf{a}_l\end{bmatrix}^T\end{aligned} \tag{32}$$

it is possible to write the load vector as

$$\begin{aligned}&\mathbf{f}_L(t) = \tilde{\mathbf{f}}_{l_u}(t) + \tilde{\mathbf{f}}_{l_l}(t) = \\ &-k\Big\{ \int_a^b \tilde{\mathbf{N}}_u^T \tilde{\mathbf{N}}_u \, dx + \int_a^b \tilde{\mathbf{N}}_l^T \tilde{\mathbf{N}}_l \, dx - \int_a^b \tilde{\mathbf{N}}_u^T \tilde{\mathbf{N}}_l \, dx - \int_a^b \tilde{\mathbf{N}}_l^T \tilde{\mathbf{N}}_u \, dx \Big\} \mathbf{a} \\ &-c\Big\{ \int_a^b \tilde{\mathbf{N}}_u^T \tilde{\mathbf{N}}_u \, dx + \int_a^b \tilde{\mathbf{N}}_l^T \tilde{\mathbf{N}}_l \, dx + \int_a^b \tilde{\mathbf{N}}_u^T \tilde{\mathbf{N}}_l \, dx + \int_a^b \tilde{\mathbf{N}}_l^T \tilde{\mathbf{N}}_u \, dx \Big\} \dot{\mathbf{a}} \\ &+c\,v \Big\{ \int_a^b \tilde{\mathbf{N}}_u^T \tfrac{\partial \tilde{\mathbf{N}}_u}{\partial \tilde{x}} \, dx + \int_a^b \tilde{\mathbf{N}}_l^T \tfrac{\partial \tilde{\mathbf{N}}_l}{\partial \tilde{x}} \, dx - \int_a^b \tilde{\mathbf{N}}_u^T \tfrac{\partial \tilde{\mathbf{N}}_l}{\partial \tilde{x}} \, dx - \int_a^b \tilde{\mathbf{N}}_l^T \tfrac{\partial \tilde{\mathbf{N}}_u}{\partial \tilde{x}} \, dx \Big\} \mathbf{a}.\end{aligned} \tag{33}$$

The vector $\mathbf{f}_L(t)$ collects the forces on the upper and lower beam, caused by the interface element. The forces on the interface element are therefore $\mathbf{f}_i(t) = -\mathbf{f}_L(t)$, and the stiffness and damping matrices of the interface element can be identified from Eq. 33 as

$$\begin{aligned}&\mathbf{K} = k\Big\{ \int_a^b \tilde{\mathbf{N}}_u^T \tilde{\mathbf{N}}_u \, dx + \int_a^b \tilde{\mathbf{N}}_l^T \tilde{\mathbf{N}}_l \, dx - \int_a^b \tilde{\mathbf{N}}_u^T \tilde{\mathbf{N}}_l \, dx - \int_a^b \tilde{\mathbf{N}}_l^T \tilde{\mathbf{N}}_u \, dx \Big\} \\ &-cv\Big\{ \int_a^b \tilde{\mathbf{N}}_u^T \tfrac{\partial \tilde{\mathbf{N}}_u}{\partial \tilde{x}} \, dx + \int_a^b \tilde{\mathbf{N}}_l^T \tfrac{\partial \tilde{\mathbf{N}}_l}{\partial \tilde{x}} \, dx - \int_a^b \tilde{\mathbf{N}}_u^T \tfrac{\partial \tilde{\mathbf{N}}_l}{\partial \tilde{x}} \, dx - \int_a^b \tilde{\mathbf{N}}_l^T \tfrac{\partial \tilde{\mathbf{N}}_u}{\partial \tilde{x}} \, dx \Big\},\end{aligned} \tag{34}$$

$$\mathbf{C} = c\Big\{ \int_a^b \tilde{\mathbf{N}}_u^T \tilde{\mathbf{N}}_u \, dx + \int_a^b \tilde{\mathbf{N}}_l^T \tilde{\mathbf{N}}_l \, dx - \int_a^b \tilde{\mathbf{N}}_u^T \tilde{\mathbf{N}}_l \, dx - \int_a^b \tilde{\mathbf{N}}_l^T \tilde{\mathbf{N}}_u \, dx \Big\}. \tag{35}$$

The above expressions are also valid for an interface element between a beam element overlying a plate element in the xy-plane, such as in model c), with the shape functions for the plate evaluated at the y-coordinate of the beam.

2.4 Coupling to soil

Assuming steady-state conditions, the governing equation for the railway track structure can be written as

$$(-\omega^2 \mathbf{M}_r + i\omega \mathbf{C}_r + \mathbf{K}_r)\tilde{\mathbf{u}}_r = \tilde{\mathbf{f}}_r, \tag{36}$$

or

$$\mathbf{D}_r \tilde{\mathbf{u}}_r = \tilde{\mathbf{f}}_r, \tag{37}$$

where $\mathbf{M}_r$, $\mathbf{C}_r$ and $\mathbf{K}_r$ is the mass, damping and stiffness matrix respectively. $\mathbf{D}_r = (-\omega^2 \mathbf{M}_r + i\omega \mathbf{C}_r + \mathbf{K}_r)$ is the dynamic stiffness matrix, and $\tilde{\mathbf{u}}_r$ and $\tilde{\mathbf{f}}_r$ is the displacement and force vector for the track structure, respectively.

The track and soil is coupled in a standard FE manner. Only the vertical DoFs of the track structure and the soil are coupled. A global system of equations for the soil and the railway structure is formed by combining Eqs. 6 and 37, yielding

$$\mathbf{D}_t \tilde{\mathbf{u}}_r = \tilde{\mathbf{f}}_r, \tag{38}$$

where $\mathbf{D}_t$ represents the total dynamic stiffness matrix for the track structure and soil.

Once the track displacements $\tilde{\mathbf{u}}_r$, and thereby also the displacement in the soil DoFs $\tilde{\mathbf{u}}_g$, have been obtained by solving Eq. 38, the corresponding forces on the soil surface, $\tilde{\mathbf{f}}_g$ are calculated by Eq. 6. A second flexibility matrix $\mathbf{F}_{gf}(\omega, v)$ is established, in the same manner as $\mathbf{F}_g(\omega, v)$ as described in Section 2.2, expressing the displacements in free-field due to forces on the soil–structure interface. The free-field displacements, $\tilde{\mathbf{u}}_f$, are then calculated as

$$\tilde{\mathbf{u}}_f = \mathbf{F}_{gf}\tilde{\mathbf{f}}_g. \tag{39}$$

3 MODEL COMPARISON

To compare the effect of the three different modeling strategies for the track on the free-field response, each model is used for evaluating the response to a moving unit harmonic point load acting on the rail. The track properties are given in Table 1. The track rests on a 14 m deep layer of clay overlaying a half-space, with properties according to Table 2. An element length of 0.3 m is used, meaning that 12 elements are used in the transverse direction of the slab in model c). For model b) the slab is rigidly connected to 13 soil DoFs in the transverse direction. In all three models, the number of elements in the track direction is 500, yielding a total track length of 150 meters, which has been found to be sufficient to avoid problems with reflecting waves at the boundaries of the FE model in the studied case. The track gauge is 1.435 m.

Figure 3 shows the wavefield and the track deformation due to a harmonic point load with frequency $f = 50$ Hz traveling at $v = 60$ m/s, as obtained with the three different models. The difference in the slab deformation in the transverse direction due to the different modeling approaches is clearly visible. The displacements shown in Figure 3 are in the moving frame of reference, following the load at speed $v = 60$ m/s. In this frame of reference, the displacements are in steady state with the loading frequency $f = 50$ Hz. For a fixed point in the free-field, however, the response is transient and contains a broad band of frequencies due to the Doppler effect. A higher load speed results in a broader frequency content of the response in a fixed point. This can be seen in Figure 4 that shows the displacement spectrum for a fixed point 10 m and 25 m from the track, due to a harmonic 50 Hz load travelling at $v = 30$ m/s and $v = 60$ m/s. All three models yield similar results, however, the response obtained with model c) using plate elements is slightly higher than obtained with the other two models, for this particular load frequency.

To compare the three models for a range of excitation frequencies, a moving rms-value of the vibration velocity in a fixed point is calculated for each excitation frequency f, as

$$v_{rms}(t) = \sqrt{\frac{1}{T}\int_t^{t+T} \dot{u}(t)^2 dt}, \tag{40}$$

where $\dot{u}(t)$ is the velocity time history response for a fixed point. T is the window length and is here set to $T = 1$ s. In Figure 5 the maximum of $v_{rms}(t)$ is shown for each excitation frequency for the three models, for a fixed point located 10 and 25 m from the track respectively and the load speeds $v = 30$ and $v = 60$ m/s. For both load speeds, and both distances, the free-field response is very similar for all three models up to about $f = 50$ Hz. At higher frequencies, both models a) and b) underestimate the response. However, the underestimation with model b) is modest. For model a) the maximum underestimation is almost 10 dB at 70 Hz.

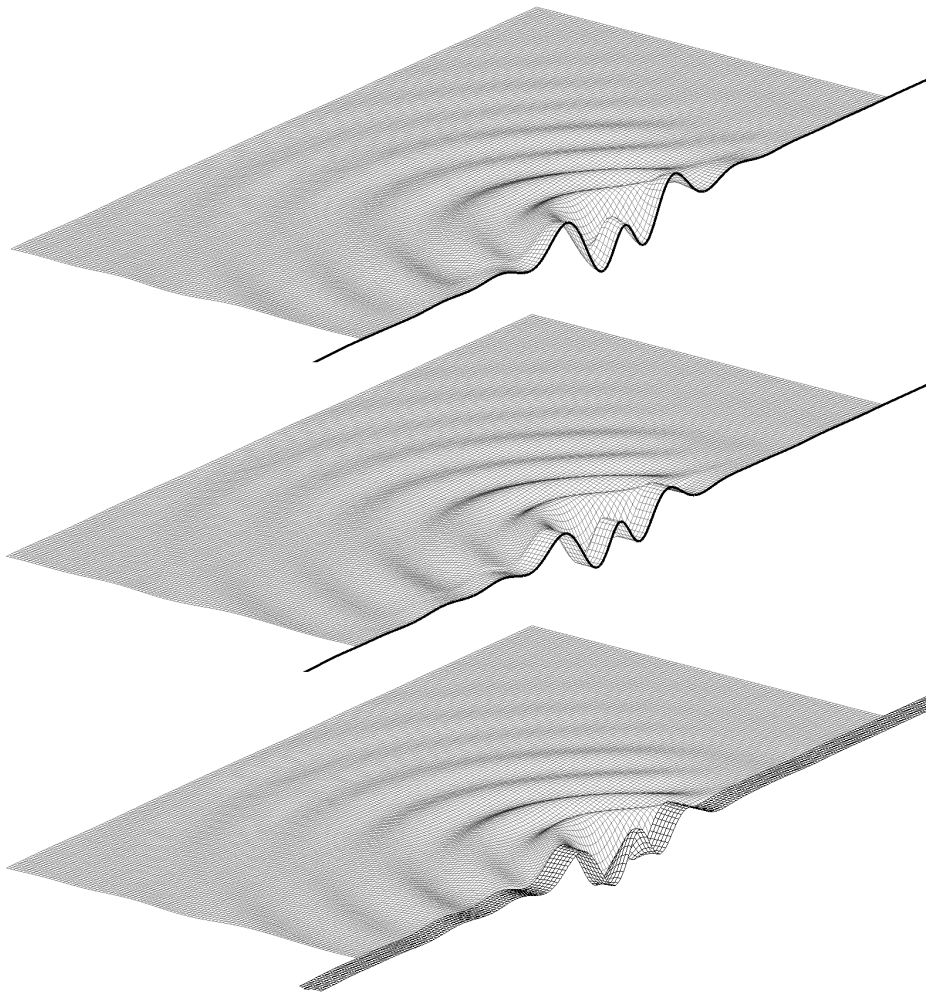

Figure 3: Soil and slab displacements in models a)–c), from top to bottom, when subjected to a harmonic load with frequency $f = 50$ Hz moving along the track at speed $v = 60$ m/s. The size of the displayed area is 60 m$\times$ 30 m.

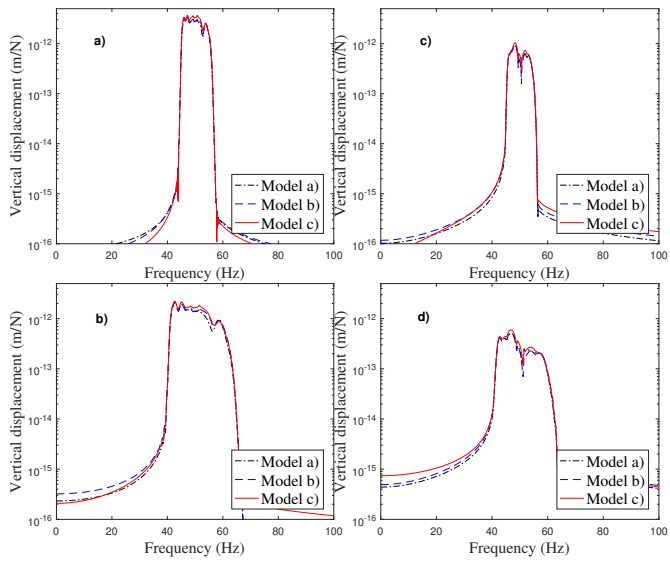

Figure 4: Response of a fixed point in the free-field due to a 50 Hz load traveling on the track. a) and b) show the results for a fixed point 10 meters from the track, with a load speed of $v = 30$ and $v = 60$ m/s, respectively. c) and d) are for a point 25 meters from the track.

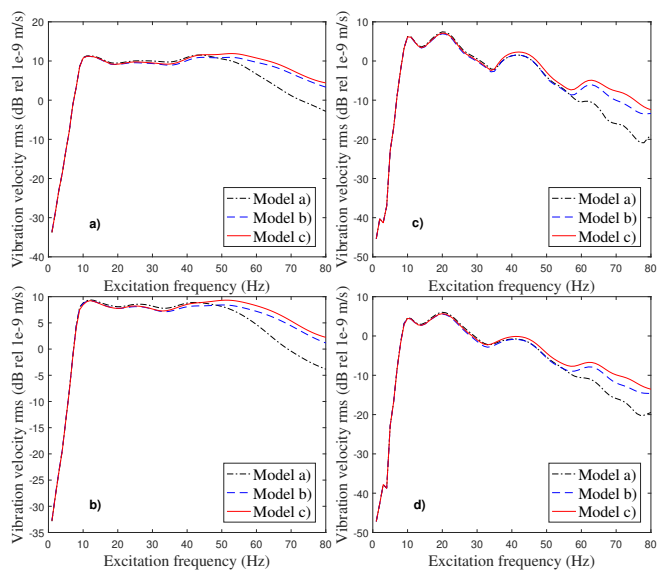

Figure 5: Velocity rms-value of a fixed point in the free-field due to a harmonic load traveling on the track. a) and b) show the results for a fixed point 10 meters from the track, with a load speed of $v = 30$ and $v = 60$ m/s, respectively. c) and d) are for a point 25 meters from the track.

	Parameter	Value
Rail	Mass (kg/m)	60
	Young's modulus (GPa)	210
	Second moment of inertia (m^4)	3.217×10^{-5}
	Loss factor (-)	0.01
Rail pads	Stiffness (MN/m^2)	92
	Damping (kNs/m^2)	73
Slab + support layer	Density (kg/m^3)	2310
	Young's modulus (GPa)	26.7
	Poisson's ratio	0.2
	Width (m)	3.6
	Thickness (m)	0.55
	Loss factor (-)	0.04

Table 1: Track properties.

4 CONCLUSIONS

In the paper a numerical prediction model for train-induced ground-vibration has been presented. The model is formulated in a frame of reference following the moving load, which offers some advantages over conventional FE models using a fixed frame of reference. Using a fixed frame of reference, the computational domain must be large for the moving load to stay within the model during the time of analysis. In the moving frame of reference following the load, on the other hand, the load stays at the same location in the model throughout the analysis, allowing a smaller model. Furthermore, frequency domain methods can be used for analyzing the moving load. A drawback of the model is that it is not suitable for analyzing load cases where the resulting wavelengths are very short, such as moving loads approaching the soil shear wave velocity. Short wavelengths, making the current approach inappropriate, may also result from non-moving loads, depending on the soil and track stiffness and the frequency of the load.

Three different models of a railway slab track have been established and compared. In the first two models, the railway track is modeled as a Bernoulli-Euler beam on a layered half-space, with different assumptions regarding the displacement and stress distribution at the track–soil interface. In the third model, the track slab is modeled using Kirchhoff plate elements, enabling a more general displacement and stress distribution in the track transverse direction to be resolved. It is shown that in the case studied here, the beam model where the track–soil interface is considered rigid over the width of the slab, only slightly underestimates the response, at higher frequencies. The beam model where a uniform traction is assumed at the track–soil interface, on the other hand, underestimates the response significantly at frequencies above 50 Hz.

5 Acknowledgments

Part of the project was funded by the City of Helsingborg through the call Plattformen. The authors of this work gratefully acknowledge the financial support.

Layer	Parameter	Value
Soil	Depth (m)	14.0
	Young's modulus (MPa)	475
	Poisson's ratio	0.48
	Density (kg/m^3)	2125
	Loss factor (-)	0.14
Bedrock	Depth (m)	∞
(half-space)	Young's modulus (MPa)	8800
	Poisson's ratio	0.40
	Density (kg/m^3)	2600
	Loss factor (-)	0.04

Table 2: Soil properties.

REFERENCES

[1] Y. Yang, H. Hung, A 2.5D finite-infinite element approach for modelling visco-elastic bodies subjected to moving loads. *International Journal for Numerical Methods in Engineering*, **51**. 1317–1336, 2008.

[2] X. Sheng, C.J.C. Jones, D.J. Thompson, Prediction of ground vibration from trains using the wavenumber finite and boundary element methods. *Journal of Sound and Vibration*, **293**. 575–586, 2006.

[3] G. Lombaert, G. Degrande, J. Kogut, S. Francois, The experimental validation of a numerical model for the prediction of railway induced vibrations. *Journal of Sound and Vibration*, **297**. 512–535, 2006.

[4] P. Galvin, S. Francois, M. Schevenels, E. Bongini, G. Degrande, G. Lombaert, A 2.5D coupled FE-BE model for the prediction of railway induced vibrations. *Soil Dynamics and Earthquake Engineering*, **30**. 1500–1512, 2010.

[5] X. Sheng, C.J.C. Jones, M. Petyt, Ground vibration generated by a harmonic load acting on a railway track. *Journal of Sound and Vibration* **225(1)**.3–28, 1999.

[6] X. Sheng, C.J.C. Jones, M. Petyt, Ground vibration generated by a load moving along a railway track. *Journal of Sound and Vibration*, **228(1)**. 129–156, 1999.

[7] A.M. Kaynia, C. Madshus, P. Zackrisson, Ground vibration from high-speed trains: prediction and countermeasure. *Journal of Geotechnical and Geoenvironmental Engineering*, **126(6)**. 531–537, 2000.

[8] M.J.M.M. Steenbergen, A.V. Metrikine, The effect of the interface conditions on the dynamic response of a beam on a half-space to a moving load. *European Journal of Mechanics A/Solids*, **26**. 33–54, 2007.

[9] L.V. Andersen, *Linear Elastodynamic Analysis*, Department of Civil Engineering, Aalborg University. DCE Lecture Notes, No. 3, 2006.

[10] W. Thomson, Transmission of elastic waves through a stratified solid medium. *Journal of Applied Physics*, **21**. 89–93, 1950.

[11] N. Haskell, The dispersion of surface waves on multilayered medium. *Bulletin of the Seismological Society of America*, **73**. 17–43, 1953.

[12] R. Wang, A simple orthonormalization method for stable and efficient computation of Green's functions. *Bulletin of the Seismological Society of America*, **89(3)**. 733–741, 1999.

[13] L. Andersen, S.R.K. Nielsen, P.H. Kirkegaard, Finite element modelling of infinite Euler beams on Kelvin foundations exposed to moving loads in convected co-ordinates. *Journal of Sound and Vibration*, **241(4)**. 587–604, 2001.

[14] X. Lei, J. Wang, Dynamic analysis of the train and slab track coupling system with finite elements in a moving frame of reference. *Journal of Vibration and Control*, **20(9)**. 1301–1317, 2014.

[15] N. Ottosen, H. Petersson, *Introduction to the finite element method*, Prentice Hall, 1992.

Paper B

Evaluating the effect of vibration isolation mats on train-induced ground vibrations

J. Malmborg, K. Persson, P. Persson
Department of Construction Sciences, Lund University
P.O. Box 118, SE-22100 Lund, Sweden

Abstract

In the present paper, the effectiveness of a vibration isolation mat for a railway slab track system is studied using a finite element model of the railway track. The finite elements are formulated in a moving frame of reference following the moving load at a particular speed. The rails are modeled using Bernoulli beams, whereas the track slab and an underlying supporting plate are modeled using Kirchhoff plate elements. The vibration isolation mat is modeled as a continuous visco-elastic layer between the track slab and the supporting plate. The response of the underlying soil is represented through a dynamic stiffness matrix, obtained via the Green's function for a horizontally layered visco-elastic strata in a moving frame of reference in the frequency–wavenumber domain. The model accounts for the quasi-static excitation caused by the static axle loads of a vehicle, as well as the dynamic excitation caused by the vehicle running over an uneven rail. The free-field response and the insertion loss obtained with the vibration isolation mat is first evaluated for a harmonic load moving along the track. Band-averaged vibration levels and the insertion loss for a fixed point next to the track are then calculated for a train cart, represented by a 10 degree-of-freedom multi-body system, running at different speeds.

1. INTRODUCTION

Due to an increasing population, many cities experience urban densification where previously unexploited land areas close to railways are now being used for new residential and office buildings. Furthermore, increasing demands on infrastructure results in heavily trafficked roads and railways close to residential areas. Annoyance from traffic-induced vibrations and noise is therefore a growing problem. To predict vibration levels arrising from traffic, and to evaluate vibration mitigation measures, models are needed for estimating the load from the vibration source as well as the vibration transmission through the ground.

One technique for reducing the vibrations from railways is to introduce an elastic mat underneath the ballast, or underneath the slab in the case of ballastless slab tracks. The performance of such elastic mats have been studied by other authors using various 2.5D and 3D models, e.g. [1–3] where boundary elements are used to account for the soil response.

In the present paper, the effectiveness of a vibration isolation mat for a railway slab track system is studied. A 3D finite element (FE) formulation in a moving frame of reference following the load is used for describing the railway track. The underlying soil response is included through a dynamic stiffness matrix obtained via the Green's function for a horizontally layered visco-elastic strata in a moving frame of reference, in the frequency–wavenumber domain. The free-field response and the insertion loss obtained with the vibration isolation mat is first evaluated for a harmonic load moving along the track. Band-averaged vibration levels and insertion loss for a fixed point next to the track are then calculated for a train cart, represented by a 10 degree-of-freedom multi-body system, running on an uneven track.

In Section 2 an overview of the model is given and the studied case is presented in Section 3. Finally, conclusions are given in Section 4.

2. MODEL OVERVIEW

In the present work the Green's function of a horizontally layered stratum, in a moving frame of reference, is calculated in the frequency–wavenumber domain and transformed to frequency–spatial domain through a double

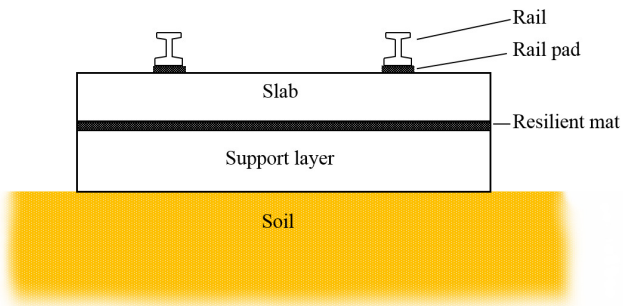

Figure 1: Section of slab track with resilient mat between the slab and the support layer.

inverse Fourier transform. It is then used to derive a dynamic stiffness matrix of the ground. The ground model is coupled to an FE representation of the railway structure, including the supporting layer, slab and rails. The supporting layer and the slab are modeled as two overlaying Kirchhoff plates. A continuous visco-elastic interface layer is introduced between the supporting layer and the slab to represent mortar or, in the case of a floating slab track, a vibration isolation mat. The rails are modeled as Bernoulli-Euler beams, connected to the slab via a continuous visco-elastic interface layer representing the rail pads. Both the ground model and the FE model are expressed in a moving frame of reference, following the vehicle at a given speed v, by introducing a coordinate transformation as

$$(\tilde{x}, \tilde{y}, \tilde{z}) = (x - vt, y, z), \tag{1}$$

where $\tilde{x}, \tilde{y}, \tilde{z}$ denotes the coordinates in the moving frame of reference.

2.1. Soil model

Introducing the coordinate transformation into the Navier's equations yields

$$\begin{aligned}(\lambda+\mu)\frac{\partial^2 \tilde{u}_j}{\partial \tilde{x}_i \partial \tilde{x}_j} + \mu \frac{\partial^2 \tilde{u}_i}{\partial \tilde{x}_j \partial \tilde{x}_j} = \\ = \rho\Big(\frac{\partial^2 \tilde{u}_i}{\partial t^2} - 2v\frac{\partial^2 \tilde{u}_i}{\partial t \partial \tilde{x}_1} + v^2 \frac{\partial^2 \tilde{u}_i}{\partial^2 \tilde{x}_1}\Big),\end{aligned} \tag{2}$$

where $\tilde{u}_i = \tilde{u}_i(\tilde{x}, \tilde{y}, \tilde{z}, t)$ is the displacement in the moving frame of reference. Fourier transforming Eq. 2 with respect to the horizontal coordinates and time, $(\tilde{x}, \tilde{y}, t)$, yields the convective Navier equations in frequency–wavenumber domain. As showed by Sheng [4], the solution for an individual layer can be found analytically, and due to continuity of displacements and tractions over interfaces between layers, several layers can be assembled using the Thomson [5] and Haskell [6] layer transfer matrix approach, forming a relationship between the displacement and stresses at the top of the stratum and at the bottom of the stratum. With known boundary conditions at the lowest interface, a relationship between the traction and the displacement at the surface can be obtained as

$$\hat{\mathbf{u}} = \hat{\mathbf{G}}\,\hat{\mathbf{p}}, \tag{3}$$

where $\hat{\mathbf{u}} = \hat{\mathbf{u}}(\tilde{k}_x, \tilde{k}_y, \omega)$ and $\hat{\mathbf{p}} = \hat{\mathbf{p}}(\tilde{k}_x, \tilde{k}_y, \omega)$ are vectors containing the displacements and tractions respectively on the soil surface, $\hat{\mathbf{G}} = \hat{\mathbf{G}}(\tilde{k}_x, \tilde{k}_y, \omega)$ is the Green's function tensor, $\tilde{k}_x$ and $\tilde{k}_y$ are the horizontal wavenumbers, and ω is the circular frequency of the moving harmonic load. For certain frequencies and stratifications, the original Thomson and Haskell method suffers from loss-of-precision. To avoid these problems in the present work, the different soil layers are assembled in an orthonormalisation procedure as proposed by Wang [7].

Equation 3 is evaluated for a set of discrete values of $\tilde{k}_x$ and $\tilde{k}_y$, and the displacement vector $\tilde{\mathbf{u}}(\tilde{x}, \tilde{y}, \omega)$ is obtained in Cartesian space through a double inverse Fourier transform of $\hat{\mathbf{u}}(\tilde{k}_x, \tilde{k}_y, \omega)$.

The procedure described above is used for calculating the response on the soil surface, due to a unit load with a rectangular spatial distribution. From this single load case, a dynamic flexibility matrix $\mathbf{F}_g(\omega, v)$ is established

for a set of DoFs where the superstructure interacts with the soil surface. These DoFs will be referred to as soil-structure interaction (SSI) DoFs. $\mathbf{F}_g$ is formed, column by column, by interpolating from $\tilde{\mathbf{u}}$. The flexibility matrix is then inverted to form the dynamic stiffness matrix of the soil, $\mathbf{D}_g(\omega, v) = \mathbf{F}_g^{-1}(\omega, v)$, which gives a relation between the steady-state displacements $\tilde{\mathbf{u}}_g$ and forces $\tilde{\mathbf{f}}_g$ for the SSI DoFs, at a certain circular frequency ω and velocity v, as

$$\mathbf{D}_g \, \tilde{\mathbf{u}}_g = \tilde{\mathbf{f}}_g. \tag{4}$$

2.2. Railway structure

Assuming steady-state conditions, the governing equation for the railway structure can be written as

$$(-\omega^2 \mathbf{M}_s + i\omega \mathbf{C}_s + \mathbf{K}_s)\tilde{\mathbf{u}}_s = \tilde{\mathbf{f}}_s, \tag{5}$$

or

$$\mathbf{D}_s \tilde{\mathbf{u}}_s = \tilde{\mathbf{f}}_s, \tag{6}$$

where $\mathbf{M}_s$, $\mathbf{C}_s$ and $\mathbf{K}_s$ is the mass, damping and stiffness matrix respectively. $\mathbf{D}_s = (-\omega^2 \mathbf{M}_s + i\omega \mathbf{C}_s + \mathbf{K}_s)$ is the dynamic stiffness matrix, and $\tilde{\mathbf{u}}_s$ and $\tilde{\mathbf{f}}_s$ is the displacement and force vector respectively. The coordinate transformation used to express the governing FE equations in a moving frame of reference introduces convective terms in the damping and stiffness matrices, see e.g. [8–10]. The track slab and the supporting layer are described using four-node rectangular Kirchhoff plate elements with three DoFs per node (vertical displacement + two rotations). The rail is decribed by two-node Bernoulli-Euler beam elements. The visco-elastic layer between the slab and the supporting layer, as well as the rail pads, are described by continuously distributed springs and dashpots. In both cases, the shear transfer between the two plates is disregarded.

2.3. Coupling between soil and FE

The track is coupled to the SSI DoFs in a standard FE manner. Here, only the vertical DoFs of the supporting plate are coupled to the soil. For the finite elements, displacements and stress distributions are governed by the element shape functions. However, for the soil, the displacements and interface tractions are governed by the load distribution chosen for calculating the soil response fundamental solution. Thus, continuity of displacements and stresses is not guaranteed along the superstructure–soil surfaces, but force and displacement continuity is enforced at the exact location of the nodes.

A global system of equations for the ground and the railway structure is formed by combining Eqs. 4 and 5, yielding

$$\mathbf{D}_t \tilde{\mathbf{u}}_s = \tilde{\mathbf{f}}_s, \tag{7}$$

where $\mathbf{D}_t$ represents the total dynamic stiffness matrix for the structure assembled onto the ground DoFs.

2.4. Free-field response

Once the displacements $\tilde{\mathbf{u}}_s$, and thereby also the subset $\tilde{\mathbf{u}}_g$, have been obtained by solving Eq. 7, the corresponding forces on the soil surface, $\tilde{\mathbf{f}}_g$ are calculated by Eq. 4. A second flexibility matrix $\mathbf{F}_{gf}(\omega, v)$ is established, in the same manner as $\mathbf{F}_g(\omega, v)$, as described in Section 2.1. The free-field displacements, $\tilde{\mathbf{u}}_f$, are then calculated as

$$\tilde{\mathbf{u}}_f = \mathbf{F}_{gf} \tilde{\mathbf{f}}_g. \tag{8}$$

These displacements are in the moving frame of reference, following the load at speed v. In this frame of reference, the displacements are in steady state with the loading frequency f. For a fixed point in the free-field, however, the response is transient. Due to the Doppler effect, the response will contain frequencies other than the excitation frequency. The fixed point response time history, $u(t)$, is obtained by moving with the train speed, along a line parallell with the track, in the opposite travel direction of the train.

3. STUDIED CASE

The model described above is used for evaluating the effect of a resilient mat placed under the track slab. The track rests on a 14 m deep layer of clay overlaying a half-space. The properties of the track and the soil layers are shown in Table 1 and Table 2, respectively. Due to symmetry, only half the track is modeled. The element length is 0.3 m in both the plates and the beams.

Table 1: Track properties.

	Parameter	Value
Rail	Mass (kg/m)	60
	Youngs modulus (GPa)	210
	Second moment of inertia (m^4)	3.217×10^{-5}
	Loss factor (-)	0.01
Rail pads	Stiffness (MN/m^2)	92.3
	Damping (kNs/m^2)	73.4
Concrete slab	Density (kg/m^3)	2500
	Youngs modulus (GPa)	34
	Poisson's ratio	0.2
	Width (m)	3.0
	Thickness (m)	0.3
	Loss factor (-)	0.04
HSL	Density (kg/m^3)	2200
	Youngs modulus (GPa)	25
	Poisson's ratio	0.2
	Width (m)	3.0
	Thickness (m)	0.4
	Loss factor (-)	0.04
Slab mat	Stiffness (MN/m^3)	10
	Damping (kNs/m^3)	20
Mortar	Stiffness (MN/m^3)	1000
	Damping (kNs/m^3)	250

Table 2: Soil properties.

Layer	Parameter	Value
Soil	Depth (m)	14.0
	Youngs modulus (MPa)	475
	Poisson's ratio	0.48
	Density (kg/m^3)	2125
	Loss factor (-)	0.14
Bedrock (half-space)	Depth (m)	∞
	Youngs modulus (MPa)	8800
	Poisson's ratio	0.40
	Density (kg/m^3)	2600
	Loss factor (-)	0.04

First, the track receptance and the free-field response is calculated for a simple harmonic unit load moving along the track at speeds $v = 30$ m/s and $v = 60$ m/s, for both the unisolated and the isolated track. Then, the free-field response due to a train cart running over an uneven track at those same velocities is calculated for both models.

3.1. Track receptance

The receptance, i.e. the displacement of the loading point, when subjecting the track to a moving harmonic unit load, is calculated for the velocities $v = 0$ m/s, $v = 30$ m/s and $v = 60$ m/s. The load is applied symmetrically on both rails, i.e. half a unit load is applied on each rail. For the floating slab, the receptance decreases noticeably with increasing load velocity and the resonance peak is shifted to a lower frequency, as shown in Figure 2. Figure 3 shows the free-field displacements for $v = 60$ m/s and $f = 40$ Hz, for the floating slab.

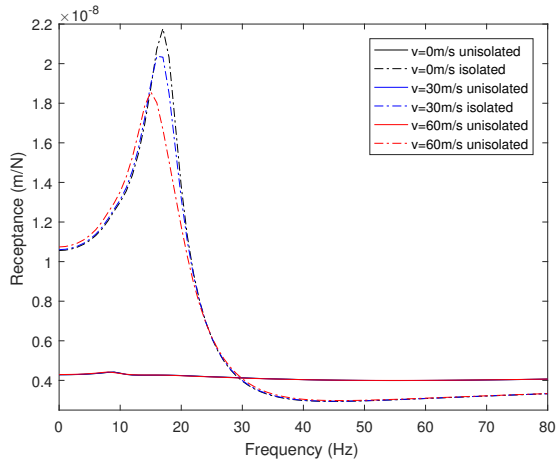

Figure 2: Track receptance.

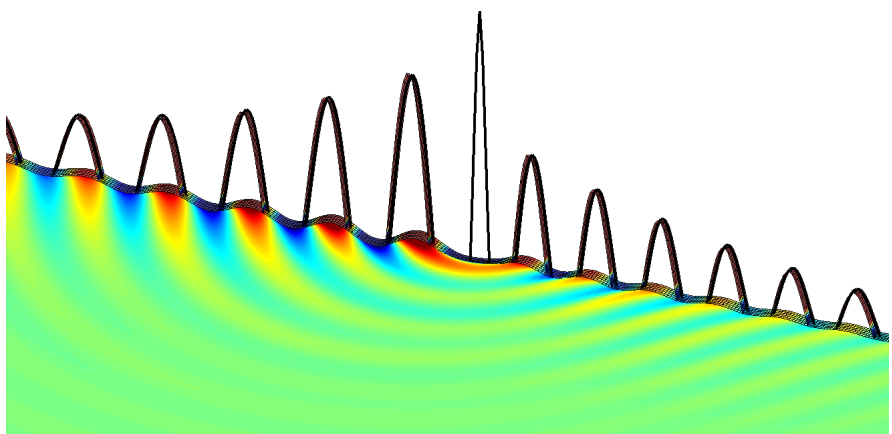

Figure 3: Free-field displacements due a harmonic point load at $f = 40$ Hz moving at a speed $v = 60$ m/s on the floating slab. The Doppler effect is clearly visible.

3.2. Insertion loss

The insertion loss quantifies the change in response due to a modification of the system. Here, it relates the displacement in the free-field obtained with the resilient mat, to the displacement obtained without the resilient mat. The insertion loss is defined as

$$IL = 20 \log_{10} \frac{u_o}{u_r}, \tag{9}$$

where u_o and u_r is the displacement in the original (unisolated) configuration and the modified (isolated) configuration, respectively.

As described in Section 2.4, the response in a fixed point in the free-field $u(t)$, due to harmonic load moving along the track, is transient. The root-mean-square (rms) value of $u(t)$ is

$$u_{rms} = \sqrt{\frac{1}{T} \int_0^T u(t)^2 \, dt}. \tag{10}$$

The rms-value of the displacement is used for calculating an insertion loss for a fixed point, due to the moving load.

Figures 4a–b show the insertion loss for points in the free-field 5 m and 25 m from the track, respectively, when the load velocity is $v = 30$ m/s. The insertion loss is shown for three points following the moving load. These points are located perpendicular to (0 m), ahead of (+10/+25 m) and behind (–10/–25 m) the moving load. Furthermore, the insertion loss calculated from the rms-value of the displacement in a fixed point is also shown. Figures 4c–d show the corresponding results for the load velocity $v = 60$ m/s.

The insertion loss is considerably higher for the point perpendicular to the moving load, than for the other two points following the load. Naturally, the insertion loss is therefore also lower for a fixed point as the load passes. The insertion loss is slighly lower for the higher load velocity, and slightly higher further from the track. Negative insertion loss is observed near the resonance frequency of the floating slab.

3.3. Train passage

Here, a 10 DoF vehicle, modeled as a multi-body system, is introduced into the model. The contact between the vehicle wheels and the rail is accounted for by means of a linearized Hertzian contact spring, i.e. the wheel is assumed to be in contact with the rail at all times. Since the track is described in a moving frame of reference following the vehicle, each wheel is connected to the same rail element throughout the analysis.

The rail unevenness is often described by a power spectral density (PSD) function, allowing the rail irregularities to be decomposed into spectral components of different wavelengths. For a single harmonic component of the track irregularity, with wavelength λ, the frequency of excitation is $f = v/\lambda$ where v is the vehicle speed. Here, the German track PSD is used to describe the rail irregularities,

$$P_z(\beta) = \frac{A_p \beta_c^2}{(\beta^2 + \beta_r^2)(\beta^2 + \beta_c^2)} \ \left[\frac{\mathrm{m}^2}{\mathrm{rad/m}}\right], \tag{11}$$

where $\beta = 2\pi/\lambda$, the constants $\beta_r = 0.0206$ rad/m and $\beta_c = 0.8246$ rad/m. A_p is a parameter defining the track quality, ranging from $A_p = 4.032{\times}10^{-7}$ m^2/(rad/m) to $A_p = 10.8{\times}10^{-7}$ m^2/(rad/m). Here, a poor track quality is assumed and hence the higher value is used in this example.

An expression for the total response power spectrum in a fixed point, when the rail irregularities are described by a PSD, was derived by Sheng [11]. The total response from the dynamic excitation of the rail irregularities, is obtained by combining the contributions from a number of discrete irregularity wavelengths. The vertical velocity levels, as well as the insertion loss based on these velocity levels, are calculated for points located 5 m and 25 m from the track, for the train speeds $v = 30$ m/s and $v = 60$ m/s. The results are presented in 1/3 octave bands, see Figure 5. As for the harmonic point load, the response in the free-field generally increases with increasing velocity.

The insertion loss is slightly higher for points further from the track, in the frequency bands above 20 Hz. The response in low frequency bands are dominated by the quasi-static load, which is significant for the free-field response close to the track. Again, negative insertion loss is obtained close to the resonance frequency of the floating slab. Close to the track, positive insertion loss is observed for the low frequencies where the response is dominated by the quasi-static response.

Table 3: Vehicle properties (from [10]).

Parameter	Value
Primary suspension stiffness k_p (MN/m)	1.18
Primary suspension damping c_p (kNs/m)	39.2
Secondary suspension stiffness k_s (MN/m)	0.53
Secondary suspension damping c_s (kNs/m)	90.2
Wheel mass m_w (kg)	$1.78{\times}10^3$
Bogie mass m_b (kg)	$3.04{\times}10^3$
Bogie inertia I_b (kgm^2)	$3.93{\times}10^3$
Body mass m_c (kg)	$41.75{\times}10^3$
Body inertia I_c (kgm^2)	$2.08{\times}10^6$

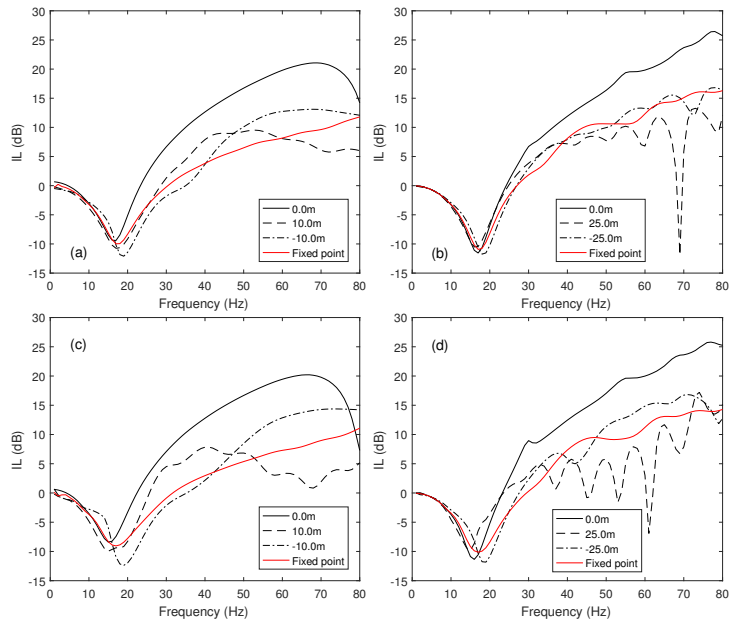

Figure 4: (a) and (b): Insertion loss in free-field points 5 m and 25 m from the track, respectively, for a moving point load at v=30 m/s. (c) and (d): Insertion loss in free-field points 5 m and 25 m from the track, respectively, for a moving point load at v=60 m/s.

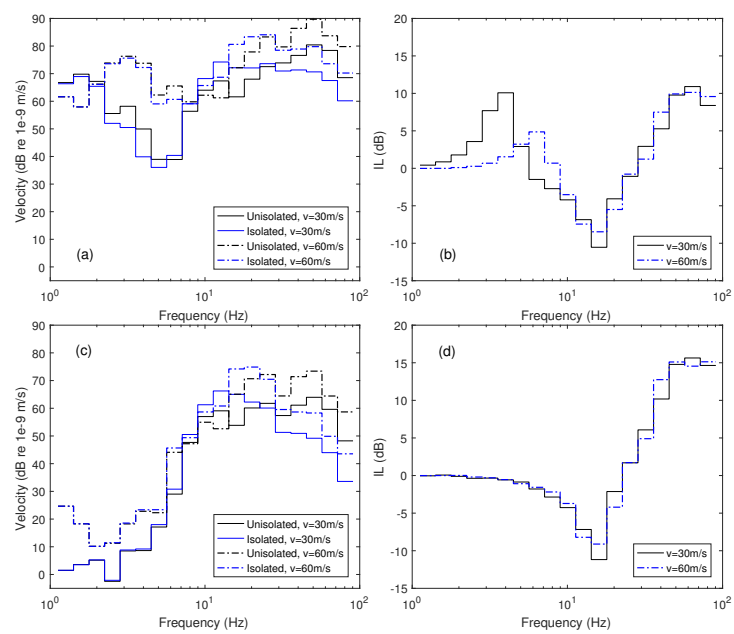

Figure 5: (a) Free-field vibration velocity levels in 1/3 octave bands for a point located 5 m from the track. (b) Corresponding insertion loss. (c) Free-field vibration velocity levels in 1/3 octave bands for a point located 25 m from the track. (d) Corresponding insertion loss.

4. Conclusions

In this paper a numerical model of a railway track has been applied to study the effect of a vibration isolation mat. The model is formulated in a frame of reference following the load moving along the track at a fixed velocity. This formulation is efficient, allowing smaller models compared to traditional 3D FE formulations. Furthermore, the moving load can be analyzed in frequency domain.

It is shown that, when a simple harmonic load moves along the track, the effect of the resilient mat on the free-field response is reduced with increasing velocity of the load. For points that are following the moving load, the insertion loss is considerably higher for a point perpendicular to the load than for other points equidistant from the track. A fixed point experiences the wave field from the moving load from all different angles as the load approaches and departs, and naturally the insertion loss is therefore lower than the maximum. Furthermore, the insertion loss is slightly higher 25 m from the track than 5 m from the track.

Introducing a resilient mat under the track slab modifies the free-field response arising from a specific load on the track, and furthermore, the modified track stiffness changes the dynamic wheel-rail interaction forces due to track unevenness. Here, the vehicle is modeled as a multi-body system, and the track uneveness is treated as a stationary stochastic process described by a PSD function. The response in the free-field generally increases with increasing velocity of the train. The insertion loss is slightly higher in the frequency bands above 20 Hz, for points further from the track. The response in low frequency bands are dominated by the quasi-static load, which is significant for the free-field response close to the track. Here, a positive insertion loss is observed, whereas again, as in the case with the moving point load, a negative insertion loss is obtained close to the resonance frequency of the floating slab.

5. Acknowledgments

The research was carried out in the framework of the project “Urban Tranquility” under the Interreg V programme. The authors of this work gratefully acknowledge the European Regional Development Fund for the financial support. Gratitude is also expressed to the City of Helsingborg for the research funding through the call “Plattformen”.

References

[1] Alves Costa P, Calcada A, Silva Cardoso A. Ballast mats for the reduction of railway traffic vibrations. Numerical study. Soil Dynamics and Earthquake Engineering 2012:42, 137–150.

[2] Lombaert G, Degrande G, Vanhauwere B, Vandeborght B, Francois S. The control of ground-borne vibrations from railway traffic by means of continuous floating slabs. Journal of Sound and Vibration 2006:297, 946–961.

[3] Galvin P, Romero A, Domingues J. Vibrations induced by HST passage on ballast and non-ballast tracks. Soil Dynamics and Earthquake Engineering 2010:30, 862–873.

[4] Sheng X, Jones CJC, Petyt M. Ground vibration generated by a load moving along a railway track. Journal of Sound and Vibration 1999:228(1), 129–156.

[5] Thomson W. Transmission of elastic waves through a stratified solid medium. Journal of Applied Physics 1950:21, 89–93.

[6] Haskell N. The dispersion of surface waves on multilayered medium. Bulletin of the Seismological Society of America 1953:73, 17–43.

[7] Wang R. A simple orthonormalization method for stable and efficient computation of Green’s functions. Bulletin of the Seismological Society of America 1999:89(3), 733–741.

[8] Andersen, LV. Linear Elastodynamic Analysis, Department of Civil Engineering, Aalborg University. DCE Lecture Notes, No. 3, 2006.

[9] Andersen L, Nielsen SRK, Kirkegaard PH. Finite element modelling of infinite Euler beams on Kelvin foundations exposed to moving loads in convected co-ordinates. Journal of Sound and Vibration 2001:241(4), 587–604.

[10] Lei X, Wang J. Dynamic analysis of the train and slab track coupling system with finite elements in a moving frame of reference. Journal of Vibration and Control 2014:20(9), 1301–1317.

[11] Sheng X, Jones CJC, Thompson DJ. A theoretical model for ground vibration from trains generated by vertical track irregularities. Journal of Sound and Vibration 2004:272, 937–965.

Paper C

Effects of modeling strategies for a slab track on predicted ground vibrations

J. Malmborg, P. Persson, K. Persson
Department of Construction Sciences, Lund University
P.O. Box 118, SE-22100 Lund, Sweden
jens.malmborg@construction.lth.se

Abstract

In the paper, the effect of modeling strategies regarding the dynamic behavior of a railway slab track on a layered half-space is studied. The track is modeled with various degrees of accuracy through the use of either beam theory, shell finite elements or solid finite elements. The underlying soil response is included through a dynamic stiffness, obtained via the Green's function for a horizontally layered visco-elastic half-space in the frequency–wavenumber domain. The effect of different assumptions regarding the track cross-section behavior and the track–soil interface conditions on the resulting free-field vibrations are studied for a harmonic load moving along the track. First, only the out-of-plane displacements of the slab–soil interface are coupled, i.e. only the vertical contact pressure is accounted for. Secondly, the effect of coupling the slab–soil in-plane displacements on the free-field vibrations is studied. It was found that the in-plane slab–soil coupling significantly affects the vertical vibration in the free-field. It was also found that a beam model of the track yields accurate response levels compared to a solid continuum model in the case of a thick slab, whereas considerable differences were obtained for a thin slab.

Keywords: Train-induced ground vibration, moving frame of reference, slab track, finite element, Green's function.

1. Introduction

Due to an increasing population, many cities experience urban densification. Previously unexploited areas, close to railways and heavily trafficked roads, are now being developed for residential and office buildings. Annoyance from traffic-induced vibrations and noise is therefore a growing problem.

To estimate the load from the vibration source and to predict the vibration transmission through the ground, models are needed. Ground vibrations caused by passing trains have been studied using a wide range of different techniques in the past decades, ranging from empirical methods to analytical and numerical calculation models. Numerical prediction models often employ either the finite element (FE) method or the boundary element (BE) method, or a combination thereof. The FE method enables arbitrary geometries and discontinuities to be modeled, but the need to discretize a large computational domain may lead to long computation times. Furthermore, when modeling wave propagation, the truncation of the model geometry may lead to spurious reflections of elastic waves unless the artificial boundaries are properly modeled. The BE method inherently includes non-reflecting

boundaries, but depending on the model size, the computational cost may still be high. If the soil and track are assumed to be invariant in the track direction, the computational cost may be reduced through the use of so called 2.5D models [1–6], where a Fourier transform with respect to the coordinates in the track direction is performed and a 2D problem is solved for a sequence of wavenumbers, using either the FE method, the BE method, analytical methods, or a combination of these.

Apart from the FE and BE methods, some models utilize that a fundamental solution (Green's function) for the soil response can be found analytically in frequency–wavenumber domain for a horizontally layered visco-elastic half-space. Several authors have used such a soil model coupled to a railway track. *Sheng et al* [7, 8] derived a semi-analytical model, with the track represented by an infinite layered beam resting on a layered ground, where both the ground and the beam are described in the frequency–wavenumber domain, in the reference frame of the moving load. *Kaynia et al* [9] coupled a series of FE beams, representing the railway track, to a dynamic stiffness matrix of the ground calculated from the Green's function of a layered half-space. *Triepaischajonsak et al* [10] calculated the track/ground interaction forces in time domain using a beam on elastic foundation, and introduced the calculated forces into a ground model in frequency–wavenumber domain to predict the free-field vibrations. *Koroma et al* [11] used a time-domain FE model of the track, with the soil stiffness described by lumped parameter models, to calculate the track–soil interaction forces that were subsequently used for calculating the free-field vibrations in frequency–wavenumber domain using a layered half-space model.

Modeling the track as a beam is a common approach in both track/vehicle dynamics analyses and predictions of ground-borne vibrations. However, when the track is modeled as a beam, some assumptions regarding the displacements or the stress distribution in the track–soil interface have to be made, which may affect the resulting ground vibrations. *Steenbergen et al* [12] studied the influence of different interface conditions between a beam on a half-space, subjected to a dynamic moving load, on the free-field response, using a semi-analytical model in the frequency–wavenumber domain. *Galvín et al* [4] compared the free-field response of a high-speed train passage on a ballasted track on an embankment, calculated using a 2.5D continuum model, to a model with a beam representation of the track, finding large differences attributed to the rigid cross-section of the embankment using the beam model.

State-of-the-art models for train-induced ground vibrations, utilizing continuum representations of the railway track, account for both the track cross-section flexibility and the in-plane shear forces of the track–soil interface. To the authors knowledge, it has previously not been demonstrated what the implications are of using a simplified approach concerning the track and track–soil coupling, when predicting the ground vibrations caused by a load moving over a slab track. The subject was touched upon in a conference paper by the authors [13]. For use in early design stages, prediction tools need to be fast to enable swift evaluation of different design alternatives or response sensitivity to model parameters, while maintaining sufficient accuracy to provide meaningful results. In the present paper, the free-field ground vibrations due to a harmonic load moving at constant velocity along a railway slab track are calculated using different assumptions of the slab cross-section behavior and the track–soil interface conditions.

2. Study overview

The influence of various modeling strategies on the predicted ground vibrations was studied for a slab track that is shown principally in Figure 1. It consists of a concrete slab, rails and rail pads. The study is performed for two slab thicknesses, $t = 0.2$ m and $t = 0.5$ m. The slab width is 3.0 m for both thicknesses. The track properties used are given in Table 1.

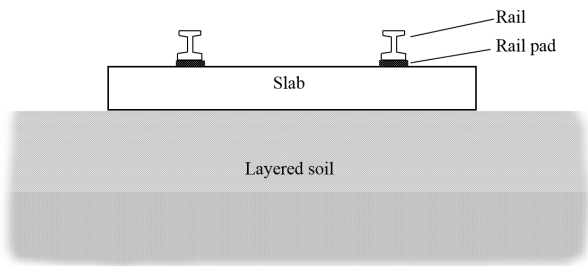

Figure 1: Schematic cross-section of slab track on a layered soil.

The track is assumed to rest on a 14 m deep layer of clay overlaying a half-space. The analyses are performed for two different values of the clay layer's Young's modulus, presented in Table 2. The stiffer soil properties are that of a stiff clay till, where the parameters were obtained through geotechnical and geophysical measurements at a site in the city of Lund, Sweden, close to a research facility housing highly vibration-sensitive equipment. The Rayleigh wave speed for this soil is $c_R = 261$ m/s. The Young's modulus for the softer soil is chosen to give a Rayleigh wave speed approximately equal to half of that for the stiffer soil, $c_R = 131$ m/s.

Four computational models, Models a) – d), with different assumptions regarding the slab and the slab–soil interface conditions, are established as:

a) The slab is modeled as a Bernoulli–Euler beam. Vertical displacement continuity of the beam and the soil is enforced along the beam center line. A uniform normal stress distribution between the beam and the soil is assumed in the transverse direction of the slab. In-plane coupling of the slab–soil is disregarded.

b) The slab is modeled as a Bernoulli–Euler beam. The slab–soil interface is assumed rigid in the transverse direction, enforcing vertical displacement continuity of the beam and the soil under the full width of the slab. The axial rigidity of the slab is modeled using the bar equation. Laterally, the slab is assumed rigid, enforcing zero displacements of the soil in the cross-direction under the slab.

c) The slab is modeled with Kirchhoff shell elements, allowing a more general slab–soil interface stress and displacement distribution in the transverse direction of the slab than by the aforementioned models. Displacement and force continuity is enforced in the nodes of the slab–soil interface.

d) The slab is modeled with 3D solid elements, allowing the most general stress and displacement field of the four models. Displacement and force continuity is enforced in the nodes of the slab–soil interface.

Models a) – b) are semi-analytical, not requiring the introduction of finite elements as for Models c) – d). The rails are modeled as Bernoulli-Euler beams in all four models. The loading is assumed identical on both rails and in Models a) and b) the two rails are accordingly modeled as one single rail. In Models c) and d), only half of the track is modeled, due to assumed symmetry around the track center line. The models are formulated in a moving frame of reference following the load at at specific speed, requiring that the track is assumed invariant in the load travel direction. Hence, the discrete rail supports are modeled as a continuous visco-elastic interface layer between the rail and the slab. The underlying soil response is included through a dynamic stiffness, obtained via the Green's function for a horizontally layered visco-elastic stratum in the frequency–wavenumber domain, as further described in Section 3. The track models and their coupling to the soil is further detailed in Section 4 . The Models a) – d) are shown schematically in Figure 2.

To compare the effect of the various modeling strategies for the track, each of Model a) – d) was used for evaluating the vertical free-field response to a moving unit harmonic point load acting on the rail, with frequencies in the range 5 to 80 Hz. The velocity of the moving load, set to $v = 30$ m/s, was chosen since it is a common train velocity in urban areas. First, only vertical coupling of the slab to the soil was accounted for. Then, the in-plane slab–soil displacements were also coupled.

Damping is introduced in the models through the use of complex Young's moduli for the ground, the slab and the rails. For the FE models, an element length of 0.15 m is used in both the longitudinal and lateral direction. For the solid model, six elements are used in the thickness direction of the slab. For the semi-analytical model, 4096×4096 points are used in wavenumber domain, with a maximum wavenumber of 41 rad/m in both directions. In Model b) the slab–soil interface is laterally discretized into 21 strips. The aforementioned discretizations were found to be sufficient. In the FE models, the displacement boundary conditions are free at the truncated ends of the track. The total track length is 90 m, which has been found to be sufficient to avoid problems with reflecting waves at the free boundaries.

Table 1: Track properties.

	Parameter	Value
Rail	Mass (kg/m)	60
	Young's modulus (GPa)	210
	Second moment of inertia (m^4)	3.217×10^{-5}
	Loss factor (-)	0.01
	Track gauge (m)	1.435
Rail pads	Stiffness (MN/m^2)	250
	Damping (kNs/m^2)	22.5
Slab	Density (kg/m^3)	2500
	Young's modulus (GPa)	30
	Poisson's ratio	0.2
	Width (m)	3.0
	Thickness (m)	0.2 / 0.5
	Loss factor (-)	0.04

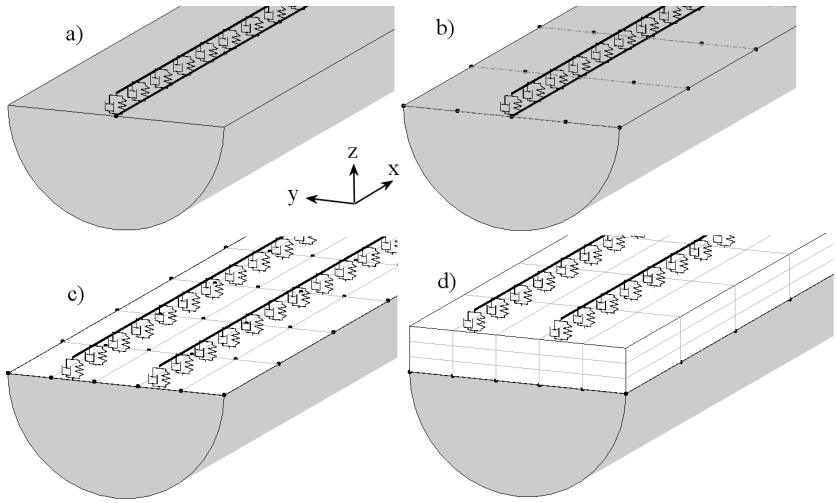

Figure 2: Schematic view of computational models. In Models a) and b) the slab is modeled as Bernoulli–Euler beams with different slab–soil interface conditions. In Models c) and d) the slab is modeled by Kirchhoff shell and 3D solid continuum finite elements, respectively.

Table 2: Ground properties.

Layer	Parameter	Value
Soil	Depth (m)	14
	Young's modulus (MPa)	475 / 120
	Poisson's ratio	0.48
	Density (kg/m^3)	2125
	Loss factor (-)	0.14
Bedrock	Depth (m)	∞
(half-space)	Young's modulus (MPa)	8800
	Poisson's ratio	0.40
	Density (kg/m^3)	2600
	Loss factor (-)	0.04

3. Soil model

The ground is assumed to be composed of horizontal visco-elastic layers. Neglecting body forces, the Navier equations for a single soil layer can be written as

$$(\lambda+\mu)\frac{\partial^2 u_j}{\partial x_i \partial x_j}+\mu\frac{\partial^2 u_i}{\partial x_j \partial x_j}=\rho\frac{\partial^2 u_i}{\partial t^2}, \tag{1}$$

where $u_i = u_i(x_1, x_2, x_3, t)$ is the displacement in direction *i*. The Lamé parameters are λ and μ.

The equations are obtained in the frame of reference following the load moving at a fixed speed v along the x_1-axis by applying the coordinate transformation,

$$(\tilde{x}_1, \tilde{x}_2, \tilde{x}_3) = (x_1 - vt, x_2, x_3), \tag{2}$$

where $\tilde{x}_1, \tilde{x}_2, \tilde{x}_3$ denotes the coordinates in the moving frame of reference. Partial derivatives in the two reference frames are related as [14]

$$\frac{\partial}{\partial x_1} = \frac{\partial}{\partial \tilde{x}_1}, \qquad \left.\frac{\partial}{\partial t}\right|_{x_1} = \left.\frac{\partial}{\partial t}\right|_{\tilde{x}_1} - v\frac{\partial}{\partial \tilde{x}_1}, \tag{3}$$

which applied to Eq. (1) yields

$$(\lambda+\mu)\frac{\partial^2 \tilde{u}_j}{\partial \tilde{x}_i \partial \tilde{x}_j} + \mu\frac{\partial^2 \tilde{u}_i}{\partial \tilde{x}_j \partial \tilde{x}_j} = \rho\Big(\frac{\partial^2 \tilde{u}_i}{\partial t^2} - 2v\frac{\partial^2 \tilde{u}_i}{\partial t \partial \tilde{x}_1} + v^2\frac{\partial^2 \tilde{u}_i}{\partial^2 \tilde{x}_1}\Big), \tag{4}$$

where $\tilde{u}_i = \tilde{u}_i(\tilde{x}, \tilde{y}, \tilde{z}, t)$ is the displacement in the moving frame of reference.

Fourier transforming the Navier equations with respect to the horizontal coordinates and time, $(\tilde{x}_1, \tilde{x}_2, t)$, yields the Navier equations in frequency–wavenumber domain as

$$(\lambda+\mu)\tilde{\Delta}\mathrm{i}\tilde{k}_1 + \mu\Big(\frac{\mathrm{d}^2}{\mathrm{d}\tilde{x}_3^2} - \tilde{k}_1^2 - \tilde{k}_2^2\Big)\tilde{U}_1 = -\rho\tilde{\omega}^2\tilde{U}_1, \tag{5a}$$

$$(\lambda+\mu)\tilde{\Delta}\mathrm{i}\tilde{k}_2 + \mu\Big(\frac{\mathrm{d}^2}{\mathrm{d}\tilde{x}_3^2} - \tilde{k}_1^2 - \tilde{k}_2^2\Big)\tilde{U}_2 = -\rho\tilde{\omega}^2\tilde{U}_2, \tag{5b}$$

$$(\lambda+\mu)\frac{\mathrm{d}\tilde{\Delta}}{\mathrm{d}\tilde{x}_3} + \mu\Big(\frac{\mathrm{d}^2}{\mathrm{d}\tilde{x}_3^2} - \tilde{k}_1^2 - \tilde{k}_2^2\Big)\tilde{U}_3 = -\rho\tilde{\omega}^2\tilde{U}_3, \tag{5c}$$

where $\tilde{\Delta} = \tilde{\Delta}(\tilde{k}_1, \tilde{k}_2, \tilde{x}_3, \omega)$ and $\tilde{U}_i = \tilde{U}_i(\tilde{k}_1, \tilde{k}_2, \tilde{x}_3, \omega)$ are the Fourier transforms, with respect to the horizontal coordinates and time, of the dilation $\Delta(\tilde{x}_1, \tilde{x}_2, \tilde{x}_3, t)$ and the displacement $\tilde{u}_i(\tilde{x}, \tilde{y}, \tilde{z}, t)$, respectively. The imaginary unit is denoted i. The vibration frequency of a material point is $\tilde{\omega} = \omega - \tilde{k}_1 v$ and ω is the circular frequency of the moving load. The horizontal wavenumbers in the direction of $\tilde{x}_1$ and $\tilde{x}_2$ are $\tilde{k}_1$ and $\tilde{k}_2$, respectively.

The solution to Eq. (5) for an individual layer can be found analytically, as showed by *Sheng et al* [7, 8]. Due to continuity of displacements and tractions over interfaces between layers, the Thomson [15] and Haskell [16] layer transfer matrix approach can be used to assemble several layers, forming a relationship between the displacement and stresses at the top of the stratum and at the bottom of the stratum. A relationship between the traction and the displacements at the soil surface can be obtained as

$$\hat{\mathbf{u}} = \hat{\mathbf{G}}\,\hat{\mathbf{p}}, \tag{6}$$

where

$$\hat{\mathbf{u}} = \hat{\mathbf{u}}(\tilde{k}_1, \tilde{k}_2, \omega) = \begin{bmatrix} \hat{u}_x \\ \hat{u}_y \\ \hat{u}_z \end{bmatrix}, \quad \hat{\mathbf{p}} = \hat{\mathbf{p}}(\tilde{k}_1, \tilde{k}_2, \omega) = \begin{bmatrix} \hat{p}_x \\ \hat{p}_y \\ \hat{p}_z \end{bmatrix}, \tag{7}$$

are vectors containing the displacements and tractions, respectively, on the soil surface, and

$$\hat{\mathbf{G}} = \hat{\mathbf{G}}(\tilde{k}_1, \tilde{k}_2, \omega) = \begin{bmatrix} \hat{G}_{11} & \hat{G}_{12} & \hat{G}_{13} \\ \hat{G}_{21} & \hat{G}_{22} & \hat{G}_{23} \\ \hat{G}_{31} & \hat{G}_{32} & \hat{G}_{33} \end{bmatrix}, \tag{8}$$

is the Green's function tensor for the layered half-space.

For certain frequencies and stratifications, the original Thomson and Haskell method suffers from loss-of-precision. To avoid these problems in the present work, the different soil layers are assembled in an orthonormalization procedure as proposed by Wang [17].

Equation (6) is evaluated for a set of discrete values of $\tilde{k}_1$ and $\tilde{k}_2$, and the displacement vector $\tilde{\mathbf{u}}(\tilde{x}_1, \tilde{x}_2, \omega)$ is obtained in Cartesian space through a double inverse Fourier transform of $\hat{\mathbf{u}}(\tilde{k}_1, \tilde{k}_2, \omega)$.

4. Track models

4.1. Semi-analytical beam models: Models a) and b)

Here, due to the assumed symmetry, both rails are represented as one infinite beam with the total bending stiffness $(EI)_\mathrm{r}$ and mass m_r. The rail is supported by continuously distributed springs and dashpots representing the rail pads, with stiffness k_p and damping c_p. The rail pads are connected to the slab, represented by an infinite beam with bending stiffness $(EI)_\mathrm{s}$ and mass m_s. To account for the shear force in the axial direction of the soil–slab interface, an infinite bar with axial stiffness $(EA)_\mathrm{s}$ represents the axial rigidity of the slab. The rail is subjected to a harmonic load P_0 with circular frequency Ω, moving in the positive x-direction with the velocity v. The system is described by three equations:

$$\begin{aligned}
(EI)_\mathrm{r}\frac{\partial^4 u_\mathrm{r}}{\partial x^4} + m_\mathrm{r}\frac{\partial^2 u_\mathrm{r}}{\partial t^2} + k_\mathrm{p}\Big(u_\mathrm{r} - u_\mathrm{s}\Big) + c_\mathrm{p}\Big(\frac{\partial u_\mathrm{r}}{\partial t} - \frac{\partial u_\mathrm{s}}{\partial t}\Big) &= \delta(x - vt)P_0\mathrm{e}^{\mathrm{i}\Omega t}, \\
(EI)_\mathrm{s}\frac{\partial^4 u_\mathrm{s}}{\partial x^4} + m_\mathrm{s}\frac{\partial^2 u_\mathrm{s}}{\partial t^2} + k_\mathrm{p}\Big(u_\mathrm{s} - u_\mathrm{r}\Big) + c_\mathrm{p}\Big(\frac{\partial u_\mathrm{s}}{\partial t} - \frac{\partial u_\mathrm{r}}{\partial t}\Big) &= -F_z, \\
(EA)_\mathrm{s}\frac{\partial^2 w_\mathrm{s}}{\partial x^2} - m_\mathrm{s}\frac{\partial^2 w_\mathrm{s}}{\partial t^2} &= F_x,
\end{aligned} \tag{9}$$

where $u_\mathrm{r} = u_\mathrm{r}(x,t)$ and $u_\mathrm{s} = u_\mathrm{s}(x,t)$ is the vertical displacement of the rail and slab, respectively and $w_\mathrm{s} = w_\mathrm{s}(x,t)$ is the axial displacement of the slab. Further, $F_z = F_z(x,t)$ is the vertical force in the slab–soil interface and $F_x = F_x(x,t)$ is the shear force in the axial direction of the slab–soil interface. The interface force terms couple the third equation to the first two in Eq. (9). The equations are obtained in the frame of reference following the load by applying the coordinate transformation in Eq. (2),

$$\begin{aligned}
&(EI)_\mathrm{r}\frac{\partial^4 \tilde{u}_\mathrm{r}}{\partial \tilde{x}^4} + m_\mathrm{r}\Big(\frac{\partial^2 \tilde{u}_\mathrm{r}}{\partial t^2} - 2v\frac{\partial^2 \tilde{u}_\mathrm{r}}{\partial \tilde{x}\partial t} + v^2\frac{\partial^2 \tilde{u}_\mathrm{r}}{\partial \tilde{x}^2}\Big) + k_\mathrm{p}\Big(\tilde{u}_\mathrm{r} - \tilde{u}_\mathrm{s}\Big) + c_\mathrm{p}\Big((\frac{\partial \tilde{u}_\mathrm{r}}{\partial t} - v\frac{\partial \tilde{u}_\mathrm{r}}{\partial \tilde{x}}) - (\frac{\partial \tilde{u}_\mathrm{s}}{\partial t} - v\frac{\partial \tilde{u}_\mathrm{s}}{\partial \tilde{x}})\Big) \\
&= \delta(\tilde{x})P_0\mathrm{e}^{\mathrm{i}\Omega t}, \\
&(EI)_\mathrm{s}\frac{\partial^4 \tilde{u}_\mathrm{s}}{\partial \tilde{x}^4} + m_\mathrm{s}\Big(\frac{\partial^2 \tilde{u}_\mathrm{s}}{\partial t^2} - 2v\frac{\partial^2 \tilde{u}_\mathrm{s}}{\partial \tilde{x}\partial t} + v^2\frac{\partial^2 \tilde{u}_\mathrm{s}}{\partial \tilde{x}^2}\Big) + k_\mathrm{p}\Big(\tilde{u}_\mathrm{s} - \tilde{u}_\mathrm{r}\Big) + c_\mathrm{p}\Big((\frac{\partial \tilde{u}_\mathrm{s}}{\partial t} - v\frac{\partial \tilde{u}_\mathrm{s}}{\partial \tilde{x}}) - (\frac{\partial \tilde{u}_\mathrm{r}}{\partial t} - v\frac{\partial \tilde{u}_\mathrm{r}}{\partial \tilde{x}})\Big) = -\tilde{F}_z, \\
&(EA)_\mathrm{s}\frac{\partial^2 \tilde{w}_\mathrm{s}}{\partial \tilde{x}^2} - m_\mathrm{s}\Big(\frac{\partial^2 \tilde{w}_\mathrm{s}}{\partial t^2} - 2v\frac{\partial^2 \tilde{w}_\mathrm{s}}{\partial \tilde{x}\partial t} + v^2\frac{\partial^2 \tilde{w}_\mathrm{s}}{\partial \tilde{x}^2}\Big) = \tilde{F}_x,
\end{aligned} \tag{10}$$

where, again, $\tilde{}$ denotes that a variable is expressed in the moving frame of reference. Fourier transforming Eq. (10) with respect to $\tilde{x}$ yields

$$
\begin{aligned}
&(EI)_{\mathrm{r}}\tilde{k}_1^4\bar{u}_{\mathrm{r}} + m_{\mathrm{r}}\Big(\frac{\partial^2\bar{u}_{\mathrm{r}}}{\partial t^2} - 2\mathrm{i}v\tilde{k}_1\frac{\partial\bar{u}_{\mathrm{r}}}{\partial t} - v^2\tilde{k}_1^2\bar{u}_{\mathrm{r}}\Big) + k_{\mathrm{p}}\Big(\bar{u}_{\mathrm{r}} - \bar{u}_{\mathrm{s}}\Big) + c_{\mathrm{p}}\Big((\frac{\partial\bar{u}_{\mathrm{r}}}{\partial t} - \mathrm{i}v\bar{u}_{\mathrm{r}}) - (\frac{\partial\bar{u}_{\mathrm{s}}}{\partial t} - \mathrm{i}v\bar{u}_{\mathrm{s}})\Big) = P_0\mathrm{e}^{\mathrm{i}\Omega t},\\
&(EI)_{\mathrm{s}}\tilde{k}_1^4\bar{u}_{\mathrm{s}} + m_{\mathrm{s}}\Big(\frac{\partial^2\bar{u}_{\mathrm{s}}}{\partial t^2} - 2\mathrm{i}v\tilde{k}_1\frac{\partial\bar{u}_{\mathrm{s}}}{\partial t} - v^2\tilde{k}_1^2\bar{u}_{\mathrm{s}}\Big) + k_{\mathrm{p}}\Big(\bar{u}_{\mathrm{s}} - \bar{u}_{\mathrm{r}}\Big) + c_{\mathrm{p}}\Big((\frac{\partial\bar{u}_{\mathrm{s}}}{\partial t} - \mathrm{i}v\bar{u}_{\mathrm{s}}) - (\frac{\partial\bar{u}_{\mathrm{r}}}{\partial t} - \mathrm{i}v\bar{u}_{\mathrm{r}})\Big) = -\bar{F}_z,\\
&(EA)_{\mathrm{s}}\tilde{k}_1^2\bar{w}_{\mathrm{s}} + m_{\mathrm{s}}\Big(\frac{\partial^2\bar{w}_{\mathrm{s}}}{\partial t^2} - 2\mathrm{i}v\tilde{k}_1\frac{\partial\bar{w}_{\mathrm{s}}}{\partial t} - v^2\tilde{k}_1^2\bar{w}_{\mathrm{s}}\Big) = -\bar{F}_x,
\end{aligned}
\tag{11}
$$

with $\bar{u} = \bar{u}(\tilde{k}_1, t) = \int_{-\infty}^{\infty}\tilde{u}(\tilde{x}, t)\mathrm{e}^{-\mathrm{i}\tilde{k}_1\tilde{x}}\mathrm{d}\tilde{x}$, $\bar{w} = \bar{w}(\tilde{k}_1, t) = \int_{-\infty}^{\infty}\tilde{w}(\tilde{x}, t)\mathrm{e}^{-\mathrm{i}\tilde{k}_1\tilde{x}}\mathrm{d}\tilde{x}$, $\bar{F}_i = \bar{F}_i(\tilde{k}_1, t) =$
$= \int_{-\infty}^{\infty}\tilde{F}_i(\tilde{x}, t)\mathrm{e}^{-\mathrm{i}\tilde{k}_1\tilde{x}}\mathrm{d}\tilde{x}$, and $\tilde{k}_1$ denotes the wavenumber in the direction of $\tilde{x}$.

Further, assuming steady-state vibration with circular frequency Ω, i.e. $\bar{u}(\tilde{k}_1, t) = \hat{u}(\tilde{k}_1)\mathrm{e}^{\mathrm{i}\Omega t}$ and $\bar{w}(\tilde{k}_1, t) = \hat{w}(\tilde{k}_1)\mathrm{e}^{\mathrm{i}\Omega t}$, and setting $\omega = \Omega - \tilde{k}_1 v$ yields

$$
\begin{aligned}
(EI)_{\mathrm{r}}\tilde{k}_1^4\hat{u}_{\mathrm{r}} - \omega^2 m_{\mathrm{r}}\hat{u}_{\mathrm{r}} + k_{\mathrm{p}}\Big(\hat{u}_{\mathrm{r}} - \hat{u}_{\mathrm{s}}\Big) + \mathrm{i}\omega c_{\mathrm{p}}\Big(\hat{u}_{\mathrm{r}} - \hat{u}_{\mathrm{s}}\Big) &= P_0,\\
(EI)_{\mathrm{s}}\tilde{k}_1^4\hat{u}_{\mathrm{s}} - \omega^2 m_{\mathrm{s}}\hat{u}_{\mathrm{s}} + k_{\mathrm{p}}\Big(\hat{u}_{\mathrm{s}} - \hat{u}_{\mathrm{r}}\Big) + \mathrm{i}\omega c_{\mathrm{p}}\Big(\hat{u}_{\mathrm{s}} - \hat{u}_{\mathrm{r}}\Big) &= -\hat{F}_z,\\
(EA)_{\mathrm{s}}\tilde{k}_1^2\hat{w}_{\mathrm{s}} - \omega^2 m_{\mathrm{s}}\hat{w}_{\mathrm{s}} &= -\hat{F}_x.
\end{aligned}
\tag{12}
$$

Sheng et al [7, 8] assumed a uniform contact pressure in the lateral direction of the track–soil interface and disregarded any horizontal coupling. This is also the assumption made here for Model a). *Steenbergen et al* [12] and *Ntotsios et al* [19] accounted for a varying contact pressure in the track–soil interface by discretizing the interface laterally into a number of strips, assuming a constant pressure within each strip. The same principle is adopted here for Model b), not only the vertical contact pressure, but also for the interface shear stress in the longitudinal and lateral directions. The interface is discretized into N strips with a uniform width, i.e. the width of a single strip is $\Delta = b/N$, where b is the slab width.

A strip centered around the $\tilde{y}$-axis, with a unit force in direction j is considered. The strip stress is

$$
p_j(\tilde{x}, \tilde{y}) = \begin{cases} \frac{1}{\Delta}, & -\Delta/2 < \tilde{y} < \Delta/2 \\ 0, & \text{otherwise} \end{cases}.
\tag{13}
$$

In wavenumber domain the interface stress becomes

$$
\hat{p}_j(\tilde{k}_1, \tilde{k}_2) = \frac{\sin(\tilde{k}_2\Delta/2)}{\tilde{k}_2\Delta/2}.
\tag{14}
$$

Denote the soil displacement in direction i due to the soil surface stress in direction j by $\hat{u}_{ij}$. From Eq. (6) this displacement is obtained as $\hat{u}_{ij}(\tilde{k}_1, \tilde{k}_2) = \hat{G}_{ij}(\tilde{k}_1, \tilde{k}_2)\hat{p}_j(\tilde{k}_1, \tilde{k}_2)$ (no summation on repeated indices).

The soil displacement at an arbitrary y-coordinate, due to the loaded strip becomes

$$\hat{\tilde{u}}_{ij}(\tilde{k}_1, y) = \frac{1}{2\pi}\int_{\infty}^{\infty} \hat{u}_{ij}(\tilde{k}_1, \tilde{k}_2)\mathrm{e}^{\mathrm{i}\tilde{k}_2 y}\mathrm{d}\tilde{k}_2 = \frac{1}{2\pi}\int_{\infty}^{\infty} \hat{G}_{ij}(\tilde{k}_1, \tilde{k}_2)\hat{p}_j(\tilde{k}_1, \tilde{k}_2)\mathrm{e}^{\mathrm{i}\tilde{k}_2 y}\mathrm{d}\tilde{k}_2 = \tag{15}$$

$$\frac{1}{2\pi}\int_{\infty}^{\infty} \hat{G}_{ij}(\tilde{k}_1, \tilde{k}_2)\frac{\sin(\tilde{k}_2\Delta/2)}{\tilde{k}_2\Delta/2}\mathrm{e}^{\mathrm{i}\tilde{k}_2 y}\mathrm{d}\tilde{k}_2 = \hat{\tilde{H}}_{ij}(\tilde{k}_1, y).$$

$\hat{\tilde{H}}_{ij}(\tilde{k}_1, y)$ is a transfer function, expressing the displacements at y due to a unit load at the strip centered around $y = 0$. Due to the translational invariability of the soil, $\hat{\tilde{H}}_{ij}(\tilde{k}_1, y)$ can be used for calculating the soil displacement at any distance along the y-axis from any loaded strip, by replacing the coordinate y with the distance. Hence, for each wavenumber $\tilde{k}_1$, a matrix expression can be established linking the displacements and forces in all the strips,

$$\begin{bmatrix} \hat{\tilde{H}}_{11}(0) & \hat{\tilde{H}}_{12}(0) & ... & \hat{\tilde{H}}_{13}(-(N-1)\Delta) \\ \hat{\tilde{H}}_{21}(0) & \hat{\tilde{H}}_{22}(0) & ... & \hat{\tilde{H}}_{23}(-(N-1)\Delta) \\ \hat{\tilde{H}}_{31}(0) & \hat{\tilde{H}}_{32}(0) & ... & \hat{\tilde{H}}_{33}(-(N-1)\Delta) \\ \hat{\tilde{H}}_{11}(\Delta) & \hat{\tilde{H}}_{12}(\Delta) & ... & \hat{\tilde{H}}_{13}(-(N-2)\Delta) \\ \vdots & \vdots & ... & \vdots \\ \hat{\tilde{H}}_{31}((N-1)\Delta) & \hat{\tilde{H}}_{32}((N-1)\Delta) & ... & \hat{\tilde{H}}_{33}(0) \end{bmatrix} \begin{bmatrix} \hat{F}_{1x} \\ \hat{F}_{1y} \\ \vdots \\ \hat{F}_{Nz} \end{bmatrix} = \begin{bmatrix} \hat{u}_{1x} \\ \hat{u}_{1y} \\ \vdots \\ \hat{u}_{Nz} \end{bmatrix}, \tag{16}$$

where the argument $\tilde{k}_1$ has been dropped for brevity. Equation (16) can be written as $\hat{\tilde{\mathbf{H}}}\hat{\mathbf{F}} = \hat{\mathbf{u}}$. For known displacements, the strip forces are $\hat{\mathbf{F}} = \hat{\tilde{\mathbf{H}}}^{-1}\hat{\mathbf{u}}$. Enforcing equal displacements in all strips, a (3×3) system is obtained from $\hat{\tilde{\mathbf{H}}}^{-1}$,

$$\begin{bmatrix} k_{11} & k_{12} & k_{13} \\ k_{21} & k_{22} & k_{23} \\ k_{31} & k_{32} & k_{33} \end{bmatrix} \begin{bmatrix} \hat{u}_x \\ \hat{u}_y \\ \hat{u}_z \end{bmatrix} = \begin{bmatrix} \hat{F}_x \\ \hat{F}_y \\ \hat{F}_z \end{bmatrix}, \tag{17}$$

where $\hat{F}_i = \hat{F}_i(\tilde{k}_1)$ is the total force in the i-direction from all strips, i.e. the same force acting on the slab in Eq. (12). It is assumed that the slab is rigid in the lateral direction. Further, continuity of vertical and axial displacements between the slab and the soil are assumed. Hence, $\hat{u}_y(\tilde{k}_1) = 0$, $\hat{u}_z(\tilde{k}_1) = \hat{u}_{\mathrm{s}}(\tilde{k}_1)$ and $\hat{u}_x(\tilde{k}_1) = \hat{w}_{\mathrm{s}}(\tilde{k}_1)$. These relationships are inserted into Eq. (12) that now constitutes a solvable system of equations. When the track displacements have been calculated, the individual strip forces can be obtained from $\hat{\mathbf{F}} = \hat{\tilde{\mathbf{H}}}^{-1}\hat{\mathbf{u}}$ and used for calculating the free-field soil surface response.

4.2. Finite element models: Models c) and d)

To account for the deformation of the slab in the cross-direction, finite elements are used for modeling the track in Models c) and d). The coordinate transformation in Eq. (2), when applied to the equations governing the FE formulations, introduces convective terms in the damping and stiffness matrices. The finite elements used for the track are described in Section 4.2.1. In Section 4.2.2, the coupling of the FE track to the soil is described.

4.2.1. Element equations for railway track

With the coordinate transformation in Eq. (2) and the partial derivative relations in Eq. (3), the Cauchy equation of motion can be written as

$$\tilde{\boldsymbol{\nabla}}^T \tilde{\boldsymbol{\sigma}} = \rho\Big(\frac{\partial^2 \tilde{\mathbf{u}}}{\partial t^2} - 2v\frac{\partial^2 \tilde{\mathbf{u}}}{\partial t \partial \tilde{x}_1} + v^2 \frac{\partial^2 \tilde{\mathbf{u}}}{\partial^2 \tilde{x}_1}\Big), \tag{18}$$

where the matrix differential operator $\tilde{\boldsymbol{\nabla}}$, the stress vector $\tilde{\boldsymbol{\sigma}}$ and the displacement vector $\tilde{\mathbf{u}}$ are defined as

$$\tilde{\boldsymbol{\nabla}}^T = \begin{bmatrix} \frac{\partial}{\partial \tilde{x}_1} & 0 & 0 & \frac{\partial}{\partial \tilde{x}_2} & \frac{\partial}{\partial \tilde{x}_3} & 0 \\ 0 & \frac{\partial}{\partial \tilde{x}_2} & 0 & \frac{\partial}{\partial \tilde{x}_1} & 0 & \frac{\partial}{\partial \tilde{x}_3} \\ 0 & 0 & \frac{\partial}{\partial \tilde{x}_3} & 0 & \frac{\partial}{\partial \tilde{x}_1} & \frac{\partial}{\partial \tilde{x}_2} \end{bmatrix}, \tag{19}$$

$$\tilde{\boldsymbol{\sigma}}^T = \begin{bmatrix} \tilde{\sigma}_{11} & \tilde{\sigma}_{22} & \tilde{\sigma}_{33} & \tilde{\sigma}_{12} & \tilde{\sigma}_{13} & \tilde{\sigma}_{23} \end{bmatrix}, \tag{20}$$

$$\tilde{\mathbf{u}}^T = \begin{bmatrix} \tilde{u}_1 & \tilde{u}_2 & \tilde{u}_3 \end{bmatrix}, \tag{21}$$

The weak form is obtained by multiplying Eq. (18) by an arbitrary weight function vector $\mathbf{g} = \mathbf{g}(\tilde{x}, \tilde{y}, \tilde{z})$ and integrating it over the region. The resulting weak form, after partial integration, becomes

$$\begin{aligned} \int_V (\tilde{\boldsymbol{\nabla}}\mathbf{g})^T \tilde{\boldsymbol{\sigma}}\, \mathrm{d}V + \rho \int_V \mathbf{g}^T \frac{\partial^2 \tilde{\mathbf{u}}}{\partial t^2}\, \mathrm{d}V - 2\rho\, v \int_V \mathbf{g}^T \frac{\partial^2 \tilde{\mathbf{u}}}{\partial t \partial \tilde{x}_1}\, \mathrm{d}V + \rho\, v^2 \int_S \mathbf{g}^T \frac{\partial \tilde{\mathbf{u}}}{\partial \tilde{x}_1}\, n_x\, \mathrm{d}S - \rho\, v^2 \int_V \frac{\partial \tilde{\mathbf{g}}}{\partial \tilde{x}_1}^T \frac{\partial \tilde{\mathbf{u}}}{\partial \tilde{x}_1}\, \mathrm{d}V \\ = \int_S \mathbf{g}^T \mathbf{t}\, \mathrm{d}S, \end{aligned} \tag{22}$$

where $\mathbf{t}$ is the traction vector.

To obtain the FE formulation, the displacements $\tilde{\mathbf{u}}(\tilde{x}, \tilde{y}, \tilde{z}, t)$ are approximated using the element nodal values $\mathbf{a}(t)$ and the shape functions $\mathbf{N}(\tilde{x}, \tilde{y}, \tilde{z})$ as $\tilde{\mathbf{u}} = \mathbf{N}\mathbf{a}$. Adopting the Galerkin method, the mass, damping and stiffness matrices, and the load vector, are identified as

$$\mathbf{K} = \int_V (\tilde{\boldsymbol{\nabla}}\mathbf{N})^T \mathbf{D} (\tilde{\boldsymbol{\nabla}}\mathbf{N})\, \mathrm{d}V \;\; - \rho v^2 \int_V \frac{\partial \mathbf{N}}{\partial \tilde{x}_1}^T \frac{\partial \mathbf{N}}{\partial \tilde{x}_1}\, \mathrm{d}V + \rho v^2 \int_S \mathbf{N}^T \frac{\partial \mathbf{N}}{\partial \tilde{x}_1} n_x\, \mathrm{d}S, \tag{23}$$

$$\mathbf{C} = -2\rho v \int_V \mathbf{N}^T \frac{\partial \mathbf{N}}{\partial \tilde{x}_1}\, \mathrm{d}V, \tag{24}$$

$$\mathbf{M} = \rho \int_V \mathbf{N}^T \mathbf{N}\, \mathrm{d}V, \tag{25}$$

$$\mathbf{f}_l = \int_S \mathbf{N}^T \tilde{\mathbf{t}}\, \mathrm{d}S, \tag{26}$$

where $\mathbf{D}$ is the constitutive matrix for isotropic elasticity. Similar derivations for the convective solid finite elements can be found in e.g. [14]. Analogously, convective terms in the stiffness and damping matrices are also obtained for the other element types. When the velocity v is set to zero, the equations reduce to the standard FE equations, whose derivations can be found in for example [18].

In Model c), the track slab is modeled using 4-node rectangular Kirchhoff shell elements with five degrees-of-freedom (DoFs) per node (three displacements and two rotations). In Model d), standard 8-node isoparametric brick elements with three displacement DoFs per node are used. In Models c) and d), 2-node Bernoulli-Euler beam

elements with two DoFs per node (vertical displacement and one rotation), are used for modeling the rails. The rail pads, i.e. the coupling between the rails and the slab, are modeled by visco-elastic interface elements representing continuous springs and dashpots. Here, the equations are derived for an interface element when the rail is parallel to the x-axis. Denoting the spring stiffness and dashpot coefficient by k and c, respectively, the loads on the rail and slab from the visco-elastic interface are written

$$q_{\mathrm{r}}(x,t) = -k(w_{\mathrm{r}} - w_{\mathrm{s}}) - c\Big(\frac{\partial w_{\mathrm{r}}}{\partial t} - \frac{\partial w_{\mathrm{s}}}{\partial t}\Big) = 0, \tag{27}$$

$$q_{\mathrm{s}}(x,y_r,t) = -k(w_{\mathrm{s}} - w_{\mathrm{r}}) - c\Big(\frac{\partial w_{\mathrm{s}}}{\partial t} - \frac{\partial w_{\mathrm{r}}}{\partial t}\Big) = 0, \tag{28}$$

where $w_{\mathrm{r}} = w_{\mathrm{r}}(x,t)$ is the deflection in the rail, and $w_{\mathrm{s}} = w_{\mathrm{s}}(x,y_r,t)$ is the deflection of the slab at the y-coordinate of the rail $y = y_{\mathrm{r}}$. With the coordinate transformation in Eq. (2) and the partial derivative relations in Eq. (3), these loads are obtained in the moving frame of reference as

$$\tilde{q}_{\mathrm{r}}(\tilde{x},t) = -k(\tilde{w}_{\mathrm{r}} - \tilde{w}_{\mathrm{s}}) - c\Big\{\Big(\frac{\partial \tilde{w}_{\mathrm{r}}}{\partial t} - \frac{\partial \tilde{w}_{\mathrm{s}}}{\partial t}\Big) - v\Big(\frac{\partial \tilde{w}_{\mathrm{r}}}{\partial \tilde{x}} - \frac{\partial \tilde{w}_{\mathrm{s}}}{\partial \tilde{x}}\Big)\Big\}, \tag{29}$$

$$\tilde{q}_{\mathrm{s}}(\tilde{x},t) = -k(\tilde{w}_{\mathrm{s}} - \tilde{w}_{\mathrm{r}}) - c\Big\{\Big(\frac{\partial \tilde{w}_{\mathrm{s}}}{\partial t} - \frac{\partial \tilde{w}_{\mathrm{r}}}{\partial t}\Big) - v\Big(\frac{\partial \tilde{w}_{\mathrm{s}}}{\partial \tilde{x}} - \frac{\partial \tilde{w}_{\mathrm{r}}}{\partial \tilde{x}}\Big)\Big\}. \tag{30}$$

The displacements of the rail, $w_{\mathrm{r}}(\tilde{x})$ are approximated using the beam element shape functions $\mathbf{N}_{\mathrm{r}}(\tilde{x})$ and the element nodal displacements $\mathbf{a}_{\mathrm{r}}(t)$. Likewise, the slab displacements $w_{\mathrm{s}}(\tilde{x},\tilde{y}_{\mathrm{r}})$ are approximated using the shell or solid ellement shape functions $\mathbf{N}_{\mathrm{s}}(\tilde{x},\tilde{y})$ evaluated at $\tilde{y} = \tilde{y}_{\mathrm{r}}$, and the element nodal displacements $\mathbf{a}_{\mathrm{s}}(t)$. By equating the forces acting on the rail and slab to the internal forces of the interface element, the following expressions are obtained for the interface element stiffness and damping matrices:

$$\begin{aligned}\mathbf{K} = k\Big\{ &\textstyle\int_{-L/2}^{L/2} \tilde{\mathbf{N}}_u^T\tilde{\mathbf{N}}_u \,\mathrm{d}\tilde{x} + \int_{-L/2}^{L/2} \tilde{\mathbf{N}}_l^T\tilde{\mathbf{N}}_l \,\mathrm{d}\tilde{x} - \int_{-L/2}^{L/2} \tilde{\mathbf{N}}_u^T\tilde{\mathbf{N}}_l \,\mathrm{d}\tilde{x} - \int_{-L/2}^{L/2} \tilde{\mathbf{N}}_l^T\tilde{\mathbf{N}}_u \,\mathrm{d}\tilde{x} \Big\} \\ -cv\Big\{ &\textstyle\int_{-L/2}^{L/2} \tilde{\mathbf{N}}_u^T \frac{\mathrm{d}\tilde{\mathbf{N}}_u}{\mathrm{d}\tilde{x}} \,\mathrm{d}\tilde{x} + \int_{-L/2}^{L/2} \tilde{\mathbf{N}}_l^T \frac{\mathrm{d}\tilde{\mathbf{N}}_l}{\mathrm{d}\tilde{x}} \,\mathrm{d}\tilde{x} - \int_{-L/2}^{L/2} \tilde{\mathbf{N}}_u^T \frac{\mathrm{d}\tilde{\mathbf{N}}_l}{\mathrm{d}\tilde{x}} \,\mathrm{d}\tilde{x} - \int_{-L/2}^{L/2} \tilde{\mathbf{N}}_l^T \frac{\mathrm{d}\tilde{\mathbf{N}}_u}{\mathrm{d}\tilde{x}} \,\mathrm{d}\tilde{x} \Big\},\end{aligned} \tag{31}$$

$$\mathbf{C} = c\Big\{ \int_{-L/2}^{L/2} \tilde{\mathbf{N}}_u^T\tilde{\mathbf{N}}_u \,\mathrm{d}\tilde{x} + \int_{-L/2}^{L/2} \tilde{\mathbf{N}}_l^T\tilde{\mathbf{N}}_l \,\mathrm{d}\tilde{x} - \int_{-L/2}^{L/2} \tilde{\mathbf{N}}_u^T\tilde{\mathbf{N}}_l \,\mathrm{d}\tilde{x} - \int_{-L/2}^{L/2} \tilde{\mathbf{N}}_l^T\tilde{\mathbf{N}}_u \,\mathrm{d}\tilde{x} \Big\}, \tag{32}$$

where the vectors $\tilde{\mathbf{N}}_u$ and $\tilde{\mathbf{N}}_l$ collect the shape functions for both the rail and the slab as

$$\tilde{\mathbf{N}}_u(\tilde{x}) = \Big[\mathbf{N}_{\mathrm{r}}(\tilde{x}) \quad 0 \times \mathbf{N}_{\mathrm{s}}(\tilde{x},\tilde{y} = \tilde{y}_{\mathrm{r}})\Big], \qquad \tilde{\mathbf{N}}_l(\tilde{x}) = \Big[0 \times \mathbf{N}_{\mathrm{r}}(\tilde{x}) \quad \mathbf{N}_{\mathrm{s}}(\tilde{x},\tilde{y} = \tilde{y}_{\mathrm{r}})\Big] \tag{33}$$

Following standard FE assembly, the equations of motion for the track structure can be written as

$$\mathbf{M}_{\mathrm{t}}\ddot{\tilde{\mathbf{u}}}_{\mathrm{t}} + \mathbf{C}_{\mathrm{t}}\dot{\tilde{\mathbf{u}}}_{\mathrm{t}} + \mathbf{K}_{\mathrm{t}}\tilde{\mathbf{u}}_{\mathrm{t}} = \tilde{\mathbf{f}}_{\mathrm{t}}, \tag{34}$$

where $\mathbf{M}_{\mathrm{t}}$, $\mathbf{C}_{\mathrm{t}}$ and $\mathbf{K}_{\mathrm{t}}$ is the total mass, damping and stiffness matrix, respectively, of the complete track structure. Further, $\tilde{\mathbf{u}}_{\mathrm{t}}$ and $\tilde{\mathbf{f}}_{\mathrm{t}}$ is the displacement and force vector for the complete track structure, respectively, in the moving frame of reference.

4.2.2. Coupling of finite element track to soil

Assuming steady-state conditions, the governing equation for the railway track structure can be written as

$$(-\omega^2\mathbf{M}_\mathrm{t} + \mathrm{i}\omega\mathbf{C}_\mathrm{t} + \mathbf{K}_\mathrm{t})\tilde{\mathbf{u}}_\mathrm{t} = \mathbf{D}_\mathrm{t}\tilde{\mathbf{u}}_\mathrm{t} = \tilde{\mathbf{f}}_\mathrm{t}, \tag{35}$$

where ω is the circular frequency of vibration in the moving frame of reference and the dynamic stiffness matrix of the track is $\mathbf{D}_\mathrm{t} = (-\omega^2\mathbf{M}_\mathrm{t} + \mathrm{i}\omega\mathbf{C}_\mathrm{t} + \mathbf{K}_\mathrm{t})$.

The track is coupled to a dynamic stiffness matrix representing the soil. This dynamic stiffness matrix is derived from the previously described Green's function for a horizontally layered visco-elastic half-space. The soil response is calculated for a unit load on the soil surface. The unit load is applied with uniform traction over a rectangular area, the size of which equals the element size in the connecting superstructure. Considering an element size of $2a \times 2b$, in the x_1- and x_2-direction, respectively, the traction p_j for a load in direction j is

$$p_j(\tilde{x}, \tilde{y}, \omega) = \begin{cases} 1/(4ab), & -a < \tilde{x} < a,\ -b < \tilde{y} < b \\ 0, & \text{otherwise} \end{cases}. \tag{36}$$

In wavenumber domain the traction becomes

$$\hat{p}_j(\tilde{k}_1, \tilde{k}_2, \omega) = \frac{\sin(\tilde{k}_1 a)}{\tilde{k}_1 a}\frac{\sin(\tilde{k}_2 b)}{\tilde{k}_2 b}. \tag{37}$$

The soil response is calculated for three load cases, with the unit load acting in the $\tilde{x}$-, $\tilde{y}$- and $\tilde{z}$-directions, respectively. From these three load cases, a dynamic flexibility matrix $\mathbf{C}_\mathrm{s}(\omega, v)$ is established for a set of DoFs where the superstructure interacts with the soil surface. These DoFs will be referred to as soil–structure interaction (SSI) DoFs. The flexibility matrix is then inverted to form the dynamic stiffness matrix of the soil, $\mathbf{D}_\mathrm{s}(\omega, v) = \mathbf{C}_\mathrm{s}^{-1}(\omega, v)$, which gives a relation between the steady-state displacements $\tilde{\mathbf{u}}_\mathrm{s}$ and forces $\tilde{\mathbf{f}}_\mathrm{s}$ for the SSI DoFs, at a certain load circular frequency ω and velocity v, as

$$\mathbf{D}_\mathrm{s}\,\tilde{\mathbf{u}}_\mathrm{s} = \tilde{\mathbf{f}}_\mathrm{s}. \tag{38}$$

The track and soil are coupled in a standard FE manner, and a global system of equations for the soil and the railway structure is formed by combining Eqs. (35) and (38), yielding

$$\mathbf{D}_\mathrm{g}\tilde{\mathbf{u}}_\mathrm{t} = \tilde{\mathbf{f}}_\mathrm{t}, \tag{39}$$

where $\mathbf{D}_\mathrm{g}$ represents the global dynamic stiffness matrix for the track structure and the soil.

The free-field response is calculated in a two-step procedure. The first step involves calculating the displacements in the slab–soil interface due to the moving load on the track by solving Eq. (39). The corresponding forces on the soil surface, $\tilde{\mathbf{f}}_\mathrm{s}$, are calculated by Eq. (38). In the second step, the free-field response due to these forces is calculated. A flexibility matrix $\mathbf{C}_{\mathrm{s,f}}(\omega, v)$ is established expressing the displacements in free-field due to forces on the soil–structure interface, i.e. the SSI DoFs, again using the previously described unit loadcases. The free-field

displacements, $\tilde{\mathbf{u}}_\mathrm{f}$, are then calculated as

$$\tilde{\mathbf{u}}_\mathrm{f} = \mathbf{C}_{\mathrm{s,f}}\tilde{\mathbf{f}}_\mathrm{s}. \tag{40}$$

These free-field displacements are obtained in the frame of reference of the moving load. The response is in steady-state with the frequency of the harmonic load.

5. Results from numerical studies

In Section 5.1, the free-field vertical response obtained from the different models when disregarding any in-plane interaction between the slab and the soil is presented. Section 5.2 contains the corresponding results when in-plane slab–soil interaction is accounted for. Finally, in Section 5.3, a vehicle model is introduced to calculate the wheel–rail contact forces as the vehicle runs over an uneven rail.

5.1. Free-field displacements assuming only vertical slab–soil interaction

To compare the free-field response obtained from the different models, the vertical displacement is extracted for points along a line parallel with the track, as illustrated in Figure 3. The displacements are calculated in the coordinate system following the moving load, meaning that $\tilde{x} = 0$ corresponds to a point perpendicular to the moving load. Positive $\tilde{x}$-values correspond to points ahead of the load.

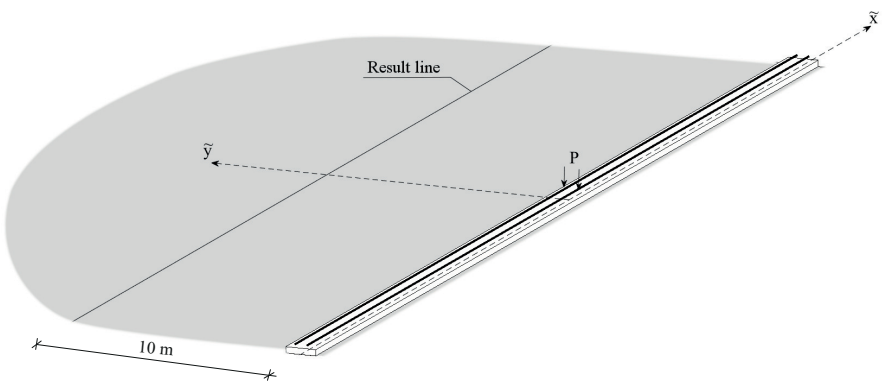

Figure 3: Illustration of the result line in relation to the moving load. The response is calculated in the moving frame of reference, along a line located 10 m from the track centerline.

The response along a line located 10 m from the track center line, as obtained with the different models when only accounting for the vertical interaction between the slab and the soil, for a unit load moving along the track at $v = 30$ m/s are shown in Figures 4–6 for the excitation frequencies $f = 40$ Hz, $f = 60$ Hz and $f = 80$ Hz, respectively. For these frequencies, the Rayleigh wavelength for the stiffer soil is $\lambda = 6.5$ m ($\sim$ twice the slab width), $\lambda = 4.3$ m and $\lambda = 3.3$ m (similar to the slab width), respectively. For the softer soil, these frequencies correspond to Rayleigh wavelengths $\lambda = 3.3$ m (similar to the slab width), $\lambda = 2.2$ m and $\lambda = 1.6$ m ($\sim$ half the slab width), respectively. These frequencies are selected to demonstrate the features of the different modeling strategies. Condensed results for the frequency range (5–80 Hz) are shown in the next subsection. Subfigures (a)

and (b) show the response of the softer soil for the thin and thick slab, respectively, whereas (c) and (d) show the corresponding results for the stiffer soil. The response along a line located at a greater distance (25 m) from the track has also been studied, but these results are not presented here because they show the same general differences as obtained for the shorter distance.

As expected, Models c) and d) yield almost indistinguishable results for both slab thicknesses and both soil types in the entire frequency range. In the following discussion, these responses are considered accurate. For low frequencies, the different slab–soil interface conditions implied by the different modeling strategies have virtually no effect on the free-field response. This is because, for low frequencies, the wavelength of the fundamental Rayleigh wave that dominates the response, is long compared to the width of the slab.

At 40 Hz (see Figure 4), the response obtained assuming a constant slab–soil pressure in the slab cross direction, Model a), is significantly underestimated for both slabs on soft soil, as seen in subfigures (a) and (b). In the case of a thick slab, the response obtained assuming a constant displacement under the slab in the cross-direction, Model b), is almost indistinguishable from that obtained with Models c) and d), see subfigure (b). However, this is not the case for the thinner slab, see subfigure (a), where also Model b) produces a slightly underestimated response. The absolute value of the slab–soil pressure distributions directly under the load for $f = 40$ Hz are shown in Figure 7 for the different models. For the thin slab, the presence of the rails is visible as local peaks in the contact pressure obtained using Models c) and d). In addition, the high contact pressures around the slab edges, obtained by enforcing rigidity in the cross-direction using Model b), are not present for the thin slab when the cross-direction flexibility is accounted for, as in Models c) and d). For the thick slab, however, the true pressure distribution approaches that of a rigid slab and hence the free-field response levels are also almost identical. For the stiffer soil, the Rayleigh wavelength is approximately twice the slab width at 40 Hz. For such a wavelength to slab width ratio, the uniform pressure produces higher vibrations than the pressure distribution obtained with a rigid surface, c.f. Figure 4 (c) and (d). The soil is even slightly more responsive to the "true" pressure distribution obtained for the thin slab, with lower edge pressures and instead having a higher overall pressure in the center of the slab, see Figure 4 (c) and Figure 7 (c).

At higher frequencies, Model a) yield an underestimated response for both slab thicknesses and soil types, see Figures 5–6. For the thin slab and soft soil, the response obtained from Model b) is overestimated for frequencies with a fundamental Rayleigh wavelength shorter than the slab width. For the stiff soil, the wavelength of the fundamental Rayleigh wave is longer than the slab width in the entire studied frequency range, and assuming a rigid slab in the cross direction yields an underestimated response for the thin slab, but an accurate response for the thick slab. The differences in the slab–soil contact pressures, obtained with the Models a) – d), are similar to those discussed above for $f = 40$ Hz, and are therefore not shown here for the higher frequencies.

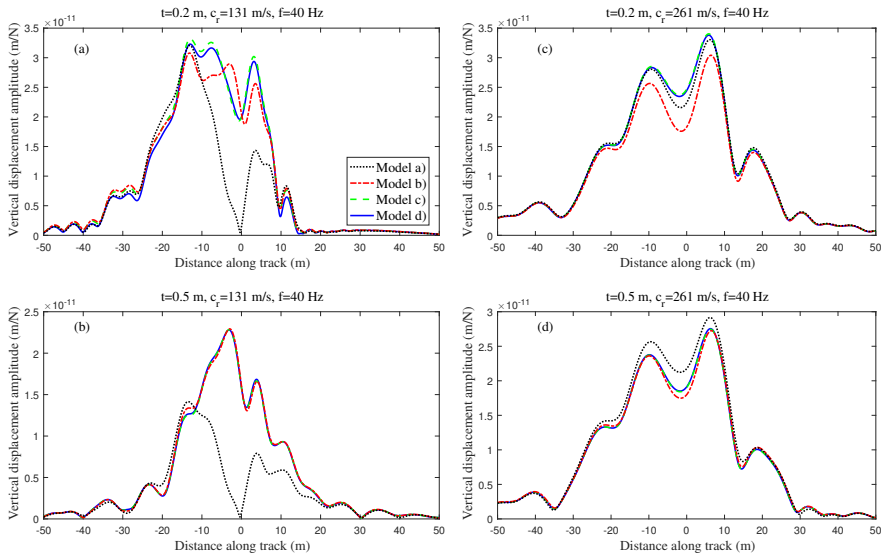

Figure 4: Maximum free-field displacement 10 m from the track center line, due to a unit harmonic load at $f = 40$ Hz moving along the track at $v = 30$ m/s, as obtained with Models a) – d), accounting only for vertical interaction between slab and soil. Figures (a) and (b) are for the thin and thick slab, respectively, on the softer soil. Figures (c) and (d) are the corresponding results for the stiffer soil.

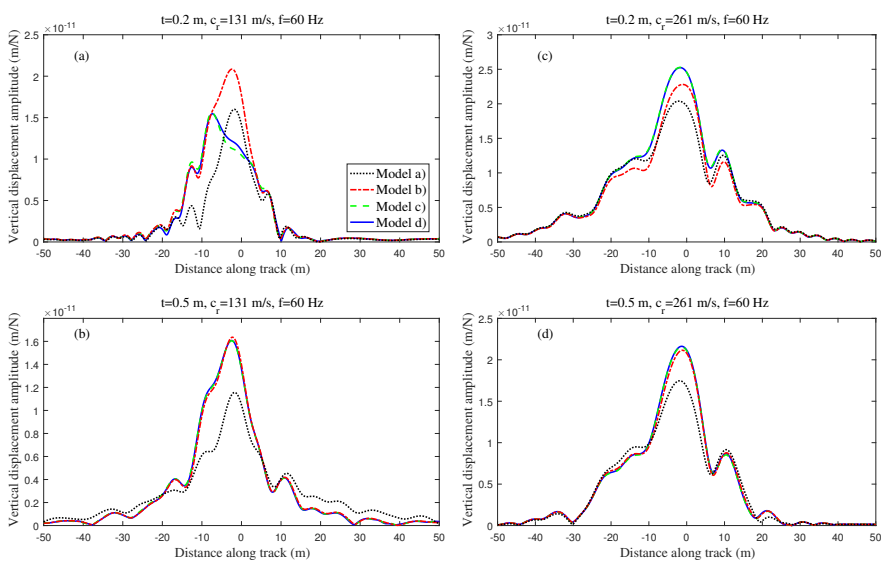

Figure 5: Maximum free-field displacement 10 m from the track center line, due to a unit harmonic load at $f = 60$ Hz moving along the track at $v = 30$ m/s, as obtained with Models a) – d), accounting only for vertical interaction between slab and soil. Figures (a) and (b) are for the thin and thick slab, respectively, on the softer soil. Figures (c) and (d) are the corresponding results for the stiffer soil.

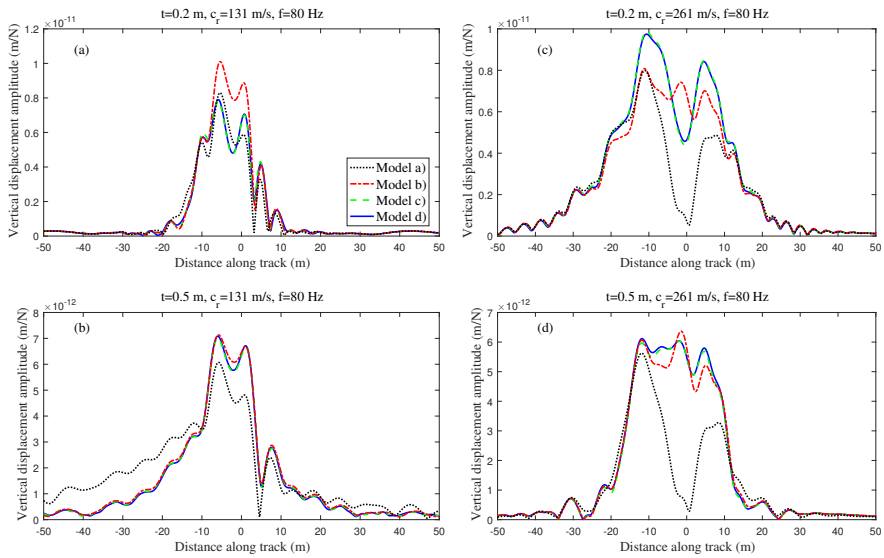

Figure 6: Maximum free-field displacement 10 m from the track center line, due to a unit harmonic load at $f = 80$ Hz moving along the track at $v = 30$ m/s, as obtained with Models a) – d), accounting only for vertical interaction between slab and soil. Figures (a) and (b) are for the thin and thick slab, respectively, on the softer soil. Figures (c) and (d) are the corresponding results for the stiffer soil.

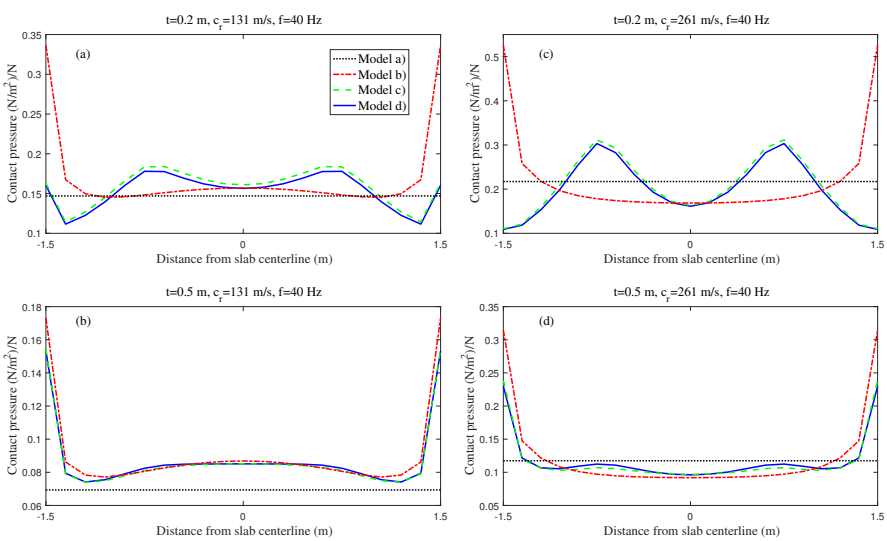

Figure 7: Vertical slab–soil contact pressure directly under the unit harmonic load at $f = 40$ Hz moving along the track at $v = 30$ m/s, as obtained with Models a) – d). Figures (a) and (b) are for the thin and thick slab, respectively, on the softer soil. Figures (c) and (d) are the corresponding results for the stiffer soil.

5.2. Free-field displacements including in-plane slab–soil interaction

When the in-plane slab–soil displacements are coupled, shear forces arise in the interface. These shear forces also affect the vertical vibration levels in the free field. The maximum vertical displacement along a line located 10 m from the track center line, for a unit load moving along the track at $v = 30$ m/s, are shown in Figures 8–10 for the Models b) – d) when in-plane interaction between the slab and soil is enforced. The excitation frequencies for which the response is shown are again $f = 40$ Hz, $f = 60$ Hz and $f = 80$ Hz, respectively.

The effects of in-plane slab–soil interaction on the vertical response levels are most noticeable around the frequencies for which the wavelength of the Rayleigh wave in the soil is similar to the slab width, see Figure 8 (a)–(b) (c.f. Figure 4) and Figure 10 (c)–(d) (c.f. Figure 6). The influence of the in-plane slab–soil interaction is complex, as it introduces shear forces on the soil surface that also change the vertical interaction forces, both of which effects influence the free-field response.

As all models are established in the moving frame of reference, following the load at the given velocity $v = 30$ m/s, the results are also obtained in this reference frame. Hence, to obtain the response of a fixed point, the receiver is moved through the model in the opposite travel direction of the load, yielding a transient time-history of the displacement response. The transient response contains a wide range of frequencies due to the Doppler effect. The time derivative of the fixed point displacement time-history yields the fixed point particle velocity. To efficiently compare the free-field responses for a range of excitation frequencies, two measures are used here. The first measure is the fixed point maximum vertical particle velocity. The second measure is the energy of the velocity time-history signal, calculated as

$$E_{\dot{u}_f} = \int_{-\infty}^{\infty} |\dot{u}_f(t)|^2 \mathrm{d}t \tag{41}$$

where $\dot{u}_f(t)$ is the vertical velocity time-history response for a fixed point, due to the moving unit load with frequency f.

The maximum vertical particle velocities and the signal energies $E_{\dot{u}_f}$ obtained from the different models are shown in Figure 11 and Figure 13, respectively, for a fixed point 10 m from the track. The results in Figure 11 and Figure 13 are normalized to the response obtained with Model d), and shown in Figure 12 and Figure 14, respectively. In these figures, the response from the different models when the in-plane slab–soil interaction was disregarded, is also shown for reference.

It can be seen in Figure 12 and Figure 14 that for the cases studied here, the predicted vertical free-field response is in general significantly higher when in-plane slab–soil interaction is accounted for and that its effects are equally significant for both the thick and the thin slab on both soil types. Disregarding the in-plane slab–soil interaction yields an underestimation of the peak particle vertical velocity and the vertical velocity signal energy, of as much as 30% and 50% respectively, c.f. the gray/blue solid lines in Figure 12 and Figure 14. Model c) (shell elements) yields similar vibration levels as Model d) (solid elements) for both slab thicknesses on both soils, both in terms of maximum particle velocity and velocity signal energy. When in-plane slab–soil interaction was disregarded, the two models provided almost indistinguishable results. When the in-plane interaction is included, the differences

increase. In Model c) the mid-section is located in the plane of the soil surface, i.e. the membrane and bending behaviors of the shell elements are decoupled. Furthermore, whereas the model with solid elements enables the slab lower surface to deform differently than the upper surface, the shell elements necessarily engage the entire thickness of the slab. Similarly, the axial and bending behaviors of the beam representing the slab in Model b) are also decoupled. For the thick slab, the response levels obtained with Model b) are about as accurate as those from Model c), and within about $\pm 10\%$ of those obtained with Model d).

The maximum vibration levels, both in terms of peak vertical particle velocity and velocity signal energy, occur around 25–30 Hz for the softer soil and around 50–55 Hz for the stiffer soil. For these frequencies, the Rayleigh wavelength is slightly shorter than twice the slab width. Further, it can be seen that the thicker slab yields significantly lower vibration levels.

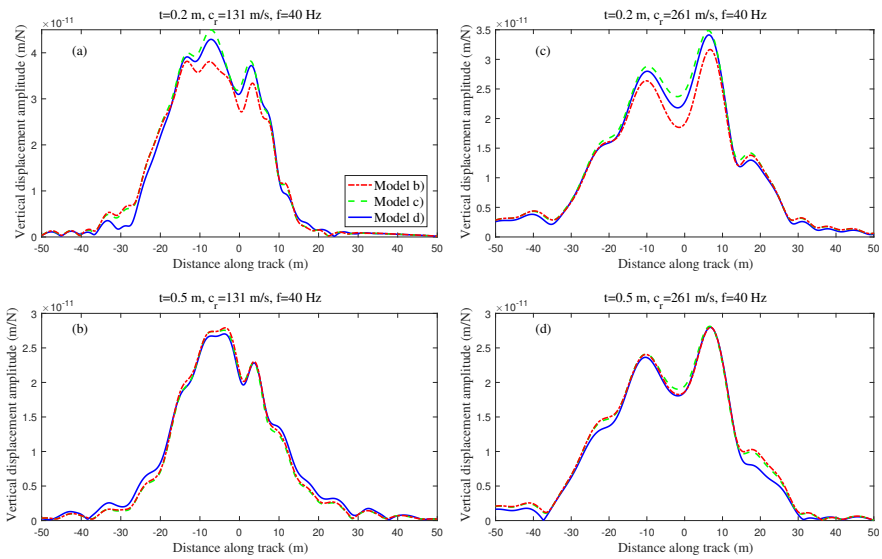

Figure 8: Maximum free-field displacement 10 m from the track center line, due to a unit harmonic load at $f = 40$ Hz moving along the track at $v = 30$ m/s, as obtained with Models b) – d), accounting for in-plane slab–soil interaction. Figures (a) and (b) are for the thin and thick slab, respectively, on the softer soil. Figures (c) and (d) are the corresponding results for the stiffer soil.

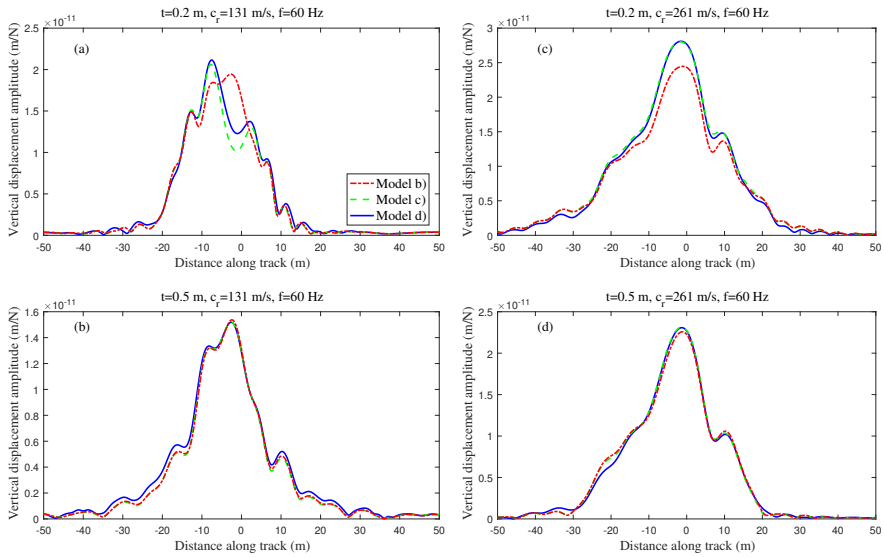

Figure 9: Maximum free-field displacement 10 m from the track center line, due to a unit harmonic load at $f = 60$ Hz moving along the track at $v = 30$ m/s, as obtained with Models b) – d), accounting for in-plane slab–soil interaction. Figures (a) and (b) are for the thin and thick slab, respectively, on the softer soil. Figures (c) and (d) are the corresponding results for the stiffer soil.

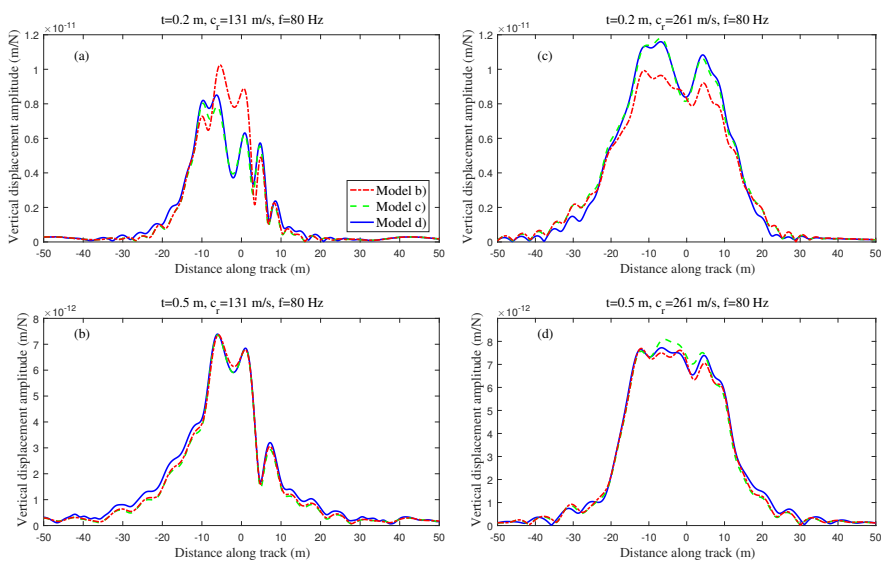

Figure 10: Maximum free-field displacement 10 m from the track center line, due to a unit harmonic load at $f = 80$ Hz moving along the track at $v = 30$ m/s, as obtained with Models b) – d), accounting for in-plane slab–soil interaction. Figures (a) and (b) are for the thin and thick slab, respectively, on the softer soil. Figures (c) and (d) are the corresponding results for the stiffer soil.

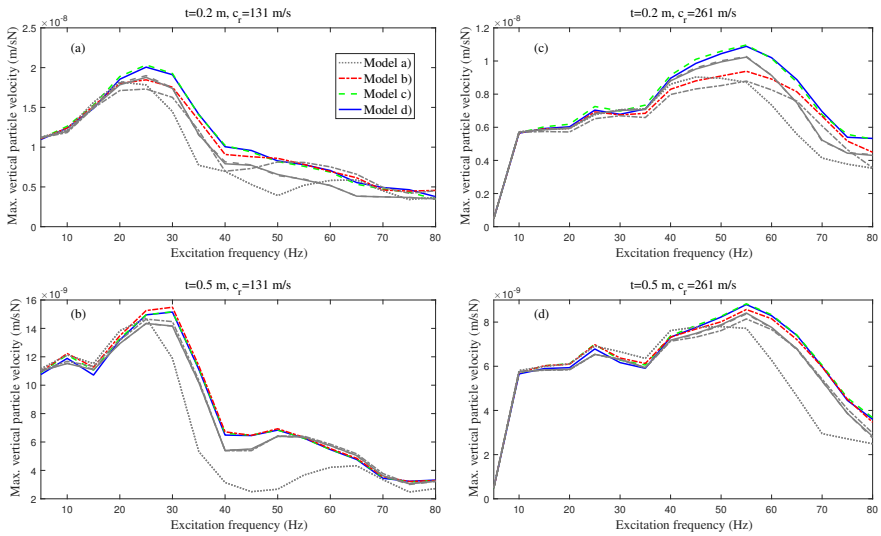

Figure 11: Maximum particle vertical velocity in a fixed point 10 m from the track center line, due to a unit harmonic load moving along the track at $v = 30$ m/s, as obtained with Models a) – d). Figures (a) and (b) are for the thin and thick slab, respectively, on the softer soil. Figures (c) and (d) are the corresponding results for the stiffer soil. Curves in gray are without accounting for in-plane slab–soil interaction.

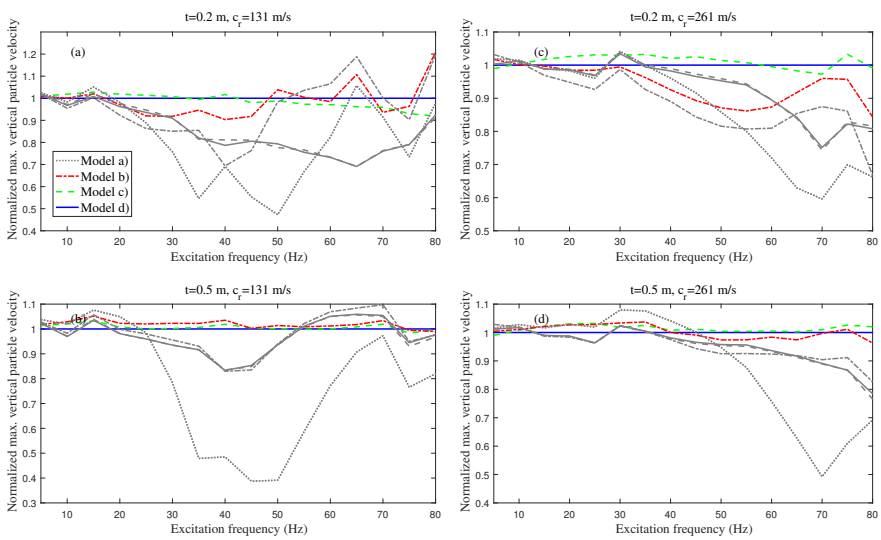

Figure 12: Normalized maximum particle vertical velocity in a fixed point 10 m from the track center line, due to a unit harmonic load moving along the track at $v = 30$ m/s, as obtained with Models a) – d). The curves are normalized against Model d). Figures (a) and (b) are for the thin and thick slab, respectively, on the softer soil. Figures (c) and (d) are the corresponding results for the stiffer soil. Curves in gray are without accounting for in-plane slab–soil interaction.

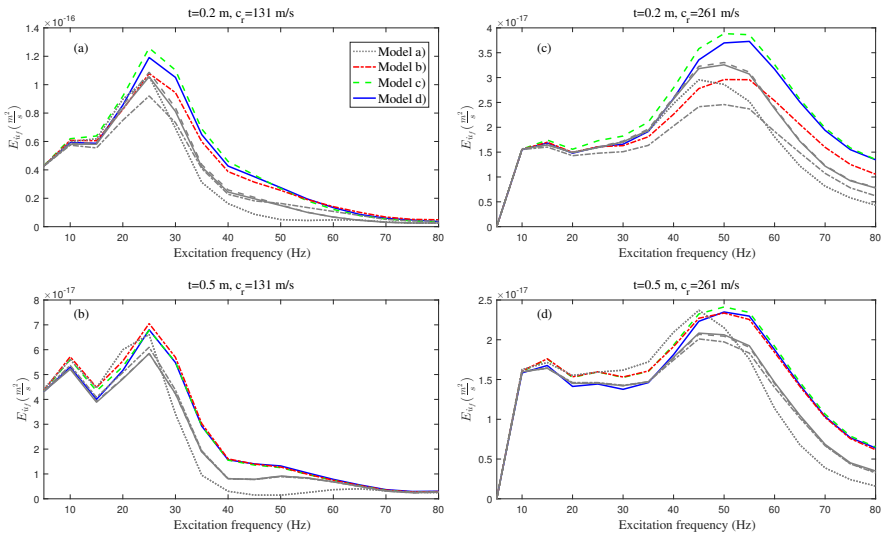

Figure 13: Vertical velocity signal energy in a fixed point 10 m from the track center line, due to a unit harmonic load moving along the track at $v = 30$ m/s, as obtained with Models a) – d). Figures (a) and (b) are for the thin and thick slab, respectively, on the softer soil. Figures (c) and (d) are the corresponding results for the stiffer soil. Curves in gray are without accounting for in-plane slab–soil interaction.

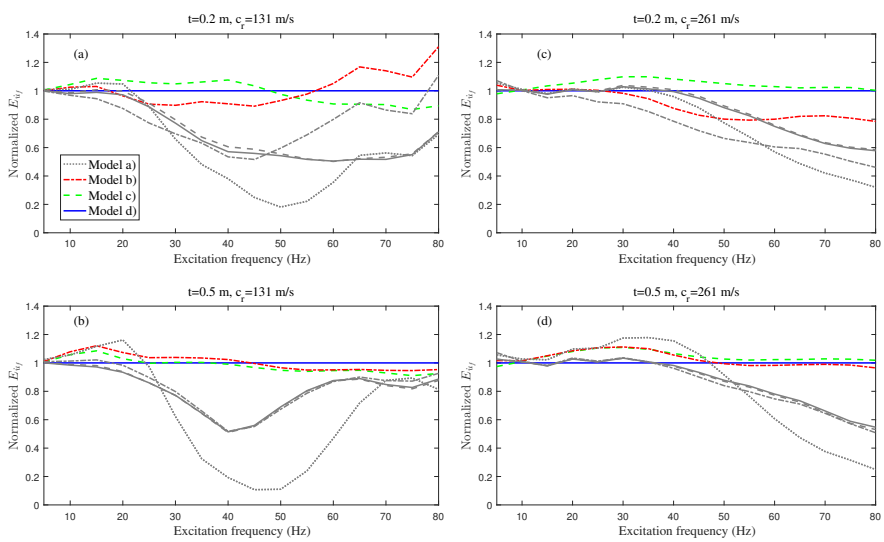

Figure 14: Normalized vertical velocity energy in a fixed point 10 m from the track center line, due to a unit harmonic load moving along the track at $v = 30$ m/s, as obtained with Models a) – d). The curves are normalized against Model d). Figures (a) and (b) are for the thin and thick slab, respectively, on the softer soil. Figures (c) and (d) are the corresponding results for the stiffer soil. Curves in gray are without accounting for in-plane slab–soil interaction.

5.3. Rail receptance and wheel–rail interaction force

In the previous subsections the differences between the different modeling strategies, regarding the free-field response due to a moving unit load, have been presented. However, when a vehicle runs over an uneven rail, the dynamic forces between the wheels and the rail depend on the rail receptance (displacement per unit force). Hence, models providing different rail receptances will also provide different wheel–rail interaction forces. The absolute values of the loading point receptance, as obtained with the different models are shown in Figure 15, for a load velocity of $v = 30$ m/s. The receptance is slightly higher for the cases with a thin slab than with a thick slab, c.f. subfigures (a) and (b) for the soft soil and subfigures (c) and (d) for the stiff soil. Further, the softer soil provides a higher rail point receptance than the stiffer soil. The in-plane slab–soil interaction has a negligible effect ($< 2\%$) on the rail receptance for the cases studied here. In Figure 15, the values shown for Models b) – d) were calculated with in-plane slab–soil interaction taken into account.

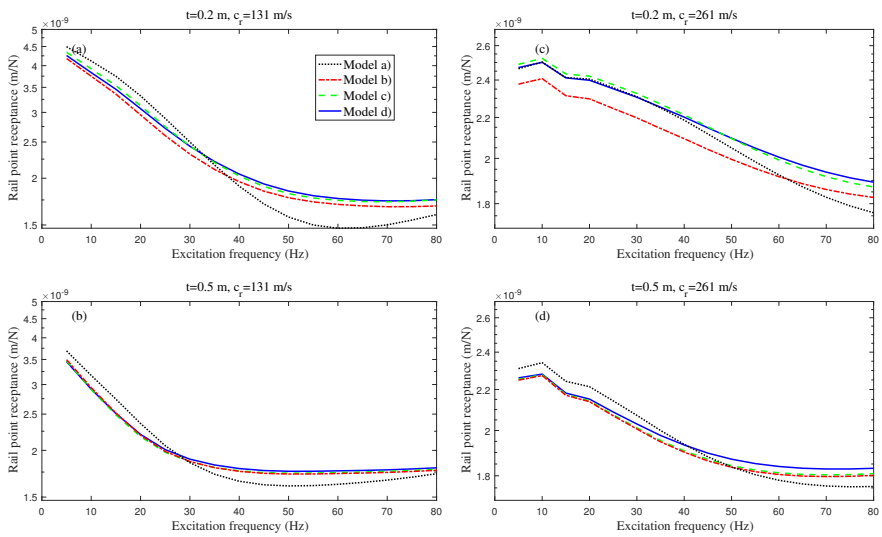

Figure 15: Rail loading point receptance, due to a unit harmonic load moving along the track at $v = 30$ m/s, as obtained with Models a) – d). Figures (a) and (b) are for the thin and thick slab, respectively, on the softer soil. Figures (c) and (d) are the corresponding results for the stiffer soil.

For each studied case, the different models yield similar values of the receptance, however some differences can be discerned. Models c) and d) provide almost identical rail receptances, with a maximum difference of less than 2%. Models a) and b) do not account for the slab flexibility in the cross-direction and overestimate the stiffness in that sense, since the entire track cross-section is forced to move uniformly. Model b) is seen to provide a slight underestimation of the receptance in the entire frequency span, with a maximum underestimation of about 5%, compared to Model d), in the cases involving the thin slab. The differences between Models a) and b) are only due to the different slab–soil interface conditions, and the receptance obtained with Model a) deviates by approximately $\pm 10\%$ compared to Model d).

The rail receptances for a given load speed are used for calculating the wheel–rail contact forces due to a vehicle running over an uneven rail. For a real vehicle with multiple axles, the receptances ahead and behind the loading points are required to set up a compliance matrix containing all the wheel–rail contact points. Here, however, a single axle vehicle is considered and thus only the receptance in the loading point is needed. The vehicle model is shown in Figure 16, and its properties, taken from [20], are shown in Table 3. The vehicle model consists of the sprung/unsprung masses m_s and m_w, and a suspension defined by the spring stiffness k_s and k_s' and the damper c_s.

For a given circular frequency of excitation $\omega = 2\pi f$ the dynamic stiffness of the vehicle can be written as

$$\mathbf{D_v} = \begin{bmatrix} \omega^2 m_u + \mathrm{i}\omega c_s + k_s & -k_s & -\mathrm{i}\omega c_s \\ -k_s & \omega^2 m_s + k_s + k_s' & -k_s' \\ -\mathrm{i}\omega c_s & -k_s' & \mathrm{i}\omega c_s + k_s' \end{bmatrix}, \tag{42}$$

with the corresponding displacement vector

$$\mathbf{u_v} = \begin{bmatrix} u_w \\ u_s \\ u_d \end{bmatrix}. \tag{43}$$

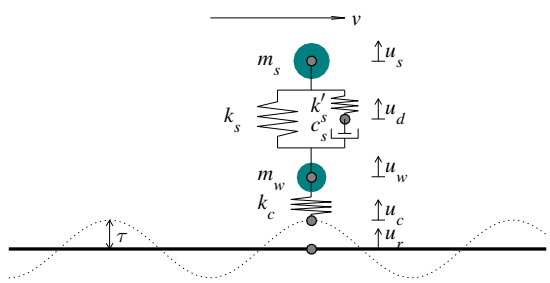

Figure 16: Single-axle vehicle moving with fixed speed v on rail with unevenness magnitude τ.

Table 3: Vehicle properties [20].

Parameter	Value
m_s (kg)	19 250
m_u (kg)	1750
k_s (N/m)	2.66×10^6
c_s (Ns/m)	3.5×10^4
k_s' (N/m)	3×10^6
k_c (N/m)	2.7×10^9

In the present study, a unit height of 0.1 mm is used for each studied unevenness wavelength. The excitation frequency and the unevenness wavelength are related through the vehicle speed as $f = v/\lambda$. A linearized Hertzian contact spring, with stiffness k_c, accounts for the wheel–rail contact. The contact spring is assembled between the wheel and a contact point on the rail. For a given frequency of excitation, the displacement of the contact point can be written as $u_c = u_r + \tau$, where u_r is the rail displacement and τ describes the the unevenness magnitude. The rail dynamic stiffness d_r at DoF u_r is the inverse of the complex valued point receptance. By eliminating the DoF u_c, the following system of equations is obtained,

$$\begin{bmatrix} \omega^2 m_u + \mathrm{i}\omega c_s + k_s + k_c & -k_s & -\mathrm{i}\omega c_s & -k_c \\ -k_s & \omega^2 m_s + k_s + k_s' & -k_s' & 0 \\ -\mathrm{i}\omega c_s & -k_s' & \mathrm{i}\omega c_s + k_s' & 0 \\ -k_c & 0 & 0 & d_r + k_c \end{bmatrix} \begin{bmatrix} u_w \\ u_s \\ u_d \\ u_r \end{bmatrix} = \begin{bmatrix} k_c\tau \\ 0 \\ 0 \\ -k_c\tau \end{bmatrix}. \tag{44}$$

The force in the contact spring is then simply $k_c(u_w - u_c) = k_c(u_w - u_r - \tau)$. Figure 17 shows the absolute value of the wheel–rail contact force, as a function of excitation frequency, for the different models. All models provide similar contact forces, the differences being of the same order of magnitude as the differences in the loading point receptance.

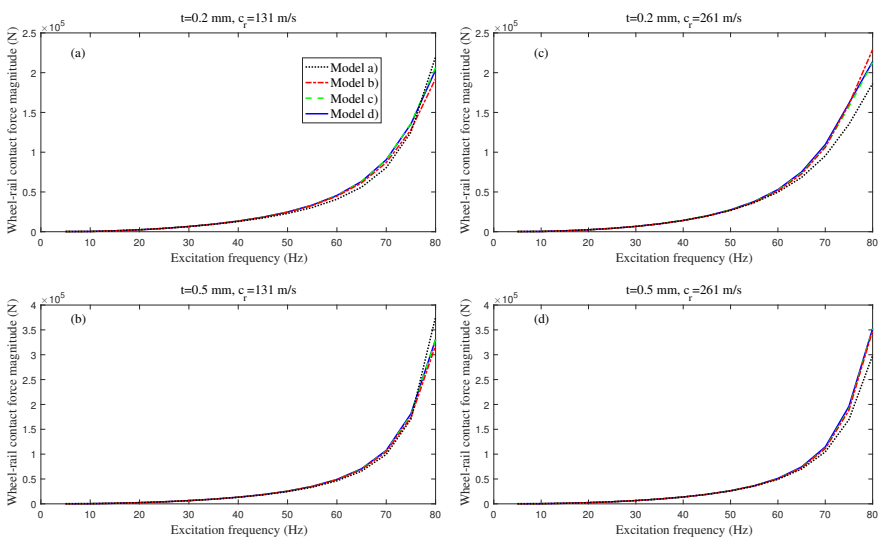

Figure 17: Absolute value of wheel–rail contact force at different excitation frequencies, $f = v/\lambda$ due to the single-axle vehicle moving along the track at $v = 30$ m/s over a harmonic unevenness of 0.1 mm. Figures (a) and (b) are for the thin and thick slab, respectively, on the softer soil. Figures (c) and (d) are the corresponding results for the stiffer soil.

6. Conclusions

In the paper, four different modeling strategies with respect to assumptions about the slab track cross-section behavior and the track–soil interface conditions, have been compared by calculating the vertical free-field response to a unit harmonic load moving along the track at a fixed speed. In the most general model used here, the slab is represented by 3D solid elements, and the response from this model is used as a reference to which the other models are compared. Two different slab thicknesses have been studied, on two stratifications with different stiffness of the top soil layer. Although the free-field response has been presented here only for a point 10 m from the track, the response further from the track has also been studied, and the same general conclusions apply also for those cases.

It has been found that for a thin slab, the pressure distribution under the slab due to load on the rails is highly influenced by the slab cross-direction flexibility, and this in turn has a large effect on the predicted free-field vibrations. As expected, this pressure distribution and the resulting free-field vibrations, calculated with a solid continuum model (Model d), are predicted equally well with a computationally cheaper shell element model (Model c). However, the two beam models, assuming constant slab–soil contact pressure (Model a) or constant cross-direction displacement (Model b), yield significantly different responses due to the inadequately assumed slab–soil pressure distributions. For the thicker slab, the cross-direction slab flexibility is very low and the pressure distribution under the slab due to a load on the rails, approaches that of a rigid slab. In that case, the beam model assuming constant cross-direction displacement (Model b) yields accurate results.

Further, it has been found that if full shear transfer between the slab and the soil is assumed, increased vibration levels in the free-field are generally obtained, especially around the frequencies where the wavelength of the fundamental Rayleigh wave that dominates the response, is similar to the slab width. For the thick slab, both the shell model (Model c) and the beam model with constant cross-direction displacement (Model b), yield response levels that are within only a few percents of that obtained with the solid model (Model d). In the cases studied here, the rail point receptances and the wheel–rail interaction forces, as obtained with the different models are very similar, and are only marginally influenced by the in-plane slab–soil interaction.

Hence it can be concluded that for a thick slab, a beam model enforcing constant displacements under the slab width, is sufficient both with regards to the accuracy of the predicted rail receptance and the wheel–rail interaction forces, as well as the free-field vibrations, when compared to a solid continuum approach. However, for a thin slab, the cross-direction flexibility of the slab has a significant impact on the free-field vibrations, which may be accounted for by using a shell model. In any case, the in-plane shear forces in the slab–soil interface need to be regarded since they significantly affect the predicted free-field vibration levels.

7. Acknowledgments

The authors gratefully acknowledge financial support from the Swedish Innovation Agency (Vinnova) under grant no 2018-04159.

References

[1] Y. Yang, H. Hung, A 2.5D finite-infinite element approach for modelling visco-elastic bodies subjected to moving loads. *International Journal for Numerical Methods in Engineering*, **51**. 1317–1336, 2008.

[2] X. Sheng, C.J.C. Jones, D.J. Thompson, Prediction of ground vibration from trains using the wavenumber finite and boundary element methods. *Journal of Sound and Vibration*, **293**. 575–586, 2006.

[3] G. Lombaert, G. Degrande, J. Kogut, S. François, The experimental validation of a numerical model for the prediction of railway induced vibrations. *Journal of Sound and Vibration*, **297**. 512–535, 2006.

[4] P. Galvín, S. François, M. Schevenels, E. Bongini, G. Degrande, G. Lombaert, A 2.5D coupled FE-BE model for the prediction of railway induced vibrations. *Soil Dynamics and Earthquake Engineering*, **30**. 1500–1512, 2010.

[5] S. François, M. Schevenels, P. Galvín, G. Lombaert, G. Degrande, A 2.5D coupled FE-BE methodology for the dynamic interaction between longitudinally invariant structures and a layered halfspace. *Computer Methods in Applied Mechanics and Engineering*, **199(23-24)**. 1536–1548, 2010.

[6] P. Alves Costa, R. Calçada, A. Silva Cardoso, Track-ground vibrations induced by railway traffic: In-situ measurements and validation of a 2.5D FEM-BEM model. *Soil Dynamics and Earthquake Engineering*, **32(1)**. 111–128, 2012.

[7] X. Sheng, C.J.C. Jones, M. Petyt, Ground vibration generated by a harmonic load acting on a railway track. *Journal of Sound and Vibration* **225(1)**. 3–28, 1999.

[8] X. Sheng, C.J.C. Jones, M. Petyt, Ground vibration generated by a load moving along a railway track. *Journal of Sound and Vibration*, **228(1)**. 129–156, 1999.

[9] A.M. Kaynia, C. Madshus, P. Zackrisson, Ground vibration from high-speed trains: prediction and countermeasure. *Journal of Geotechnical and Geoenvironmental Engineering*, **126(6)**. 531–537, 2000.

[10] N. Triepaischajonsak, D.J. Thompson, A hybrid modelling approach for predicting ground vibration from trains. *Journal of Sound and Vibration*, **335**. 147–173, 2015.

[11] S.G. Koroma, D.J. Thompson, M.F.M. Hussein, E. Ntotsios, A mixed space-time and wavenumber-frequency domain procedure for modelling ground vibration from surface railway tracks. *Journal of Sound and Vibration*, **400**. 508–532, 2017.

[12] M.J.M.M. Steenbergen, A.V. Metrikine, The effect of the interface conditions on the dynamic response of a beam on a half-space to a moving load. *European Journal of Mechanics A/Solids*, **26**. 33–54, 2007.

[13] J. Malmborg, K. Persson, P. Persson, Modeling train-induced ground-borne vibrations using FEM in a moving frame of reference. In *Proceedings of Compdyn 2019: 7th International Conference on Computational Methods in Structural Dynamics and Earthquake Engineering, Crete, Greece.* 2019.

[14] L.V. Andersen, *Linear Elastodynamic Analysis*, Department of Civil Engineering, Aalborg University. DCE Lecture Notes, No. 3, 2006.

[15] W. Thomson, Transmission of elastic waves through a stratified solid medium. *Journal of Applied Physics*, **21**. 89–93, 1950.

[16] N. Haskell, The dispersion of surface waves on multilayered medium. *Bulletin of the Seismological Society of America*, **73**. 17–43, 1953.

[17] R. Wang, A simple orthonormalization method for stable and efficient computation of Green's functions. *Bulletin of the Seismological Society of America*, **89(3)**. 733–741, 1999.

[18] N. Ottosen, H. Petersson, *Introduction to the finite element method*, Pearson Education Ltd., Harlow, United Kingdom, 1992.

[19] E. Ntotsios, D. Thompson, M. Hussein, The effect of track load correlation on ground-borne vibration from railways. *Journal of Sound and Vibration*, **402**. 142–163, 2017.

[20] X. Sheng, C.J.C. Jones, D.J. Thompson, A theoretical model for ground vibration from trains generated by vertical track irregularities. *Journal of Sound and Vibration*, **272**. 937–965, 2004.